Time-resolved photoelectron spectroscopy of DNA molecules in solution

im Fachbereich Physik
der Freien Universität Berlin
eingereichte

Dissertation

von

Franziska Buchner

Berlin 2015

Erstgutachter: Prof. Dr. Marc Vrakking

Zweitgutachter: Priv.-Doz. Dr. Philippe Wernet

Tag der Disputation: 13.05.2015

The work presented here has been carried out at the *Max Born Institute* for Nonlinear Optics and Short Pulse Spectroscopy in Berlin-Adlershof.

Financial support by DFG project LU 1638/1-1 *Electronic structure and dynamics in a liquid waterjet* is acknowledged.

Abstract

In this thesis, I have advanced the recently-developed method of time-resolved liquid jet photoelectron spectroscopy to study the excited-state dynamics of solvated molecules applying femtosecond pulses in the ultraviolet range. The focus of this work was on the molecules that probably are the most relevant for life on earth: the DNA bases. Despite extensive studies with other ultrafast techniques, there are still important open questions. Time-resolved photoelectron spectroscopy provides a complementary and important view on the excited-state relaxation of these molecules and therefore helps to answer these questions.

When photoreactions in water are triggered (in particular by ultrashort pulses), the hydrated electron is an omnipresent intermediate. In order to disentangle signal of the hydrated electron from that of the molecule under investigation, I have first investigated the appearance of this species from photoexcitation to formation of free hydrated electrons in time-resolved photoelectron spectroscopy . As precursor iodide is used which is known to efficiently generate hydrated electrons after excitation in the deep ultraviolet range. The hydrated electron is bound by 3.4 eV. Surprisingly and due to an enhanced surface sensitivity of photoelectron spectroscopy, I have found a new decay channel, in which the hydrated electrons that are generated in the vicinity of the surface recombine with the geminate iodine radical on a sub-ps timescale, while in bulk this recombination takes 22 ps.

In this work, time-resolved photoelectron spectroscopy was for the first time applied to study the excited-state dynamics of DNA bases and nucleosides in diluted solution. For adenine, my results reproduce results from the literature: The excited state decays with two different lifetimes: 90 fs and 8 ps, and the two different decays are assigned to the two tautomers of adenine present in aqueous solution. For guanosine, I observe two spectral components that are associated with two different decay times: ∼250 fs and ∼2 ps. The faster decay is assigned to propagation of the excited-state wave packet out of the steep Franck-Condon region, while the slower decay corresponds to the internal conversion at the conical intersection between the excited state and the ground state. Previous studies were contradictory. The new results from photoelectron spectroscopy support the interpretation from fluorescence up-conversion experiments and therefore contribute with important new information that will guide to a more complete understanding of the photodynamics of guanine. For the pyrimidine bases (thymine and cytosine) and their nucleosides, photoelectron spectroscopy shows spectral contributions from two channels associated with two different decay times in the range of ∼100 fs and ∼400 fs for thymine, and ∼170 fs and ∼1.4 ps for cytosine. As suggested by molecular dynamics simulations, I have interpreted the data by two different relaxation paths on a single excited-state potential energy surface. The involvement of the nπ* state, which was widely accepted so far, is questioned by the present work.

Kurzfassung

In dieser Dissertation wurde die kürzlich entwickelte Methode der zeitaufgelösten Photoelektronenspektroskopie am Flüssigkeitsstrahl zur Untersuchung von angeregten Zuständen in gelösten Molekülen weiterentwickelt, wobei ultraviolette Femtosekunden-Impulse angewendet wurden. Der Fokus dieser Arbeit liegt auf den Molekülen mit der wahrscheinlich größten Relevanz für das Leben auf der Erde: den DNA-Basen. Trotz umfangreicher Untersuchungen mit anderen ultraschnellen Methoden gibt es hierbei immernoch wichtige offene Fragen. Zeitaufgelöste Photoelektronenspektroskopie liefert eine komplementäre und wichtige Sicht auf die Relaxation angeregter Zustände und hilft daher, diese offenen Fragen zu beantworten.

Werden Photoreaktionen in Wasser initiiert (insbesondere durch ultrakurze Impulse), so entstehen sehr häufig auch hydratisierte Elektronen. Um deren Signal von dem Signal der zu untersuchenden Moleküle zu unterscheiden, habe ich zunächst seine Bildung und Entwicklung mit Hilfe der zeitaufgelösten Photoelektronenspektroskopie untersucht. Als Precursor wurde Iodid genutzt, das unter Anregung mit ultraviolettem Licht sehr effizient hydratisierte Elektronen bildet. Diese sind mit 3,4 eV gebunden. Überraschend war die Beobachtung eines neuen Zerfallskanals für hydratisierte Elektronen in der Nähe der Wasseroberfläche, der nur durch die erhöhte Oberflächenempfindlichkeit dieser Methode gefunden wurde. Hier rekombinieren die Elektronen in weniger als einer Pikosekunde, während diese Rekombination im Bulk etwa 22 ps dauert.

In dieser Arbeit wurde zeitaufgelöste Photoelektronenspektroskopie zum ersten Mal auf verdünnte, wässrige Lösungen von DNA-Basen angewendet. Für Adenin wurden frühere Ergebnisse aus der Literatur reproduziert und zwei verschiedene Zerfallszeiten (90 fs und 8 ps) beobachtet, die den beiden in wässriger Lösung von Adenin vorliegenden Tautomeren zugeordnet wurden. Für Guanosin habe ich zwei spektrale Komponenten beobachtet, die zwei verschiedenen Zerfallszeiten zugeordnet sind: ∼250 fs und ∼2 ps. Die kürzere Zeit wurde dem Herauslaufen des Wellenpakets aus dem steilen Franck-Condon-Bereich zugeordnet, während die langsamere Zeit die interne Konversion vom angeregten in den Grundzustand durch die konische Durchdringung beschreibt. Hier waren frühere Untersuchungen widersprüchlich, aber die neuen Ergebnisse aus der zeitaufgelösten Photoelektronenspektroskopie stützen die Resultate der Fluoreszenz-Messungen und tragen daher zu einem besseren Verständnis der Photodynamik von Guanin bei. Für die Pyrimidin-Basen (Thymin und Cytosin) und ihre Nukleoside zeigt die zeitaufgelöste Photoelektronenspektroskopie spektrale Beiträge von zwei Relaxationskanälen, denen zwei verschiedene Zeiten zugeordnet werden: ∼100 fs und ∼400 fs für Thymin und ∼170 fs und ∼1,4 ps für Cytosin. Motiviert durch Moleküldynamik-Simulationen habe ich diese Daten als Relaxation entlang zweier verschiedener Pfade auf derselben Potentialfläche des angeregten Zustands interpretiert. Die Beteiligung eines nπ*-Zustandes, die bislang weit akzeptiert war, wird in dieser Arbeit infrage gestellt.

Contents

1. Introduction

It is well-known that frequent sun-burns hold the risk of skin cancer being the long-term effect of changes in the genetic information that each cell carries. The molecule, that stores the genetic information of living species on earth, is the well known deoxyribonucleic acid (DNA). DNA is a polynucleotide, composed of smaller units, the nucleotides. Every nucleotide contains one out of the four DNA bases (adenine, guanine, cytosine, and thymine), a sugar moiety (deoxyribose) and a phosphate group. The nucleotides are attached to each other like a chain of pearls – covalently linked *via* the phosphate groups (phosphodiester bonds). The sequence of DNA bases along the chain encodes the genetic instructions for synthesis of proteins which actually catalyse most of the biochemical reactions within a cell. Changes in the DNA sequence – the so-called mutations – are the motor for evolution but can also lead to development of malfunctioning cells and consequently lead to cancer.

Besides genotoxic chemicals and ionising radiation, also ultraviolet (UV) light can induce a damage of the DNA – the so-called photodamage. DNA bases absorb light in the UV range (about 200–380 nm) which has sufficiently high energy to break chemical bonds. However, the DNA molecule is astonishingly resistant versus light induced changes. There have been a number of experimental and theoretical studies on the DNA itself and the DNA bases in order to understand and explain this photostability. Besides the fact that in living cells a number of repair mechanisms exist in order to prevent consequences for the cell, it seems to be an inherent property of the DNA bases themselves to dissipate the energy so quickly that chemical bonds are protected.

The development of ultrashort laser pulses (with femtosecond duration) enabled the extension of time-resolved spectroscopic methods to the time-scale of nuclear motion [1]. Transient absorption (TA), fluorescence up-conversion (FU) and time-resolved photoelectron spectroscopy (TRPES) are different techniques to study ultrafast phenomena and differ in the kind of probing process. In TA, the excited state is probed by a transition into a higher excited state but competing processes like ground state bleach and/or ground state absorption complicate the analysis. In FU, the spontaneous transition into the ground state upon emission of light is measured. These two methods are most common for solvated samples, and solvated DNA bases were extensively studied exploiting these two methods [2]. In TRPES, the excited molecule is photoionised and the kinetic

energy of the photoelectron is analysed. This method requires high vacuum conditions to ensure photoelectron detection without energy loss (due to scattering events). It is therefore commonly used to study excited-state dynamics of isolated molecules in the gas phase and in surface science.

In the last two decades, a liquid jet technique was developed which allows us to apply the TRPES also to liquid samples and molecules in solution. In this work, I will show that time-resolved photoelectron spectroscopy is a powerful tool to investigate the excited state dynamics and energetics of molecules in solution. I will present the first time-resolved photoelectron spectra of DNA bases and nucleosides in aqueous solution. The following issues will be addressed:

- To what extend does TRPES provide new, complementary information on the excited state dynamics of DNA bases in solution?
- For the excited state relaxation of the pyrimidine bases (cytosine and thymine), the involvement of an optically dark $n\pi^*$ state has been proposed but not directly observed. With TRPES, we can ionize all excited states and confirm or refute the involvement of this state in the relaxation process. If an $n\pi^*$ state is occupied during the relaxation, also its binding energy is accessible by TRPES.
- Theoretical simulations of molecules in solution are costly but the ionic state is in principle easily accessible. Therefore, this method can also be used to check the applicability of theoretical simulations – or even calibrate the calculations. Collaborations with theory groups have been established in order to compare the experimental results with sophisticated simulations of DNA bases in solution, i.e. in large water clusters.

In TA experiments on DNA bases, the signal from hydrated DNA bases was superimposed by the signal from solvated electrons. We expect to observe signal related to the hydrated electron in TRPES, too. To be able to distinguish between the two different signals, we have started our investigations by studies of the hydrated electron, only. We performed time-resolved photoelectron spectroscopy of a sodium iodide solution (easily generating the solvated electrons) and solutions of three DNA bases and four nucleosides. I will first give some general information on the method (Chapter 2) and then explain the setup in detail (Chapter 3). In Chapter 4, I will show the results obtained for sodium iodide solution and describe how a solvated electron is generated and evolves in time. Afterwards, I will discuss the experimental data on the different DNA bases and nucleosides in solution in Chapter 5. The whole work will be completed with Chapter 6 summarising the main findings and emphasising the impact of this work on the progress in the research field.

2. Photoelectron spectroscopy of liquids - problems and solutions

Photoelectron spectroscopy uses the principle of photoemission to evaluate the energy of occupied orbitals in atoms and molecules. Figure 2.1 illustrates this principle: an electron from a bound state is ejected upon absorption of one or more photon(s) with an energy of $\hbar\omega$. The kinetic energy of the photoelectron is then given by

$$E_{\text{kin}} = n \times \hbar\omega - E_b, \tag{2.1}$$

where n is the number of absorbed photons and E_b is the binding energy. The photoelectron spectrum shows the kinetic energy distribution of these photoelectrons measured by an appropriate spectrometer. From such a spectrum we can deduce the energy levels of an atom or a molecule relative to the absolute energy of the free electron in vacuum. For lower photon energies, only the weakly bound valence orbitals can be ionized, whereas for higher photon energies also the core levels are accessible (see Figure 2.1).

2.1. Time-resolved photoelectron spectroscopy

The development of the pump-probe method by A. Zewail in the 1980s enabled the investigation of excited states of molecules and was awarded with the Nobel prize in chemistry in 1999. Zewail aimed at observing the bond breaking and bond making in a photo-induced chemical reaction. The initial step of such a reaction occurs on a femtosecond to picosecond time-scale. Therefore, the previous development of ultrashort pulsed laser sources was essential for Zewail's scientific success.

In time-resolved spectroscopy, a molecule is excited by absorbing a photon of a first pulse, the pump pulse. The subsequent relaxation of the molecule or chemical reaction is observed by interaction with a second pulse, the probe pulse. The time-dependent evolution of the excited state is followed by scanning the pump-probe time delay. In the recent decades, a number of time-resolved methods have been developed exploiting different spectroscopic techniques.

In Figure 2.2, the pump-probe scheme is illustrated for photoelectron spectroscopy where the probe process is ionization. A molecule in the ground state (gs, black) with

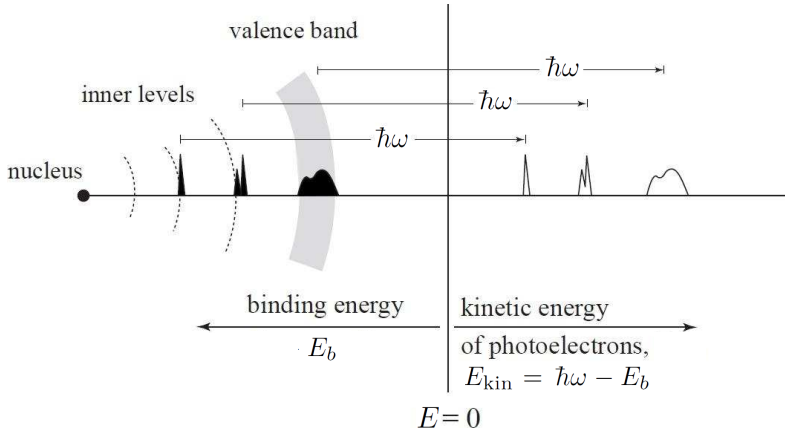

Figure 2.1. Principle of photoemission. The dashed lines and grey bar represent occupied core and valence levels of an atom. XUV-photons of energy $\hbar\omega$ ionize the different levels leading to a photoelectron spectrum with the corresponding peaks at $E_{\mathrm{kin}} = \hbar\omega - E_b$. Picture taken from Ref. [3].

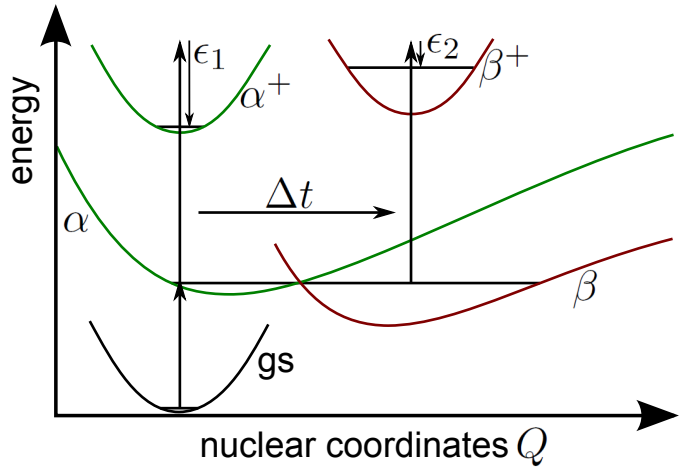

Figure 2.2. Principle of time-resolved photoelectron spectroscopy assuming a molecule with molecular coordinates Q. Initially, the ground state (gs) of the molecule is populated. Absorption of a pump photon leads to the excited state α. At zero delay, α is ionized by a probe photon leading to the formation of the ionic state α^+ and a photoelectron with a kinetic energy ϵ_1. At later delay times Δt, state α has evolved and non-adiabatically coupled to state β, where higher vibrational states are occupied. Ionization by a probe photon of the same energy now leads to the ionic state β^+ and a photoelectron with a kinetic energy ϵ_2. Picture adapted from [4].

nuclear coordinates Q absorbs a pump photon, and the initially excited state α is prepared. A delayed probe pulse ionizes the molecule and generates a photoelectron. At very short delay times, the probe pulse ionizes the α state leading to a photoelectron with a kinetic energy ϵ_1 and the ionic state α^+. In the example sketched in Figure 2.2, the state α can couple non-adiabatically to state β. Resulting from this coupling, higher vibrational states of β are populated. At longer delays Δt, ionization by the probe pulse

therefore leads to an ionic state β^+ and a photoelectron with a different kinetic energy ϵ_2.

In the work presented here, ultraviolet light is applied corresponding to photon energies in the range of about 4.5–6.2 eV. These low photon energies make this method almost background-free, because there are only very few molecules, that have ionization potentials as low as 6 eV. Therefore, photoionization of the ground state with only one pulse occurs in a multi-photon process. However, in a time-resolved process applying one photon of each pulse, the total photon energy will be about 10 eV – enough to ionize a lot of organic molecules. The choice of these low photon energies provides the large advantage that ionization with only one of the pulses is significantly less probable than (1+1)-photon processes occurring in the pump-probe scheme. Hence, we can study the excited state dynamics almost background-free in contrast to other groups who aim at using higher photon energies.

Time-resolved photoelectron spectroscopy is a well-established method for investigation of electron dynamics in isolated molecules [5, 6] and in surface science [7, 8]. This work is among the first ones, in which this technique is applied to liquid samples.

2.2. Liquids in vacuum

For an accurate measurement of the kinetic energy, the photoelectrons have to reach the detector without colliding with atoms or molecules in the meantime. Hence, high vacuum conditions are needed. Volatile liquids, however, have high vapour pressures (e.g. about 20 mbar for water at room temperature) counteracting an appropriate working pressure. With the exception of a few liquids with exceptionally low vapour pressures (e.g. formamide: 0.13 mbar at 30°C, see early experiments of Siegbahn [9]), photoelectron studies were only possible for gases and solids until the late 20th century. This problem was solved by Faubel *et al.*, who invented the liquid microjet technique [10, 11]. The liquid is pushed through a nozzle with inner diameter of 5–50 µm into vacuum and forms a jet. Such a liquid jet is shown in Figure 2.3. The jet flows laminarly for some distance which depends on the liquid, the flow rate, and the nozzle diameter. Afterwards, the jet becomes unstable and finally breaks apart into droplets. From the jet surface, molecules evaporate into the vacuum leading to a cylindrical pressure gradient.

The distance an electron can travel before colliding with surrounding molecules is the electron mean free path l. At thermal equilibrium, it is given by [12]:

$$l = (n_{\mathrm{vap}}\,\sigma_{\mathrm{el}})^{-1}, \tag{2.2}$$

where n_{vap} is the density of the vapour molecules and σ_{el} is the cross-section for an

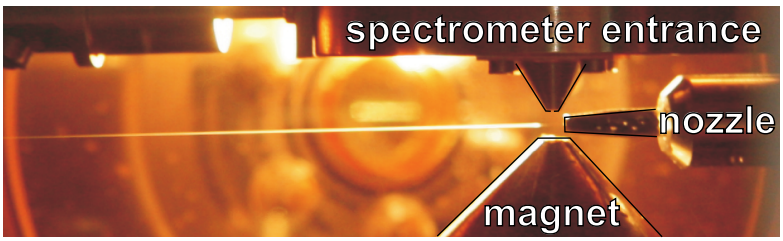

Figure 2.3. Photograph of the liquid jet in the interaction chamber. After entering into the vacuum, the jet flows laminarly for a few millimetres. Afterwards it breaks apart into droplets giving rise to enhanced light scattering (white horizontal line).

Table 2.1. Mean free path of a low kinetic energy electron (about 5 eV) in water vapour at thermal equilibrium.

pressure / mbar	mean free path
1013	53 nm
20	2.7 µm
3.6	15 µm
1	54 µm
$5.4 \cdot 10^{-2}$	1 mm
10^{-3}	54 mm
$2 \cdot 10^{-4}$	27 cm
$5.4 \cdot 10^{-5}$	1 m
10^{-6}	54 m

electron colliding with a vapour molecule. As a first approximation, the ideal gas concept is used to derive the density of the vapour molecules n_{vap} from the pressure p.

$$n_{\text{vap}} = \frac{p}{k_B T}. \tag{2.3}$$

For photoelectrons with kinetic energy between 1 and 10 eV, the scattering cross-section is about $20\text{–}120 \cdot 10^{-16}\,\text{cm}^2$ [13]. In Table 2.1, the mean free path of an electron of about 5 eV kinetic energy (corresponding $\sigma_{el} \sim 70 \cdot 10^{-16}\,\text{cm}^2$) at different densities of water vapour is listed. The table shows that for an 1 m long flight tube, a pressure of $5 \cdot 10^{-5}$ mbar has to be reached to ensure collision-free conditions. During operation (while the liquid jet is running), we measure a pressure $1 \cdot 10^{-6}$ mbar in the spectrometer achieving this condition. For the distance between the jet surface and the entrance into the spectrometer, Faubel *et al.* have shown that for a sufficiently small jet radius, the electrons travel collision-free [14].

This technique finally enables scientists to perform photoelectron studies on free flowing liquids in vacuum which is successfully used by several groups around the world [15–17].

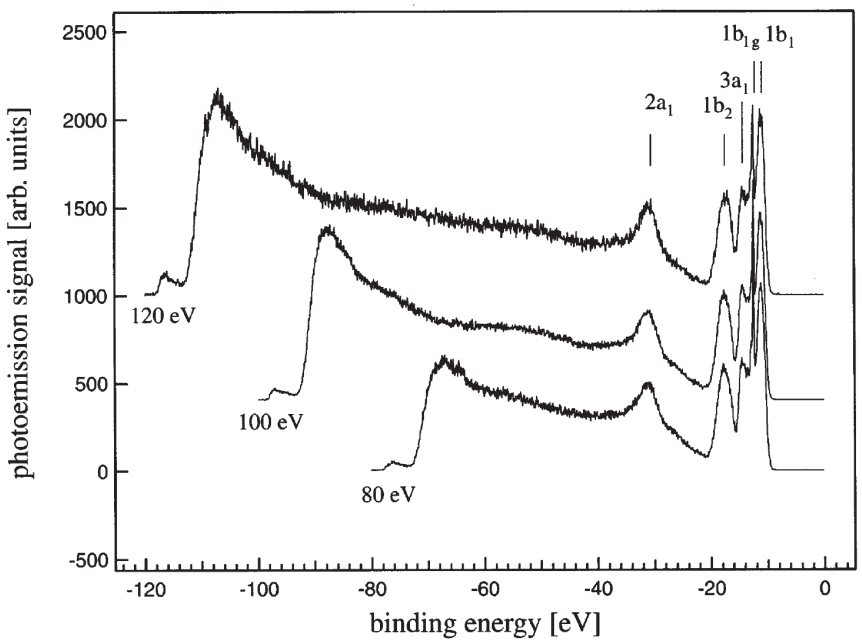

Figure 2.4. Photoelectron spectrum of liquid water obtained for different photon energies (80, 100, 120 eV). The peaks at small binding energies correspond to ionization of the four valence orbitals of the water molecule ($1b_1$, $3a_1$, $1b_2$, and $2a_1$). The strong background signal is assigned to secondary electrons due to inelastic scattering. The picture is taken from Ref. [16].

2.3. Electron scattering and electron range in the liquid

Static photoelectron spectroscopy of pure water and different salt solutions was intensively studied by Bernd Winter *et al.* (e.g. [12, 16, 18]). Photoelectron spectra of liquid water measured with different photon energies are shown in Figure 2.4 [16]. The peaks at low binding energies correspond to ionization of the occupied molecular orbitals of the water molecule ($1b_1$, $3a_1$, $1b_2$, and $2a_1$). The strong background which seems to grow with increasing binding energy is referred to as secondary electrons. These are electrons that have lost kinetic energy due to multiple inelastic scattering events on their path through the liquid and therefore give rise to the continuous background in the spectrum.

In the work presented here, photoelectrons with low kinetic energies are emitted where this effect of multiple inelastic collisions does not play a significant role. The inelastic scattering cross-sections depend on the kinetic energy of the photoelectrons. Plante et al. have calculated the cross-sections for different processes in liquid water for electron kinetic energies in the range between 1 eV and 100 MeV [19]. Their results are shown in Figure 2.5. They found ionization and electronic excitation to be important only for electron kinetic energies above 10 eV. Below 10 eV, the cross-sections for these two processes decrease by at least five orders of magnitude. In the present work, UV pulses

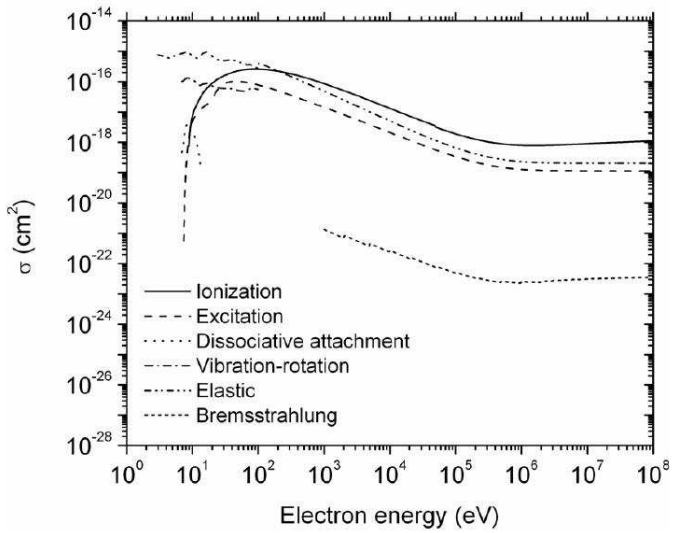

Figure 2.5. Calculated cross-sections for different scattering processes as a function of electron energy [19].

are used and photoelectrons with kinetic energies below 10 eV are generated. Thus, ionization and electronic excitation are much less important than in the aforementioned EUV studies with photon energies of about 100 eV. Dissociative electron attachment is important for electron kinetic energies around 6–10 eV. This process decreases the total signal but will not contribute to the spectrum. The remaining processes are excitation of vibrational and rotational states and elastic scattering. The latter does not change the electron kinetic energy and can thus be neglected for this discussion. Rotational excitation would only change the kinetic energy of the photoelectrons by tiny amounts compared to the broad photoelectron distributions expected due to the large variation in geometries. Cross-sections of vibrational excitation in amorphous ice were studied by Michaud et al. [20]. They found that energy-loss due to vibrational excitation would reduce the kinetic energy of the electrons by up to 0.4 eV (stretching mode excitation) with relatively low cross-sections. Regarding Figure 2.5, inelastic scattering cross-sections decrease drastically when moving from kinetic energies of about 200 eV to below 10 eV. Hence, in the experiments presented here, where the photoelectron kinetic energies are below 10 eV, inelastic scattering does not play a significant role.

Another relevant issue is the electron range in water and to what extent this method is surface or bulk sensitive. The electron range in water depends on the electron kinetic energy. We have shown that with our set-up and UV photons, photoelectrons from a depth of up to 5 nm are detected [21]. In order to distinguish between contributions from the surface and from the bulk, we used the surface-active salt tetrabutyl ammonium iodide (TBAI) and added bulk contribution by addition of sodium iodide (NaI).

Experimentally observed changes in the iodide signal can be related to the surface versus bulk contribution of iodide. In a first experiment, we used a solution of 0.2 mM TBAI which has a strong propensity to be at the surface, but at this concentration the surface is not yet saturated [22]. Therefore, the iodide signal of this TBAI-only solution is dominated by surface contributions. In a second experiment, we added bulk contribution by addition of 1.8 mM NaI to the 0.2 mM TBAI solution. For a totally bulk-sensitive measurement, we would expect the intensity of the iodide photoelectron signal to increase with the total iodide concentration, i.e. by a factor of 10. Whereas for a surface-sensitive measurement, the iodide photoelectron signal would increase less strongly than the bulk iodide concentration. In order to extract a value for the electron range, the radial distribution of iodide is needed. We assumed a simplified distribution based on the molecular dynamics simulations performed by Jungwirth and Tobias [23]. This simplified radial distribution underestimates the electron range and the obtained value therefore may be treated as the lower limit. Additionally an exponential escape probability is assumed. The difference in the iodide signal intensity supports an electron range of about 5 nm. Hence, photoelectrons do not escape the center of the jet but still the electron range is about 17 times larger than a single water molecule ($\sim$3Å). Therefore, we observe dynamics occurring at the surface but also in the region beyond.

Hence, applying photoelectron spectroscopy with UV light, we observe contributions from the surface layer and from the bulk. Further theoretical and experimental works have confirmed this finding [19, 24–26].

2.4. Electrokinetic charging

Elektrokinetic charging creates a potential difference between the liquid jet and the electron spectrometer and therefore electrostatically accelerates or retards emitted photoelectrons. Electrokinetic charging can lead to significant potentials on the order of tens of volts as derived for pure water [10] and alcohols [27]. For liquid jet photoelectron spectroscopy, this charging is a serious problem, especially when applying low photon energies in the UV range. With such low photon energies, no reference molecule inside the liquid jet can be ionized to monitor the actual potential during the experiment. Therefore, the electrokinetic charging itself has to be suppressed efficiently.

Electrokinetic charging occurs when a solution containing ions flows over a surface and carries one type of ions away while the counterions remain at the static interface. In the experimental set-up considered here, water flows through a stainless steel tubing and a fused-silica nozzle into a vacuum chamber. The first approach to overcome the problem of charging would be to eliminate the ions from the solution. For water, however, this

is not possible due to its autoprotolysis.

$$H_2O + H_2O \rightleftharpoons H_3O^+ + OH^- \tag{2.4}$$

Hence, in water a minimal amount of ions will always be present.

Being in contact with water, the silica surface becomes hydrated as shown in Figure 2.6. The so-called Haber-Haugaard layer of a hydrated silica surface contains acidic

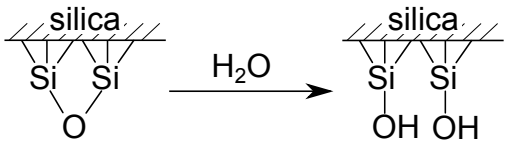

Figure 2.6. A silica surface is hydrated.

hydroxyl groups (-OH) [28, 29]. In general, these hydroxyl groups can act as proton acceptors or proton donors as shown in equations (2.5). An equilibrium will be established.

$$\begin{aligned} \text{Si-OH} + H^+ &\rightleftharpoons \text{Si-OH}_2^+ \\ \text{Si-OH} &\rightleftharpoons \text{Si-O}^- + H^+ \end{aligned} \tag{2.5}$$

In neutral water, the equilibrium is balanced such that the hydroxyl groups are deprotonated leading to a negatively charged surface (Si-O$^-$)[30]. Charging of the glass surface creates an electrostatic potential which causes the formation of a diffusely bound Gouy-Chapman layer of counterions (in this case cations). Figure 2.7 illustrates the electrokinetic charging mechanism at the exit of a fused-silica nozzle. The ion concentration in the diffuse Gouy-Chapman layer decreases exponentially with increasing distance from the surface. The characteristic length over which the potential decreases to e^{-1} relative to the surface potential is the so-called Debye length r_D [31],

$$r_\mathrm{D} = \sqrt{\frac{\varepsilon_0 \varepsilon_r^j k T}{2 e^2 N_A S}}, \tag{2.6}$$

where ε_0 is the vacuum permittivity , ε_r^j is the relative permittivity of the jet, k is Boltzmann's constant, T is the jet temperature, e is the elementary charge, N_A is Avogadro's constant and S is the ionic strength. The latter depends on the concentrations c_i of all ions in the solution and their ionic charge z:

$$S = \frac{1}{n} \sum_{i=0}^{n} c_i z_i^2. \tag{2.7}$$

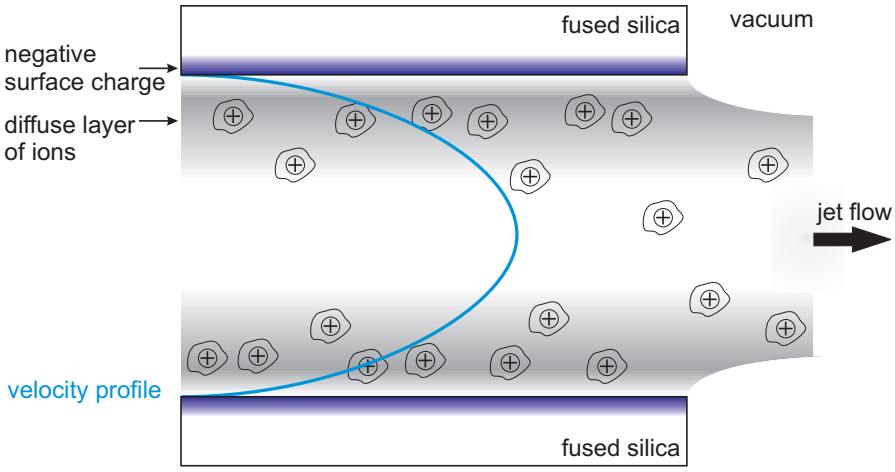

Figure 2.7. Schematic illustration of the longitudinal section of a liquid jet flowing through a fused silica nozzle into vacuum. At the silica surface, the "Haber-Haugaard layer" is negatively charged (violet). A diffuse layer of counterions (cations) called "Gouy-Chapman layer" (grey) builds up and partly sticks to the surface. Due to the laminar flow with a parabolic velocity profile (blue line), ions in the diffuse layer are sheared off. Net-charge separation results and leads to a surface potential at the water/vacuum interface.

For laminar flow, the velocity profile inside the nozzle is parabolic as indicated in Figure 2.7. The velocity is highest in the center of the jet and vanishes at the liquid/silica interface. Therefore, a part of the diffuse layer is sheared off leading to a net-charge separation. The resulting streaming current I depends on the net ion charge distribution $\rho(r)$ and the radial velocity profile $u(r)$ of the liquid jet [10, 27]:

$$I = \int_0^{r_\mathrm{N}} \rho(r) \cdot u(r)\, \mathrm{d}r, \tag{2.8}$$

where the integration runs from the center of the jet ($r = 0$) to the inner wall of the nozzle ($r = r_\mathrm{N}$).

Equation (2.8) implies that there are two conditions, where no (or least) electrokinetic charging occurs. Firstly, the Debye length could be larger than the nozzle radius. This corresponds to the case of a solution with practically no charges (which is not applicable for water due to the autoprotolysis). Secondly, in the presence of ions, the Debye length should be very small, i.e. for large ion concentrations and for high ionic charges (see equations (2.6) and (2.7)). Then the range over which the charges separate is small and only few charges are sheared off due to the velocity gradient close to the interface. This second condition has been applied for a number of recent photoelectron studies [15, 17, 21, 32–36], where addition of salt suppressed electrokinetic charging.

At MBI, we have studied the influence of salt concentration on the amount of excess charges in the jet [37] and found a concentration of 30 mM monovalent salt to sufficiently

suppress the charging of the liquid jet.

In addition to the aforementioned and discussed process, proton concentration changes can generate time-dependent charging of the liquid jet. Protons are able to diffuse quickly into or out of the silica glass surface leading to a positive or negative surface potential, respectively. Larger anions will then follow slowly and neutralize the potential time-delayed. Hence, a time-dependent surface potential will influence the photoelectrons generated from the liquid jet. Therefore, the buffer solution flows through the nozzle at least for 10 h to allow for adaption of the nozzle surface potential.

In neat water, dissolving small amounts of CO_2 can lead to quite substantial changes in the pH value. Therefore, our sample solution is always prepared freshly each day.

3. Experimental setup

In this experiment, time-resolved photoelectron spectroscopy is combined with the liquid jet technique. A schematic picture of the setup is shown in Figure 3.1. The liquid jet is pushed into the interaction chamber where the pump and probe pulses generate photoelectrons from sample molecules. The interaction chamber houses three cold traps to freeze out the liquid jet and water vapour. It is pumped by a 1500 l/s turbo molecular pump to keep the volume of about 0.05 m^3 at adequate working pressures below 10^{-3} mbar. The photoelectrons are guided by a magnetic bottle into the time-of-flight spectrometer and finally detected on a chevron-type multi-channel plate (MCP) detector with phosphor screen. The spectrometer is separated from the interaction chamber by a spherical valve and differentially pumped by two 500 l/s turbo molecular pumps.

The set-up used for the first experiments on the solvated electron has been described in detail in reference [15]. There have been several improvements. In the following, the actual set-up will be explained in detail.

3.1. The liquid jet

A high pressure liquid chromatography (HPLC) pump pushes the sample solution through a fused silica nozzle (inner diameter of 12–15 µm, 30 mm long) into vacuum. Figure 3.2 shows a photograph of the liquid jet in the interaction chamber. Directly after the nozzle, the jet flows laminarly. Evaporation of water molecules from the surface leads to slightly reduced jet diameters. From the diffraction pattern of a HeNe laser diffracted from the jet in vacuum, we deduced a jet diameter of about 8 µm generated from a nozzle with 13 µm inner diameter. The flow rate is typically about 0.5 ml/min resulting in a jet velocity of about 50 m/s. The pressure in the HPLC pump depends on the flow rate and the pore size of the microfilter in the tubing of the jet. This pressure is typically in the range of 10–50 bar with a maximum value of 100 bar.

Three cold traps are placed in the interaction chamber (see grey structures in Figure 3.1): one in direction of the liquid jet in order to freeze out the water jet and two additional cold traps to freeze out water vapour in the interaction chamber. If all cold traps are filled with liquid nitrogen, we can ensure an appropriate working pressure of about 5×10^{-4} mbar while the jet is running. The entrance to the differentially pumped

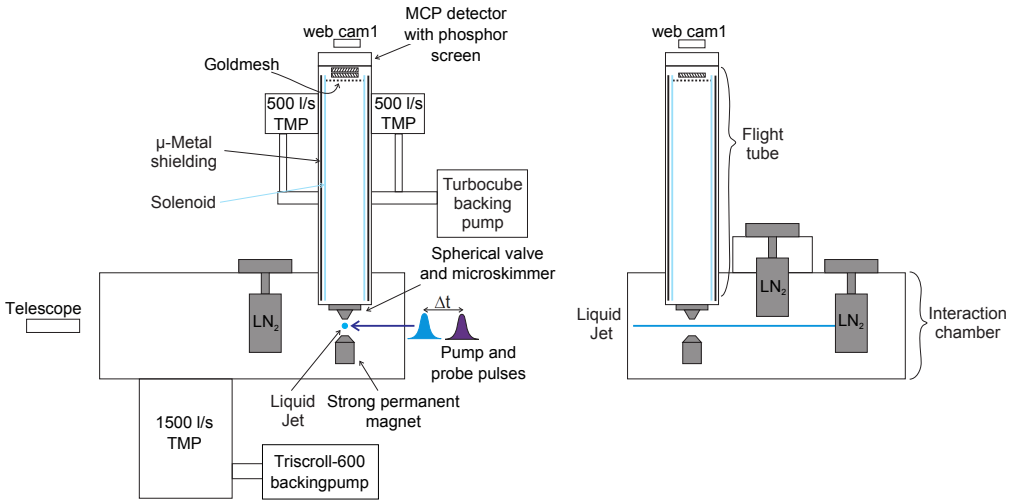

Figure 3.1. The experimental set-up from the front (left) and in side view (right). See details in the text.

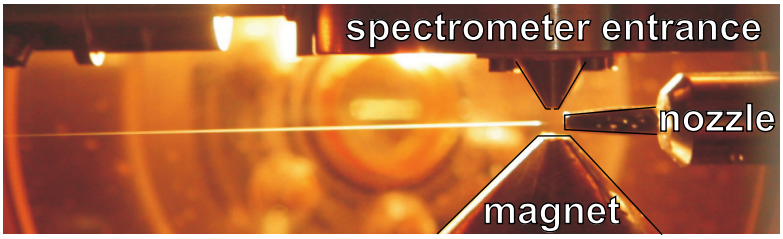

Figure 3.2. Photograph of the liquid jet in the interaction chamber. Just after entering into the vacuum, the jet flows laminarly for a few millimeters. Afterwards it breaks apart into droplets giving rise to enhanced light scattering (white horizontal line). Experiments are performed in the region of laminar flow, i.e. the invisible part of the jet in between the soft iron tip of the magnet and spectrometer entrance.

spectrometer is only about 1 mm away from the interaction region where the photoelectrons are generated. Faubel and co-workers have proven collision-free emission of photoelectrons for sufficiently small jet diameters [11]. Hence, we can be sure, that the photoelectrons enter the spectrometer without colliding with water molecules around.

In order to quickly diagnose liquid beam instabilities during experiments, we continuously monitor the jet through the telescope (see Figure 3.1) which is mounted under an angle with respect to the laser propagation axis – otherwise would be blocked by the cold trap. For a usual experiment with a 10–14 hours per day continuously running jet, about 300–400 ml of sample solution is pushed into the interaction chamber and frozen out on the cold traps. Therefore, daily venting and cleaning of the interaction chamber is necessary. A spherical valve can isolate the spectrometer from the interaction chamber and therefore minimizes the maintenance time.

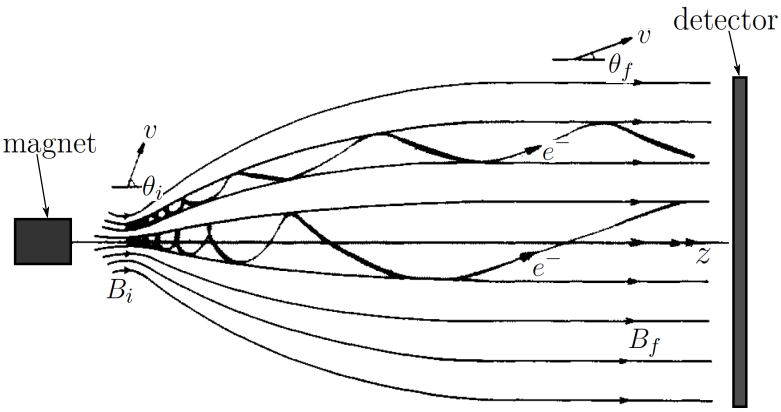

Figure 3.3. Principle of a magnetic bottle invented by Kruit and Read [38] and adapted to the present setup.

3.2. The spectrometer

The spectrometer is a time of flight spectrometer using a magnetic bottle to maximize the collection efficiency [38].

The magnetic bottle principle. A magnetic bottle collects electrons from a dihedral angle of 2π and guides them towards a detector. The magnetic bottle is formed by a strong inhomogeneous (B_i) and a weak homogeneous magnetic field (B_f) which is shielded against external fields. Figure 3.3 shows the principle. Photoelectrons that are generated in the strongly divergent field of the magnet, spiral along the magnetic field lines due to Lorentz' force. The angular momentum l of the circular motion is given by [38]

$$l = \frac{m_e^2 v^2 \cdot \sin^2\theta}{eB}, \tag{3.1}$$

where m_e is the mass of the electron, v is its velocity, θ the angle of the velocity vector with respect to the spectrometer axis z and B is the magnetic field. The angular momentum and the kinetic energy are conserved. Therefore, reduction of the B-field requires a decrease of the angle θ. Consequently, velocity components perpendicular to the spectrometer axis are transformed into parallel components. Therefore, magnetic bottle spectrometers in general have a high collection efficiency. The energy resolution of the spectrometer is limited by electron motion perpendicular to the magnetic field lines leading to longer trajectories. This perpendicular motion is determined by the gradient of the magnetic field. In the drift tube, the maximum angle $\theta_{f,\max}$ of the electrons with respect to the spectrometer axis is given by

$$\sin\theta_{f,\max} = \sqrt{B_f/B_i}\,. \tag{3.2}$$

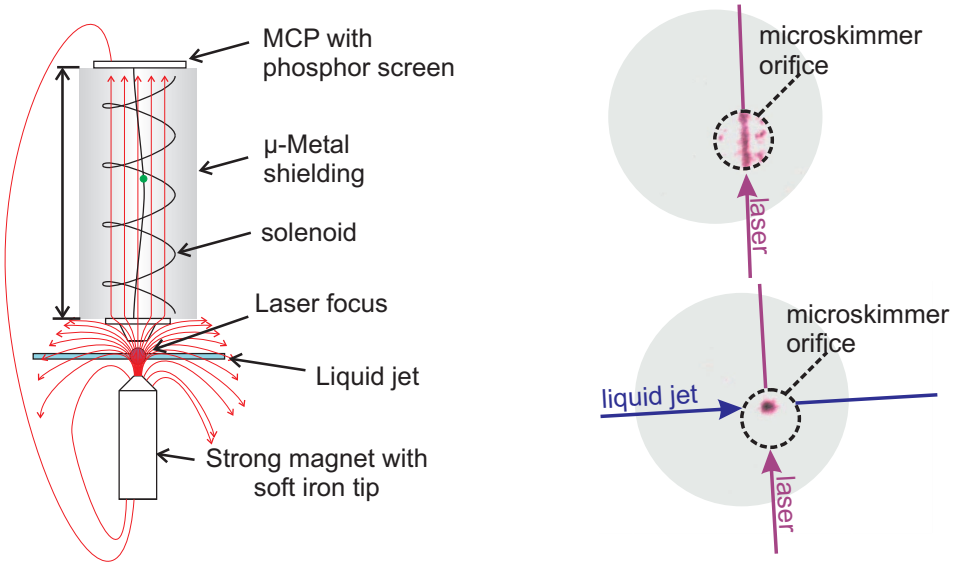

Figure 3.4. Left: Magnetic bottle time-of-flight spectrometer: Red arrows indicate magnetic field lines. **Right:** Photoelectron source images at the phosphor screen for gas phase experiments (top) and liquid jet experiments (bottom). The grey area is the active area of the phosphor screen behind the MCPs. The dashed circle around the signal indicates the image of the microskimmer orifice (in this case about 500 μm diameter).
For details see text.

And the maximum diameter of the cyclotron motion in the drift tube is then [38]:

$$d_{\mathrm{cyc}} = \frac{\sqrt{2m_e E_{\mathrm{kin}}}}{eB_i}. \tag{3.3}$$

The electrons spiral around "their" field lines and therefore, every cross-section through the spectrometer is an image of the starting position of the electrons, magnified by the factor $M = (B_i/B(z))^{1/2}$.

A schematic picture of the actual spectrometer is shown in Figure 3.4. Laser focus and liquid jet are overlapped in the divergent field of a strong permanent magnet (about 1 T). The soft iron tip increases the gradient of the magnetic field in the interaction region. Inside the flight tube, a weak magnetic field (about 1 mT) is generated by a current (about 0.6 A) flowing through a solenoid around the tube. According to equation 3.3, the maximum diameter of the cyclotron motion of about 5 eV photoelectrons is then $d_{\mathrm{cyc}} = 15\,\mu\mathrm{m}$.

Before entering the flight tube, the photoelectrons pass a small orifice of 500 μm. This orifice ensures pressures below 10^{-6} mbar in the flight tube while the jet is operating. Only at these low pressures, the MCP detector can be operated safely.

The permanent magnet is mounted on three stepping motors to adjust the magnetic bottle such that the photoelectrons are not clipped at the orifice and the entire spatial

distribution of the photoelectron signal is observed on the MCP-detector containing a phosphor screen. The magnetic bottle is capable of collecting nearly all photoelectrons ejected from the liquid jet. However, photoelectrons emitted into the lower half sphere are first reflected in the strong and inhomogeneous magnetic field and only at later times of flight detected by the MCPs. These electrons are not used for analysis and are referred to as arising from *reflected trajectories*. For analysis, we only use the photoelectrons that follow *direct trajectories*, i.e. those that are emitted into the upper half sphere (towards the flight tube). These are about 50% of the entire photoelectrons.

A grounded gold mesh terminates the electrical field-free flight tube. Behind the mesh the electrons are pre-accelerated by a potential difference of 300 V between the gold mesh and the front side of the first MCP of a chevron-type MCP detector (Photonis, Model 3040 FM). The distance between gold mesh and first MCP is about 1 cm. This pre-acceleration enhances the MCP's detection efficiency for the very low kinetic energy electrons studied here [39]. The MCPs multiply and accelerate the electrons which finally illuminate the phosphor screen and thereby make the electron source visible. The phosphor screen helps enormously to align/adjust the spectrometer, to overlap pump and probe pulses, and to differentiate gas phase from liquid jet signal. In Figure 3.4, the right panel shows images of the phosphor screen when ionizing either the gas (top) or the liquid jet (bottom). Of course, the intensity of the laser pulses was attenuated strongly in the latter case. Pulse energies were always chosen such that electron count rates were on the order of 10 per shot or less.

The signal is capacitively coupled out at the second MCP, then processed by a NOVELEC amplifier and read by an Acqiris card (AP240) which is plugged into a personal computer (see Figure 3.5). A system of two chopper wheels selects/excludes two subsequent pulses in each laser beam (see also optical setup in section 3.3). The second chopper runs with a phase offset of $\pi/2$ with respect to the first chopper. A linear combination of the two chopper output signals is generated electronically and also read out by the Acqiris card. A C++ routine then assigns counted electron signal to chopper positions and integrates histograms for the two-colour signal (pump + probe), the one-colour signals (pump-only and probe-only) and additionally computes the difference signal (pump – probe).

3.3. The light sources

In all experiments discussed here, the same regeneratively amplified Titanium:Sapphire laser system is used. At 800 nm central wavelength it delivers 3 mJ pulses of sub-40 fs duration at a repetition rate of 1 kHz. Figure 3.6 shows the optical setup. The beam is split into two parts. The first part (1) is used to generate the third harmonic by second

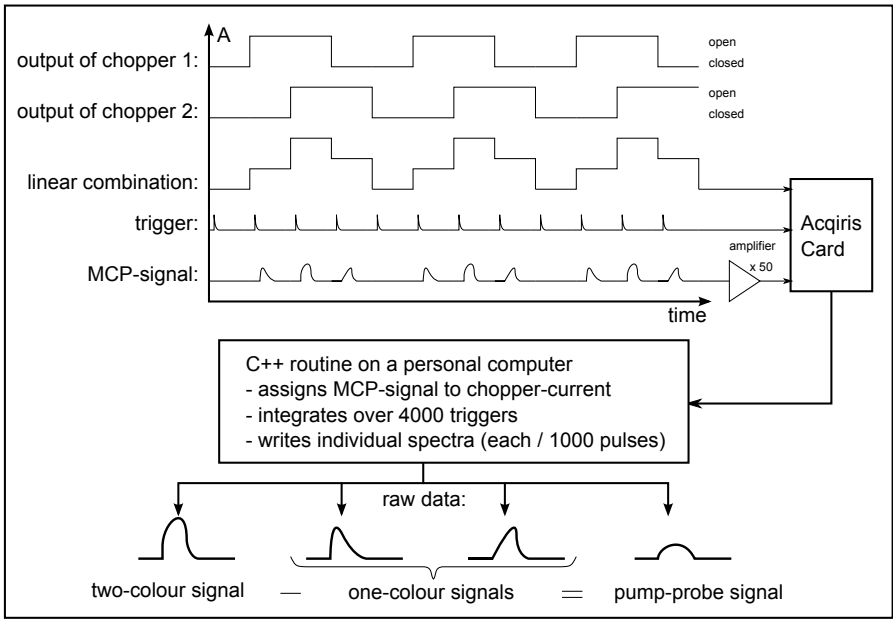

Figure 3.5. Description of the signal processing. The Acqiris Card reads out a linear combination of the two individual chopper outputs (generated electronically), the amplified MCP-signal, and the trigger from an external photodiode. At each trigger, the MCP-signal is assigned to "pump", "probe" or "pp" depending on the chopper signal.

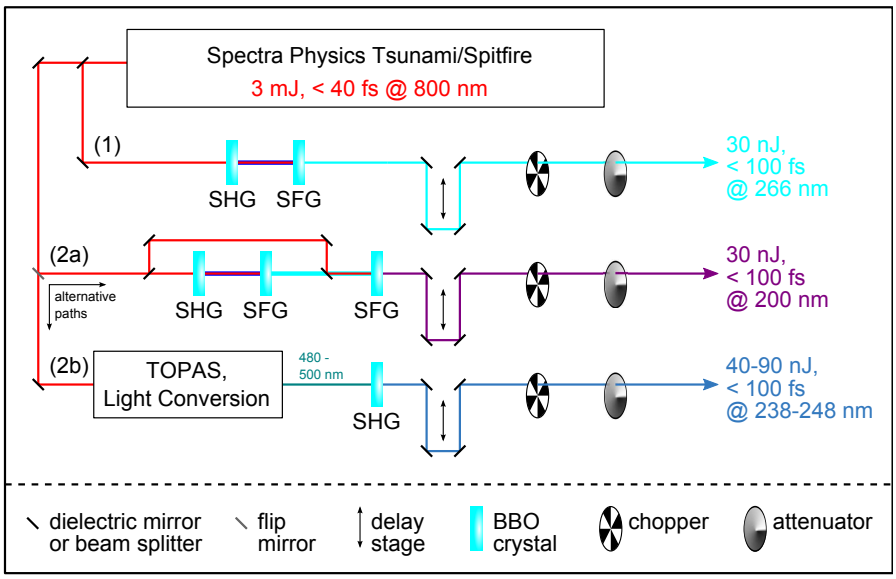

Figure 3.6. A commercial Ti:Sapphire laser generates sub-40 fs pulses at 800 nm wich are split into two parts. The first part (1) is used to generate 266 nm pulses by second harmonic generation (SHG) and sum frequency generation (SFG) in non-linear BBO crystals. The second part is either (2a) used to deliver pulses of 200 nm applying the same processes or, alternatively, (2b) yields tunable pulses in the wavelength range of about 480–500 nm from parametric processes in a TOPAS which is then frequency-doubled to give 238–248 nm pulses.

harmonic generation (SHG) and sum frequency generation (SFG) in beta barium borate crystals (BBO, thickness typically 0.2 mm). The second part can be used to generate the fourth harmonic by the same processes (2a). Alternatively, an optical parametric amplifier (TOPAS, Light Conversion) can generate visible pulses, which are frequency-doubled by another BBO crystal (2b).

For experiments with sodium iodide solution aiming at studying the solvated electron, the third and fourth harmonic of the fundamental were used (paths 1 and 2a). For experiments with solutions containing DNA bases, paths 1 and 2b were used. To allow for counting mode detection, the pulses have to be attenuated to 30–90 nJ pulse energy. We use neutral density filters (Thorlabs, NDC-50C-4) to attenuate the pulse energy. The pulse duration at the liquid jet position is below 140 fs in all cases.

A chopper wheel (Thorlabs, MC2000 Optical Chopper System, blade MC1F10) is inserted into each beam path to eliminate two subsequent pulses and let the next two pulses pass. The two wheels are phase-shifted by one pulse as indicated in Figure 3.5 to allow for separate detection of the one-colour signals.

An aluminium coated spherical mirror with about 30 cm focal length focuses both pulses onto the liquid jet. The focal beam waist is estimated to be on the order of about 100 µm.

3.4. Alignment and calibration

3.4.1. Spatial and temporal overlap

In order to align the spectrometers, a lot of parameters have to be considered. The liquid jet and the light pulses have to intersect in the highly divergent field of the permanent magnet in such a way that the photoelectrons can enter the spectrometer. To achieve this, most parts are movable: the jet is mounted on a manipulator (all three dimensions), light pulses can be aligned by simply moving mirrors outside the chamber and the magnet is mounted on three motorized linear translation stages in order to move the magnet in all three dimensions.

First, the liquid jet has to be positioned beneath the spectrometer entrance (orifice of 500 µm). The proper lateral position of the jet beneath the spectrometer entrance is found by maximizing the pressure in the spectrometer. The pump and probe pulses have to be overlapped with the liquid jet, individually, and then the overlap between the two pulses has to be established. The strategy for this is to make the pulse position on the jet visible. Then the individual spots caused by each of the pulses can be observed with a camera through the telescope (see Figure 3.1) and thus can easily be overlapped. There are two options to make the pulses visible on the jet. Firstly, a solution containing

a fluorescent dye which absorbs light in the UV/Vis range. A sample candidate is fluoresceine which fluoresces in the green when UV/Vis pulses hit the liquid jet. Secondly, enhanced light scattering is observed when pulses of higher intensities hit the droplets behind the laminar flow region of the jet. Fine adjustment is reached by overlapping the images of the individual photoelectron sources of both pulses on the phosphor screen (see Figure 3.4).

For finding the temporal overlap, we typically excite a long-lived state and scan the delay range looking for a step function in the intensity of the signal. One sample candidate for a long-lived signal is for example an alkali iodide salt solution which has the so-called charge-transfer-to-solvent states at about 200 and 240 nm excitation wavelength leading to generation of a solvated electron with a good signal to noise contrast (for details see Chapter 4).

3.4.2. Calibration of the time-of-flight spectrometer

The time-of-flight spectrometer measures the time an electron needs to arrive at the detector with respect to an external trigger (given by a photodiode that picks up a back reflection or losses from a dielectric mirror). To convert the time of flight into electron kinetic energy, the spectrometer has to be calibrated. For this purpose, the spectrum of nitric oxide (NO) gas is measured and the individual peaks are assigned to kinetic energies. In Figure 3.7 (left panel), photoelectron spectra of nitric oxide are shown for two different wavelengths: 200 nm and 266 nm. The spectra reveal the vibronic transitions from the vibrational and electronic ground state of NO ($X^2\Pi_{1/2}$, $\nu'' = 0$, $J'' = 1/2$) into different vibrational levels of the ionic state of NO^+($X^1\Sigma^+$, $\nu^+ = 0 - 32$, $N^+ = 0$). These states have ionization energies between 9.24 eV and 16.80 eV [40]. The applied photon energies are 6.20 eV (200 nm) and 4.66 eV (266 nm). Hence, two to three photons have to be absorbed to perform these transitions. Due to wavelength-dependent multi-photon ionization cross-sections, the intensity distribution may be totally different as compared to the intensity distribution obtained by one-photon ionization in Ref. [40].

The 200 nm spectrum of NO shows 10 vibronic bands ($\nu^+ = 0 - 9$) at TOF between 800 and 1200 ns. Those stem from a two-photon process. At large TOF (>1800 ns), photoelectrons from reflected trajectories show up – clearly exhibiting a very similar intensity distribution as the ones from direct trajectories. These reflected electrons are not considered for calibration. The width of the peaks increases with TOF because the TOF depends quadratically on the electron kinetic energy (see Equation 3.5). Hence, at small TOF two equally spaced energy points will appear closer together than at larger TOF.

The 266 nm spectrum shows 4 vibronic bands ($\nu^+ = 0 - 3$) at TOF between 700 and

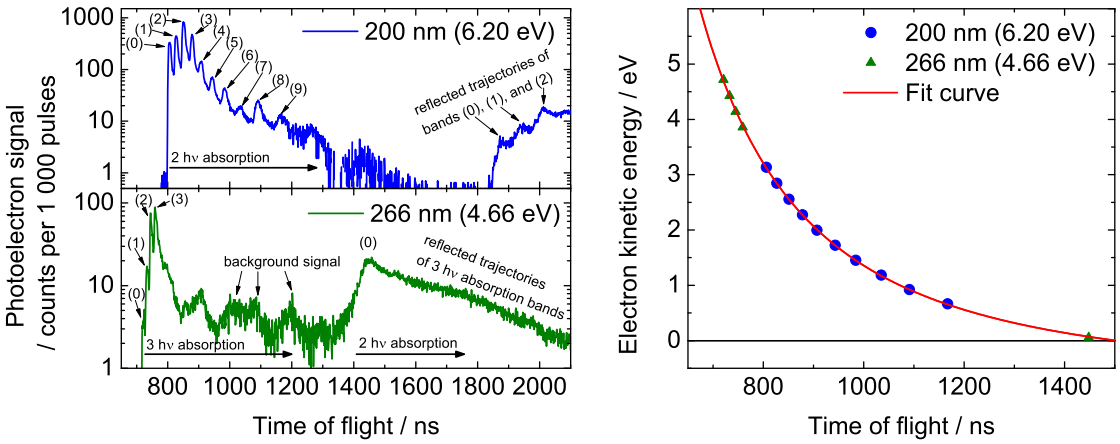

Figure 3.7. Calibration of the spectrometer using nitric oxide (NO) gas. **Left:** Photoelectron spectra of NO obtained by multi-photon ionization with 200 nm (blue) and 266 nm pulses (green). The bands are assigned to the vibronic transitions from the NO ground state to the NO^+ ion. Note that the y-axis is scaled logarithmically. **Right:** For each vibronic transition, the expected electron kinetic energy according to equation (3.4) is plotted against the corresponding time of flight in the NO-spectrum. Corresponding ionization energies are taken from Ref. [40]. Equation (3.5) is fitted to these points in order to extract the calibration parameters of the spectrometer. Note that the calibration holds only for the direct electron trajectories.
These results were published in Ref. [15].

800 ns due to 3-photon photoionization of NO. In this spectrum, a single contribution from the 2-photon ionization of NO into the first vibronic band ($\nu^+ = 0$) appears at $\gtrsim$1400 ns TOF. This feature overlaps with contributions from the reflected trajectories from the 3-photon process appearing at >1600 ns.

Each of the peaks observed in the NO spectra is assigned to the electron kinetic energy (E_{kin}) calculated from the referenced ionization energy (IE) according to

$$E_{\mathrm{kin}} = n\hbar\omega - IE, \tag{3.4}$$

where n is the number of absorbed photons with photon energy $\hbar\omega$ and IE is the ionization energy for the transitions $NO^+(X^1\Sigma^+,\ \nu^+ = 0-9,\ N^+ = 0) \leftarrow NO(X^2\Pi_{1/2},\ \nu'' = 0,\ J'' = 1/2)$ [40]. These electron kinetic energies are then plotted versus the corresponding TOF observed in the spectrum. The correlation between TOF (t) and kinetic energy is given by the following equation:

$$E_{\mathrm{kin}} = \frac{1}{2} m_e \left(\frac{s_0}{t - t_0}\right)^2 - E_0. \tag{3.5}$$

In this equation, m_e is the electron rest mass. The fit parameters are s_0, being the distance that the electrons have to cover, t_0, which is the time between the start of data acquisition (trigger signal) and photoelectron generation, and E_0, which is an energy

offset. From the example given in Figure 3.7, the following fit values were extracted: $s_0 = (0.62 \pm 0.01)\,\mathrm{m}$, $t_0 = (252 \pm 8)\,\mathrm{ns}$, and $E_0 = (0.78 \pm 0.04)\,\mathrm{eV}$. The fit value $s_0 = (0.62 \pm 0.01)\,\mathrm{m}$ nicely resembles the length of the first version spectrometer tube. For the second version of the TOF tube, the parameter s_0 is typically about 0.7 m. The time offset $t_0 = (252 \pm 8)\,\mathrm{ns}$ depends on the position of the photodiode providing the external trigger and the length of the connecting cable. It varies between the different beamtimes (slightly different set-ups) but is rather constant within one measurement session. The energy offset $E_0 = (0.78 \pm 0.04)\,\mathrm{eV}$ is due to small electric fields close to the interaction region which accelerate or decelerate all photoelectrons. These fields may be induced by tiny water droplets or salt crystals sitting on the magnet or at the nozzle surface. They depend on the exact position of the magnet and the nozzle. Due to the high sensitivity of the relative alignment of the liquid jet, laser and magnetic bottle, daily calibration of the spectrometer is required for reliable data.

Transforming the NO spectrum itself into kinetic energy, we can learn about the apparatus function of the spectrometer. When performing this transformation, the integral of the signal S has to be preserved by including the Jacobian factors.

$$\int S(E_{\mathrm{kin}})\,\mathrm{d}E_{\mathrm{kin}} = \int S(t)\,\frac{\partial E_{\mathrm{kin}}}{\partial t}\,\mathrm{d}t \tag{3.6}$$

$$S(E_{\mathrm{kin}})\mathrm{d}E_{\mathrm{kin}} = S(t)\mathrm{d}t \cdot \frac{m_e s_0^2}{(t-t_0)^3} \tag{3.7}$$

Figure 3.8 shows the energy-calibrated NO spectrum obtained by two-photon ionization with 200 nm pulses. Since the rotational bandwidth is narrow, the measured peak shape is dominated by the apparatus function. The individual bands are not symmetric with respect to their central kinetic energy. Indeed, there is a significant contribution towards low kinetic energies at each peak. The peak shape could be reproduced by the sum of a Gaussian and an exponentially decreasing shoulder towards lower electron kinetic energies:

$$\mathrm{Signal} = \begin{cases} G_0 e^{-\frac{(E_{\mathrm{kin}}-E_0)^2}{\Delta E_G^2}} & \text{for} \quad E_{\mathrm{kin}} > E_0 \\ G_0 \left(A e^{-\frac{(E_{\mathrm{kin}}-E_0)^2}{\Delta E_G^2}} + (1-A) e^{\frac{E_{\mathrm{kin}}-E_0}{\Delta E_E}} \right) & \text{for} \quad E_{\mathrm{kin}} \leq E_0; \quad 0 \leq A \leq 1 \end{cases} \tag{3.8}$$

where G_0 is the peak amplitude, E_0 is the peak position, ΔE_G is the width of the Gaussian part of the apparatus function, ΔE_E the exponential tail towards low kinetic energies, and A is the weight of the Gaussian part to the entire apparatus function.

For vibronic bands according to $\nu^+ = 0 - 8$, this function was fitted to the spectrum (see Figure 3.8). The corresponding fit parameters are given in Table 3.1. The values

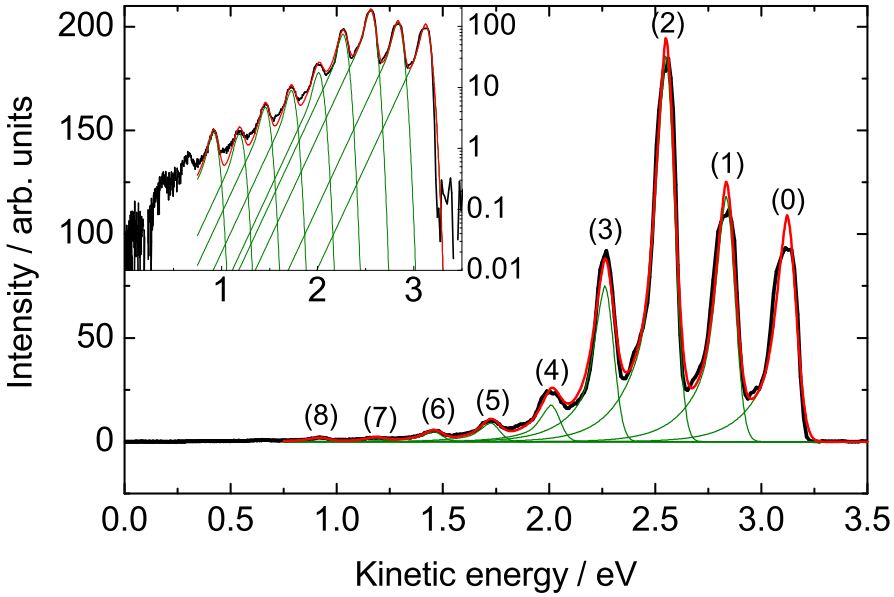

Figure 3.8. Photoelectron spectrum of NO in the gas phase obtained by 2-photon photoionization with 200 nm pulses. The experimental data (black) is well reproduced by the sum of vibrational bands (green) in the NO^+ ion, convolved with an instrument function as given in equation (3.8) where parameters ΔE_G, ΔE_E and A were treated as common parameters for all peaks. The inset shows the same data and fit lines on logarithmic scale and reveals the good match for the low-intensity peaks. These results were published in Ref. [15].

Table 3.1. Kinetic energy dependent fit parameters for the apparatus function (Equation 3.8) for the transition from the NO ground state into the ν^+-vibrational state of the ion. The last column gives the resolving power $\Delta E_{\mathrm{FWHM}}/E_0$ of the instrument where $\Delta E_{\mathrm{FWHM}} = 0.13(3)$ eV is a combination of ΔE_G and ΔE_E according to Equation 3.8.

ν^+	E_0 / eV	G_0 / arb. un.	$\Delta E_{\mathrm{FWHM}}/E_0$ / %
(0)	3.120(1)	109(2)	4(1)
(1)	2.833(1)	118(2)	5(1)
(2)	2.549(1)	186(2)	5(1)
(3)	2.261(1)	75(2)	6(1)
(4)	2.007(5)	18(2)	6(2)
(5)	1.723(9)	9(1)	8(2)
(6)	1.45(2)	5(1)	9(2)
(7)	1.18(4)	1.8(9)	11(3)
(8)	0.92(3)	1.8(8)	14(4)

for ΔE_G, ΔE_E and A which determine the resolution of the spectrometer were treated as common for all peaks and determined to $\Delta E_G = 0.061(2)$ eV, $\Delta E_E = 0.13(1)$ eV and $A = 0.39(5)$. Since these values are equal for all the peaks, the full width at half maximum ΔE_{FWHM} is constant for all the peaks and can be calculated using Equation 3.8. From the values given here, a $\Delta E_{\mathrm{FWHM}} = 0.13(3)$ eV is determined. Hence, the resolution of the spectrometer does not depend significantly on the kinetic energy of the electron in the

range of this investigation. The resolution $\Delta E_{\mathrm{FWHM}}/E_0$ of the spectrometer is about 4-6 % between 2 and 3 eV. The exponential tail of the peak corresponds to electrons originating from the same transition but which are detected at later times. This later detection can have two reasons: either the electrons lose kinetic energy on their way to the detector or they arrive later due to longer trajectories in the magnetic field. Kinetic energy-loss would mean that the electrons are scattered inelastically. As this spectrum was taken from gas phase sample with a maximum pressure of $2{\cdot}10^{-3}$ mbar, this channel is negligible (see mean free path at this pressure in Table 2.1). Hence, the electrons arrive later due to longer trajectories: electrons emitted along the magnetic field lines are fastest, while electrons emitted under an angle may fly longer trajectories into the flight tube and therefore arrive later (see Section 3.2).

The width of the apparatus function is considerably smaller than the photoelectron bands from liquid samples. Photoelectron spectra of molecules in solution are inhomogeneously broadened due to the high density of molecules leading to typical FWHM of about 1 eV being a factor of 10 wider than ΔE_{FWHM} of the apparatus function (see Table 3.1). Therefore, the apparatus function has no influence on the actual shape of the photoelectron spectra in condensed phase.

3.5. Preparation of sample solutions

DNA bases dissolved in water have different properties at different pH-values. A buffer is used to keep the pH-value constant at a given value even if the DNA base is added. As buffer system, we chose tris(hydroxymethyl)aminomethane / hydrochloric acid (TRIS/HCl) because it does not absorb UV light.

The storage bottles have a capacity of 280 ml liquid sample - enough for about 9 h of data-acquisition time. For a solution containing 1 mmol/l DNA base, the appropriate amount of powder and 490.9 mg (30 mmol/l) sodium chloride are dissolved in 278 ml water and 2 ml of the buffer stock solution (see below) is added.

For the buffer stock solution, 4.2259 g TRIS was dissolved in 200 ml demineralized water. Then HCl solution (1 mol/l) was added until the pH-cathode showed a pH value of 8 (about 15 ml HCl solution was used). Afterwards the solution was filled up to 250 ml. 2 ml of this solution were added to each DNA-solution (1 mmol/l) to keep the pH at 8.

The sample solution is prepared using demineralized water which has a residual conductivity of below 0.25 µS/cm.

4. The solvated electron

A solvated electron is a single, free electron in solution (e^-_{solv}). Polar solvents form a solvation shell around this electron – as they do for ions, too. The solvated electron appears in a variety of polar solvents. It is a potent reagent in chemistry and biology. A solvated electron can be formed by radiolysis of a solvent and therefore is a species that may also appear when photo-exciting molecules in water by UV light. Depending on the photon energy and pulse intensity, the (time-dependent) signal of solvated electrons will contribute to – or even dominate – the measured time-dependent signal. It is therefore necessary to disentangle the solvated electron contribution from the excited state dynamics of molecules. We therefore first concentrate on the solvated electron and evaluate its spectral and temporal behaviour before studying the excited state dynamics of the DNA bases in the next chapter.

4.1. Properties of hydrated electrons

In 1962, Hart and Boag discovered the solvated electron in water [41]. They measured the absorption spectrum of water and aqueous solution after an electron beam of 1.8 MeV electrons has interacted with the liquid. They found a broad absorption peaking at about 700 nm with a long tail in the visible wavelength range. Comparison with spectra from alkali metals dissolved in ammonia and reduced signal in presence of electron scavengers let them conclude that they observed a solvated electron in water. They called the solvated electron in water "hydrated electron" (e^-_{hyd}). Hydrated electrons have a rather short lifetime as compared to solvated electrons in ammonia which were already discovered about 100 years earlier [42]. Hydrated electrons can be generated by photoionisation of a solvent molecule (e.g. water [43, 44]), or by photoionisation / photodetachment of solutes (e.g. iodide [43, 45, 46] or chloride [47]). Especially, iodide is a prominent candidate, because its charge-transfer-to-solvent (CTTS) transition is in the UV wavelength region which is easily accessible. For smaller halide ions, the CTTS absorption shifts to the VUV region which is less feasible. From these experiments, we know that after formation of a hydrated electron, first the solvent shell reorients around the new charge (typical relaxation time ~ 1 ps), and a geminate pair of electron and radical is formed. Then, this geminate pair can either recombine to the precursor or it dissociates and

forms a free e^-_{hyd}. The recombination rates depend on the precursor and on the presence of electron scavengers [43, 47–49]. In case of an iodide precursor, Kloepfer *et al.* found no influence of the salt concentration (in the range of 600 µM – 200 mM) on the observed rates [43]. Sheu and Rossky investigated iodide photodetachment by quantum simulations [50]. They described two detachment channels. Most of the electrons are formed *via* a CTTS process, remain bound in a contact pair and recombine quickly. But about 10 % of the electrons reach a solvent void of proper structure by non-adiabatic tunnelling.

Until 2010, when the first photoelectron spectrum of a hydrated electron was published [15, 17, 35, 36, 51, 52], the electronic structure of hydrated electrons has only been accessible by cluster measurements [53–56]. Water clusters containing excess electrons were produced in different ways: neutral clusters containing alkali metals which form charge separated centres (e.g. [53]) or negatively charged clusters of pure water molecules with an excess electron (e.g. [57, 58]). A general observation from experiments with negatively charged clusters is that the excess electron is stronger bound for increasing cluster size. Hence, Coe *et al.* argued that extrapolating the size of the cluster to infinity would yield the bulk value for the binding energy of the hydrated electron [57]. In subsequent experiments [56, 58, 59], different vertical detachment energies for the same cluster size were found and assigned to different isomers: an isomer with an internal electron with highest vertical detachment energy and some isomers with electrons bound to the surface of the cluster with lower vertical detachment energies. Extrapolation to infinite cluster size then led to the speculation about a fully solvated electron in the bulk with vertical detachment energy of about 3.2 eV (or even up to about 4 eV [58]) and a partially solvated electron at the surface with a significantly lower vertical detachment energy of about 1.6 eV. There is an ongoing discussion in the literature about the nature of these two species [58, 60, and references therein].

In 2010, a number of groups (Abel [17], Neumark [36], Suzuki [35, 51] and our own studies [15, 52]) published their results concerning the binding energy of the hydrated electron in liquid water and its solvation dynamics. A binding energy of 3.3–3.6 eV has been found. I will first present my results (Sections 4.2 and 4.3) and then compare them to the results from Abel, Neumark and Suzuki in Section 4.4.

Parallel to these new contributions from experimentalists, Larsen *et al.* raised the question whether or not the hydrated electron occupies a cavity at all [61]. This approach has raised immediate controversy [62, 63] and is still discussed [64–66].

4.2. One-colour multi-photon photoelectron spectra of NaI in solution

For non-resonant multi-photon processes, the one-colour spectra reveal the ground state energies of the species present in the sample solution. Due to the low photon energy of UV-light (about 4–6 eV), the observed photoelectrons will result from two- or three-photon processes. This does not influence the observed kinetic energy of the photoelectrons as long as there is no resonant intermediate state. But ionisation cross-sections can be different compared to one-photon ionisation. In presence of a resonant intermediate state, nuclear dynamics may quickly lead to structural relaxation of the molecule increasing the binding energy of this intermediate state and thereby decreasing the observed photoelectron kinetic energy.

Figure 4.1 shows the absorption spectrum of iodide in aqueous solution (left) and an energy diagram of the species present in a sodium iodide solution (right). The first two bands of the iodide absorption spectrum are assigned to CTTS transitions from the closed shell iodide anion I^- into two different spin-orbit states of the neutral iodine radical $I(^2P_{3/2})$ and $I(^2P_{1/2})$. In agreement with the vacuum spin-orbit splitting [69], these two transitions are separated by almost 1 eV. Due to the spin-orbit splitting of the iodine radical, there are two different vacuum levels. Photodetachment of iodide therefore leads to two contributions in the photoelectron spectrum, corresponding to the $I(^2P_{3/2})$ and the $I(^2P_{1/2})$ radical. The $I(^2P_{1/2})$ is stronger bound by about 1 eV, resulting in less kinetic energy photoelectrons. Therefore, with 266 nm pulses (4.65 eV), two contributions due to two-photon photoionisation of iodide are expected. Additionally, three-photon photoionisation of water is also possible. With 200 nm pulses, however, a signal due to direct two-photon ionisation of iodide is not expected because iodide has a high probability to populate the CTTS state with only one photon. As soon as the CTTS state is populated, a solvated electron is formed immediately (for a detailed discussion, see Section 4.3). The spectrum obtained for the 200 nm pulses is therefore expected to also contain the initial distribution of solvated electrons. Since 4.65 eV photon energy (266 nm) is below the iodide absorption band, generation of solvated electrons with these photons is excluded.

Figure 4.2 shows the measured spectra obtained by multi-photon ionisation with either 200 nm or 266 nm pulses. The spectra can be reconstructed by fitting Gaussian contributions of the different species that are present in the solution. For these reconstructions, the peak positions were kept constant at the expected kinetic energies given in Table 4.1. Figure 4.2A shows the spectrum obtained with a 200 nm pulse (6.20 eV). This pulse can ionise liquid water in a two-photon processes (ionisation energy 11.16 eV [16]) and photodetach iodide also by two photons (photodetachment energy 7.85 and

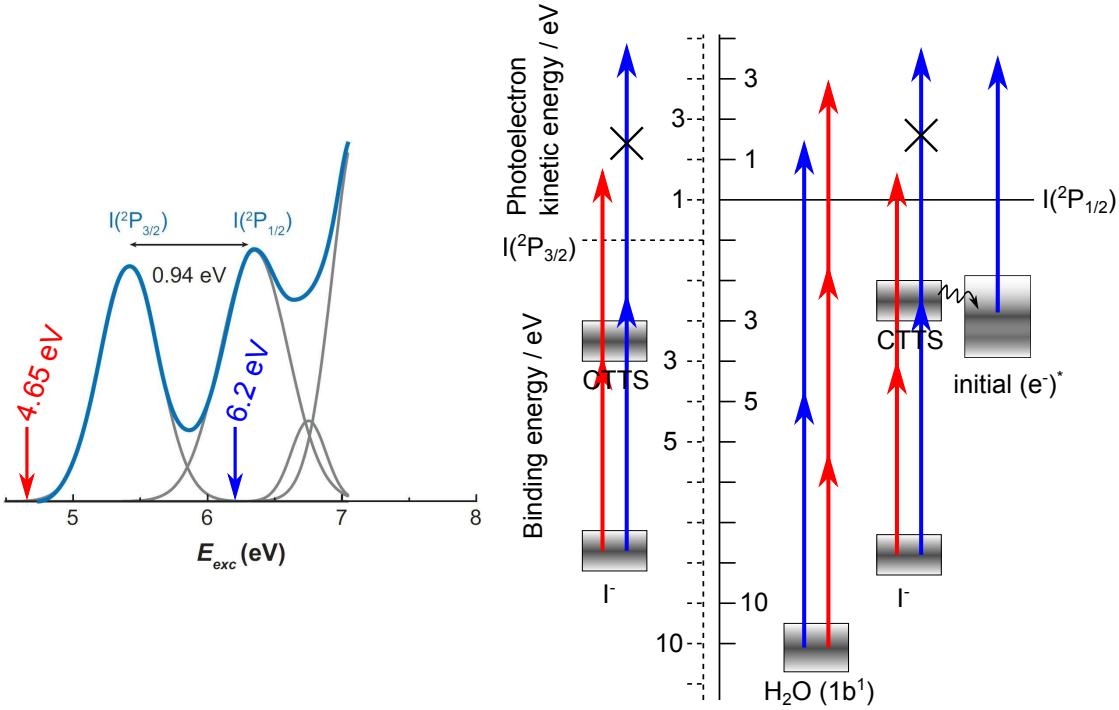

Figure 4.1. Left: Absorption spectrum (blue) of iodide in aqueous solution [67, 68]. The first two bands are assigned to transitions from the closed shell iodide anion into two different spin-orbit states of the neutral iodine radical with a diffuse CTTS electron. Figure taken from Ref. [68]. **Right:** Energy diagram of the species which are important for the assignment of the one-colour signals. Due to spin-orbit splitting two different vacuum levels with an energy difference of almost the vacuum spin-orbit splitting of 0.94 eV [69] exist for the $I(^2P_{3/2})$ (left, dashed lines) and $I(^2P_{1/2})$ (right, solid lines) radicals. Two-photon photodetachment of the iodide is possible for pulses with a photon energy of 6.2 eV (blue arrows) and 4.65 eV (red arrows). Due to the efficient one-photon excitation of the CTTS state by the 6.2 eV photons and subsequent highly efficient formation of hydrated electrons, a signal due to two-photon ionisation of iodide may not be observed. Instead, a contribution of the solvated electron formed within the pulse duration may appear (for details see Section 4.3).

8.8 eV for transition into the $I(^2P_{3/2})$ and $I(^2P_{1/2})$ states [32]). But absorption of one photon of 6.2 eV energy populates the CTTS state which rapidly decays forming solvated electrons which can be photodetached by another photon and contribute to the spectrum. Hence, also the solvated electron signal at very early times has to be included. As will be discussed in Section 4.3, we observe two contributions that can be assigned to the initial solvated electrons ("hot" e^-_{solv} and "cold" e^-_{solv} with a binding energy of 3.5 and 2.4 eV, respectively). Direct two-photon ionisation of iodide would contribute to the spectrum at a kinetic energy around 3.6 and 4.5 eV for ionisation into the $I(^2P_{1/2})$ and $I(^2P_{3/2})$ final states, respectively. A small contribution around 3.6 eV might be hidden in the signal but, especially at 4.5 eV, there is no indication for a contribution. This observation is explained in the following way: Due to the very efficient one-photon

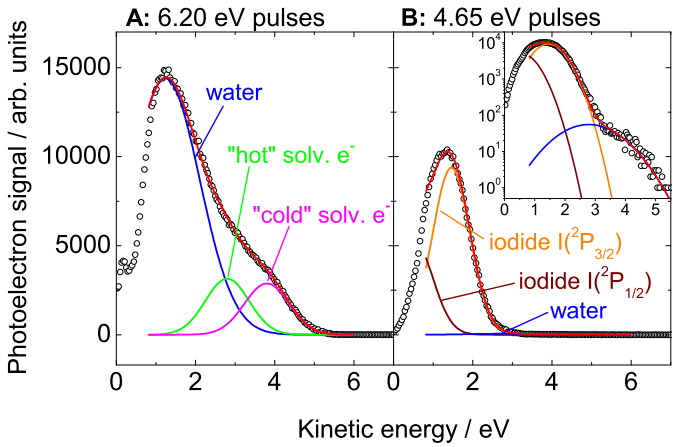

Figure 4.2. One-colour multi-photon photoelectron spectra of a 100 mM sodium iodide solution obtained with 200 nm (A, 6.2 eV) and 266 nm pulses (B, 4.65 eV). The signal (open circles) can be reproduced by a Gaussian fit (red) including signals from ionisation of the water $1b_1$ level (blue), iodide (brown and orange for ionisation into $I(^2P_{1/2})$ and $I(^2P_{3/2})$, respectively), and the "cold" (green) and "hot" solvated electrons (magenta). The inset shows the same data on a logarithmic scale.

Table 4.1. For all species present in NaI solution, the binding energy (taken from the given Refs.) and the expected photoelectron kinetic energies due to absorption of n photons are listed. These values are used to reproduce the complex signal of the one-colour spectra in Figure 4.2. Values in parentheses are given for completeness but do not appear in the spectra. The binding energies of the solvated electrons are discussed in detail in Section 4.3. The photoelectron signal of solvated electrons is formally a two-photon process: a first photon populates the CTTS state of iodide which rapidly decays forming solvated electrons and a second photon photodetaches e^-_{solv}. Only the second photon contributes to the kinetic energy of the photoelectrons.

species	E_{bin} / eV	Ref.	6.2 eV pulses		4.65 eV pulses	
			n	E_{kin} / eV	n	E_{kin} / eV
iodide	7.85 ($I(^2P_{3/2})$)	[32, 69]	2	(4.54)	2	1.48
iodide	8.8 ($I(^2P_{1/2})$)	[32]	2	(3.6)	2	0.52
water	11.16 ($1b_1$)	[16]	2	1.24	3	2.79
"cold" e^-_{solv}	3.4	[52]	1+1	2.8		
"hot" e^-_{solv}	2.4	[52]	1+1	3.8		

absorption process in iodide and subsequent formation of solvated electrons, which can also be ionised with a single electron, the direct two-photon ionisation of iodide is not observed.

For the 266 nm spectrum of NaI solution (see Figure 4.2B, 4.65 eV) two-photon photodetachment of iodide and three-photon ionisation of water is expected. Again, there are two contributions from iodide due to the different final states. The expected kinetic energies are at 0.52 and 1.62 eV. The three-photon contribution from the water $1b_1$ band appears at 2.79 eV and is only visible in the logarithmically scaled inset of Figure 4.2B.

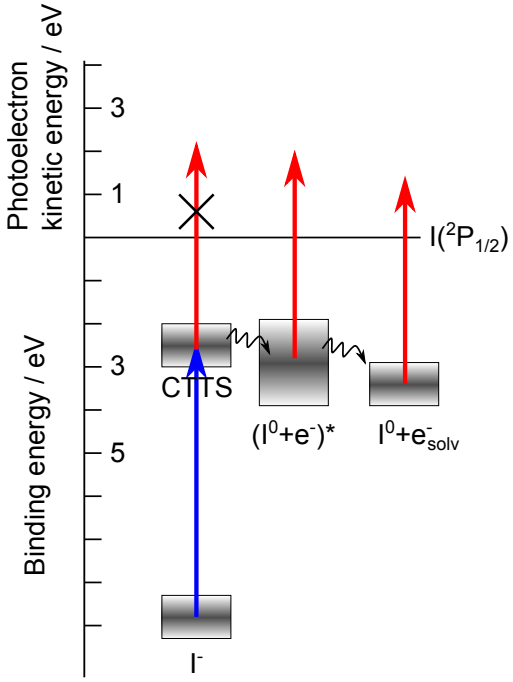

Figure 4.3. Energy diagram of the species which are important for the assignment of the time-dependent photoelectron signals of sodium iodide in aqueous solution. The CTTS is populated by absorption of a 6.2 eV photon (blue arrow) from the pump pulse. It evolves in time and leads to formation of a contact pair of iodine radical and excess electron $(I^0 + e^-)^*$, which finally thermalises to $(I^0 + e^-_{solv})$. The process is probed by delayed ionisation with 4.65 eV photons (red arrows).

4.3. Hydrated electrons from iodide photodetachment

Figure 4.3 shows the energy diagram for generation of solvated electrons by photodetachment of iodide ions. Absorption of a 6.2 eV photon (blue arrow) from the pump pulse leads to population of the CTTS state connected to the $I(^2P_{1/2})$ final state. The CTTS state evolves and a solvated electron is formed. If the excitation process is followed by a probe pulse with high enough photon energy (here: 4.65 eV, red arrow), the energy distribution of the solvated electrons can be projected onto the ionisation continuum and the temporal evolution of the photoelectron spectrum is accessible by delaying the probe *versus* the pump pulse.

Figure 4.4(left) shows the time-dependent photoelectron spectrum obtained from a 100 mM sodium iodide solution excited by a 6.2 eV pump pulse and ionised by a delayed 4.65 eV probe pulse. At the temporal overlap of the pump and probe pulses, we observe a very broad distribution of photoelectrons extending over electron kinetic energies from 0 up to more than 3 eV. Within the first picosecond, a time-dependent shift of the photoelectrons with high kinetic energies is observed. But the peak position stays almost

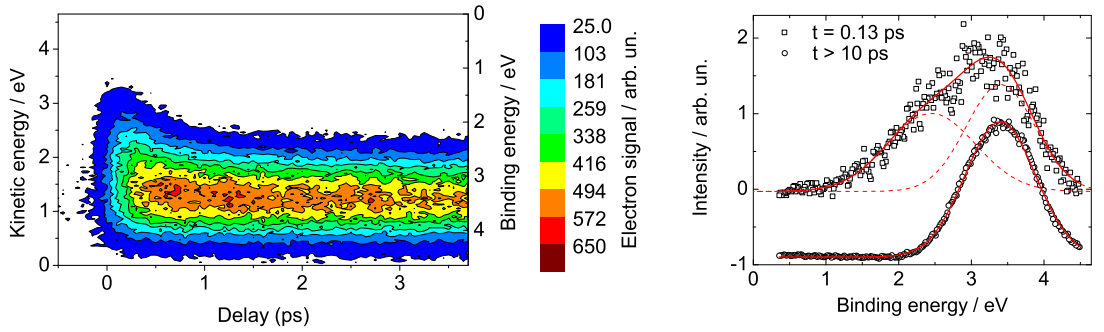

Figure 4.4. Time-resolved photoelectron spectrum of 100 mM sodium iodide solution excited with 200 nm and ionised with 266 nm pulses. **Left:** The two-dimensional plot shows a pronounced shift of the high kinetic energy photoelectrons occurring within the first picosecond. The one-colour signals have been subtracted. **Right:** Photoelectron spectrum at a pump-probe delay of 130 fs (squares) and > 10 ps (circles). The spectrum at large delays (> 10 ps) is well reproduced by a single Gaussian corresponding to the thermalised e^-_{solv} with a binding energy of 3.40 eV. The spectrum at $t = 130$ fs can be fitted by the sum of two Gaussians (dashed lines): one with the same position and width as the spectrum at long delays and a second contribution at lower binding energies which is broader. The two spectra are vertically displaced for clarity. Published in Ref. [52].

constant.

The right panel of Figure 4.4 shows a comparison between the photoelectron distribution at short and long delay times after excitation. At large delay times (> 10 ps, circles), the spectrum resembles a single Gaussian revealing the distribution of hydrated electrons in thermalised solvent geometries. This electron distribution is characterised by a center binding energy of 3.40 eV with a FWHM of 1.1 eV. At very short delays (here 130 fs, squares) however, the spectrum is much broader and can be well reproduced by the sum of two Gaussian contributions including one Gaussian of the same width and position as the spectrum at long delays. This observation suggests that already at 130 fs after excitation, there are some electrons that have high binding energies and therefore they must occupy sites for which the environment provides a favourable solvent structure. Consequentially, a fraction of e^-_{solv} is generated with a proper solvation shell (as predicted by Sheu and Rossky in 1993 [70], tunnelling channel). This is in contrast to earlier transient absorption measurements, where this tunnelling channel has not been observed. We call these electrons "cold" electrons (where "cold" refers to the solvent structure) because they appear in an environment which is already thermalised.

The second Gaussian contribution is centred at lower binding energy and is much broader. We call these only weakly solvated electrons "hot" electrons because they are initially located in an environment with an unfavourable solvent structure. In this case, the solvent molecules re-orient their dipoles according to the new charge distribution and thereby stabilise the hydrated electrons. In general, such a stabilisation process is

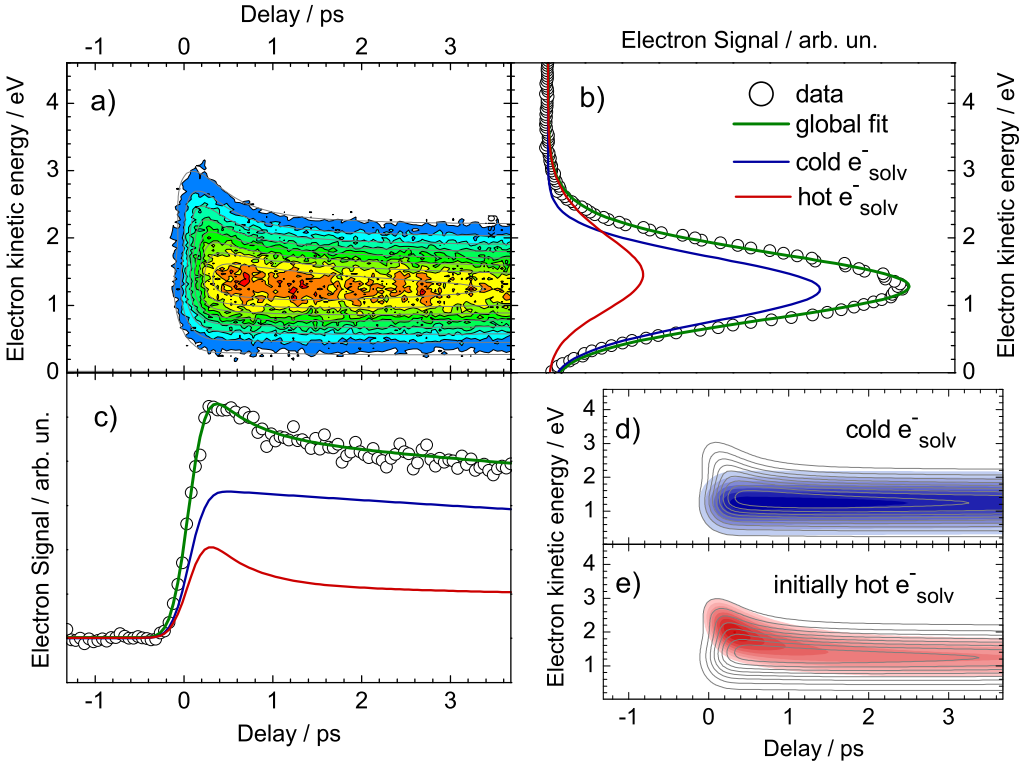

Figure 4.5. Results of a two-dimensional fit of two Gaussian contributions to the time-resolved photoelectron spectrum of 100 mM sodium iodide solution (200 nm pump, 266 nm probe). (a) Comparison of raw data (colour map) and fit (grey contour lines). In a global fit (lines), two transients of Gaussian shape are assumed and assigned to initially "hot" and "cold" electrons with corresponding spectra (b) and population dynamics (c). The contributions of hot and cold electron to the total signal is shown in (d) and (e). Published in Ref. [15].

connected with an increase in binding energy. Therefore, we assign the pronounced shift of the photoelectron spectrum within the first picosecond to the re-orientation of the water molecules, i.e. thermalisation.

In transient absorption, the electron solvation dynamics after photodetachment from iodide has been discussed using a sequential model [43, 49]. This model includes a stepwise transition from the initially excited CTTS state to a contact pair where iodine radical and ejected electron share a solvation shell, and finally the free solvated electrons and iodine radicals with their individual solvation shells. However, since the solvation dynamics observed for the solvated electrons are generally assigned to a re-orientation of surrounding water molecules, we rather preferred a model revealing this continuous process. Based on the spectra observed for different delays (see fight panel of Fig. 4.4), a two-dimensional fit to the data was performed. The results are shown in Figure 4.5. The data were analysed by a non-linear Levenberg-Marquard fit assuming Gaussian band shapes $S_i(E,t)$ for the photoelectron bands and exponential population dynamics

$P_i(t)$. Cooling processes are modelled as exponential shift of the band position and band width for the respective photoelectron band. The observed signal is the product of band shape and population dynamics, convolved with the laser cross-correlation $CC(t)$. The cross-correlation function was assumed to be of Gaussian shape. The signal $\mathrm{Sig}(E,t)$ is then the sum of the contributions of individual transients i:

$$\mathrm{Sig}(E,t) = CC(t) \otimes \sum_i [P_i(t) \cdot S_i(E,t)], \tag{4.1}$$

where the symbol $\otimes$ represents the convolution (for an explicit equation see Appendix A.1). Motivated by the observations described in the previous paragraph, we assumed two distinct populations representing "hot" and "cold" e^-_{solv}. The low kinetic energy part (high binding energy corresponding to the "cold" e^-_{solv}) of the spectrum has a temporally constant width and peak position. Hence, this component simply decays exponentially. The "hot" e^-_{solv}-part at higher kinetic energies (and lower binding energies) is initially free in position and width, but both parameters are time-dependent and approach the corresponding parameters of the "cold" e^-_{solv}.

The transient spectrum corresponding to the thermalised, "cold" electrons is centred at 3.4 eV binding energy with a FWHM of 1.1 eV. This population decays with a rate of $(22\,\mathrm{ps})^{-1}$ due to geminate recombination with the iodine radical. About 35 % of the thermalised electrons escape this fate by diffusion away from the iodine radical. These electrons recombine with other iodine radicals or hydronium ions (H_3O^+) on a µs time scale [41]. The second transient is due to "hot" electrons in an initially unrelaxed environment. This leads to a very broad signal at delay times around 0 ps in the time-resolved photoelectron spectrum (representing a large number of different water environments [68]). This "hot" electron transient thermalises on a ps-time scale: the photoelectron band position shifts from an initial binding energy of 2.35 eV towards that of the equilibrated electron and the bandwidth contracts slightly. This shift occurs with a rate of $(1.1\,\mathrm{ps})^{-1}$. A part of the hot electron population decays with a lifetime of 800 fs, probably due to geminate recombination. After 5 ps, no further spectral shift of photoelectrons is observed and the "hot" electrons have fully thermalised. There is no spectral evidence for an escape of the electron from its geminate radical. This can only be concluded from the kinetics.

In transient absorption experiments, the "initially cold" electrons have not been observed. One reason for this difference might be that the optical absorption may not be very sensitive to the local environment of e_{solv}. But since transient absorption is a bulk-sensitive method and my method is also sensitive to changes at the surface, an alternative explanation can be raised which assigns signal equivalent to TA signal to stemming from the bulk and the leftover to stemming from the surface. The distribu-

tion assigned to bulk hydrated electrons thermalise as observed in TA. These electrons are born with binding energies around 2.4 eV and approach 3.4 eV. They decay with a rate constant of $(22\,\mathrm{ps})^{-1}$. The second distribution assigned to electrons at the surface reveals a constant binding energy of 3.4 eV. They decay faster than bulk electrons with a lifetime of about 1 ps. The constant binding energy of hydrated electrons at the surface might be due to the limited degrees of freedom at the surface, which would lead to the same initial binding energy for all electrons and prevent time-dependent changes due to thermalisation.

The latter assignment to surface and bulk electrons was supported by later experiments. Using two solutions with different amounts of a surface-active cation, we studied the contribution from the surface relative to the bulk contribution [21]. For solvated electrons generated at (or close to) the surface, we found an additional sub-ps decay channel which was not observed in the bulk-sensitive TA studies. We therefore assign this sub-ps channel to solvated electrons that are generated close to the surface and recombine much faster with their geminate partner due to the limited degrees of freedom at the surface.

4.4. Comparison to results obtained by other groups

In 2010, a number of groups published their results on the binding energy of the solvated electron in liquid water. Figure 4.6 summarises the results on the so-called bulk solvated electron. Siefermann *et al.* used a precursor molecule ($K_4[Fe(CN)_6]$, 0.5 M) which is known to be repelled from the surface and only accumulates in the bulk [17]. Therefore, solvated electrons generated by excitation of these molecules should also predominantly appear in the bulk. Excitation occurs in a one-photon process at 266 nm (4.65 eV). The bulk solvated electrons are then probed using 32 nm pulses (38.7 eV). The observed vertical binding energy of 3.3 eV is in very good agreement with the binding energy of 3.4 eV which was measured in this work (see Section 4.3).

Tang *et al.* performed femtosecond time-resolved photoelectron studies on sodium iodide (NaI) solution [35, 51] and reported a binding energy for the hydrated electron of 3.3 eV (Fig. 4.6B). This is also in good agreement with the value of 3.4 eV measured in this work.

Shreve *et al.* used nanosecond UV laser pulses at 266 or 213 nm to study the photoelectron spectrum of potassium hexacyanoferrate ($K_4Fe[CN]_6$) and potassium iodide (KI) [36] in aqueous solution. They observe hydrated electrons generated by a two-photon process, where within one pulse the first photon excites the precursor generating solvated electrons via a CTTS state and the second photon ejects this electron into the vacuum. Since the time for equilibration of solvated electrons (~ 70 ps) is short com-

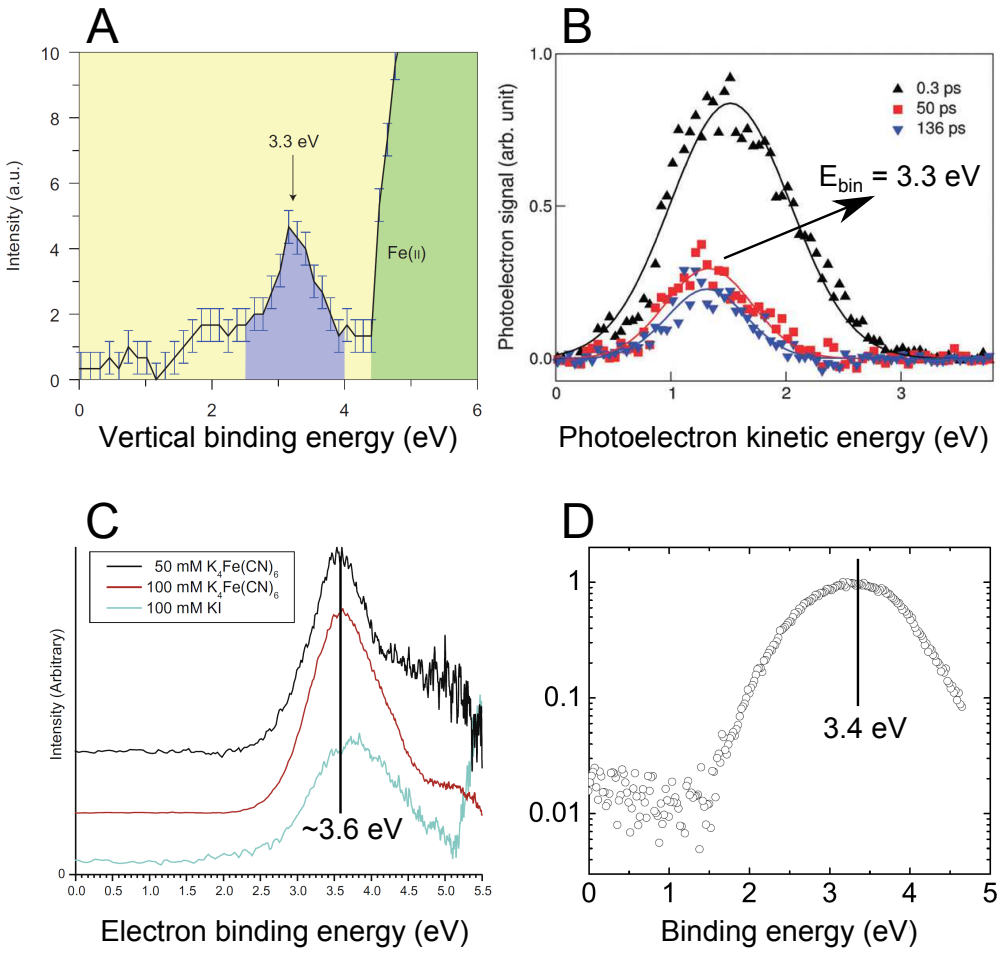

Figure 4.6. Comparison of photoelectron spectra of solvated electrons in water. A: Siefermann *et al.* found 3.3 eV binding energy upon 1-photon absorption in $[Fe(CN)_6]^{4-}$ with 266 nm pump and 32 nm probe pulses [17]. B: Tang *et al.* also found 3.3 eV binding energy, but upon 1-photon absorption of I^- with 243 nm pump and 260 nm probe pulses [51]. C: Shreve *et al.* found on average 3.6 eV binding energy upon 1-photon excitation of $[Fe(CN)_6]^{4-}$ and I^- with 213 nm pulses of ns-duration [36]. D: In this work, 3.4 eV binding energy was measured at delays >10 ps after excitation of I^- with 200 nm pulses.

pared to the pulse duration ($\sim$35 ns), the authors measure predominantly the signal of the fully relaxed hydrated electrons. They observe a single photoelectron band with an average binding energy of 3.6 eV for both precursors. This binding energy is slightly higher than the value of 3.4 eV obtained in this work. Comparing their results to the aforementioned results, Shreve *et al.* discuss experimental differences as delay schemes, temperature dependence, and inelastic scattering of the photoelectrons but find these reasons unlikely to explain the different results. They also exclude surface potentials evoked by electrokinetic charging. However, they do not discuss two-photon ionisation of the water molecules. The spectra in Figure 4.6C show at high kinetic energies an

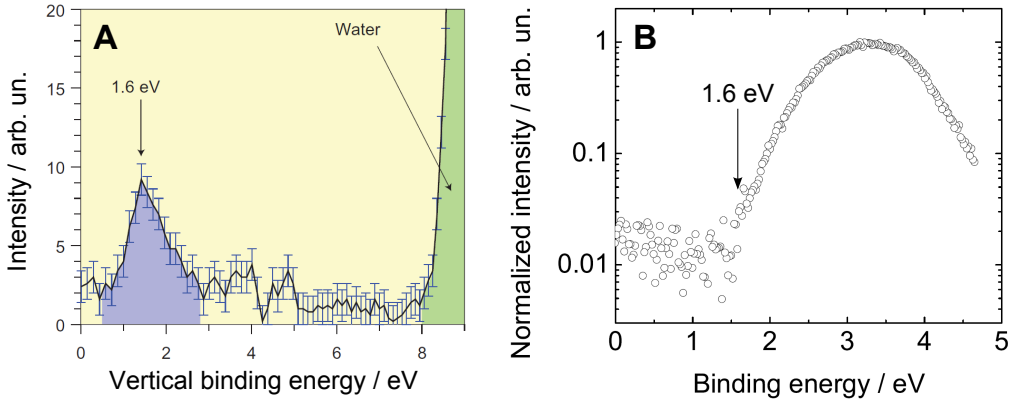

Figure 4.7. Comparison of photoelectron spectra of solvated electrons in water. A: The surface-bound solvated electron with 1.6 eV binding energy was generated by 2-photon absorption of water [17]. B: In this work, solvated electrons were generated by iodide photodetachment. This spectrum is the sum of all spectra taken at delays ≥10 ps. Despite the logarithmic scale, there is no hint for a contribution at 1.6 eV binding energy.

increasing feature with decreasing concentration. Given that the spectral shape of the photoelectron band changes with the concentration, a contribution of water itself may not be neglected.

Siefermann *et al.* also observed a surface-bound solvated electron as shown in Figure 4.7A. In this case, water molecules were excited in a 2-photon process with 266 nm pulses (4.65 eV). The two-photon absorption length is much longer than the probe depth, i.e. we can assume that the hydrated electrons are homogeneously generated over the probe volume. Siefermann *et al.* argue that using 32 nm (38.7 eV) probe pulses, they only probe the surface due to the small inelastic mean free path of the electrons in water. Therefore, they claim that no bulk signal is observed here. However, recent experimental studies on the electron range in water reveal a probe depth of about 2 nm at this wavelength [25, 71]. This is about seven times larger than the diameter of a water molecule. Hence, bulk solvated electrons should also appear in this spectrum.

In this work, we generated solvated electrons by photodetachment from a sodium iodide solution. Iodide is known to accumulate at the water surface. According to Siefermann *et al.*, the surface bound solvated electron has a lifetime longer than a hundred ps and therefore it should also appear in our time-resolved data. Figure 4.7C shows the average of all spectra at delays ≥10 ps on a logarithmic scale. There is no indication for a contribution at 1.6 eV binding energy despite our dynamic range of >1000 which is deduced from the integral of the signal. The measurements of Siefermann *et al.* are strongly discussed. A number of theoretical works have been published in the meantime which doubt the existence of a solvated electron with 1.6 eV [21, 65, 71, 72]. Although different groups spent some effort to reproduce the observations of Siefermann *et al.*,

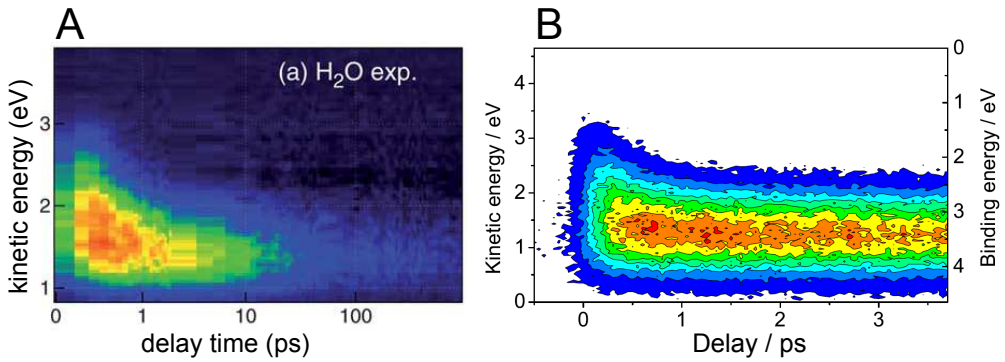

Figure 4.8. Comparison of two-dimensional plot of the time-resolved photoelectron spectra of solvated electrons in water generated by CTTS state excitation of iodide. A: Suzuki *et al.* excite the first CTTS state with 226 nm pulses and probe the dynamics with 260 nm (4.77 eV) [73]. Note the logarithmically scaled delay-axis. B: In this work, the second CTTS state was excited with 200 nm and probed with 266 nm. A qualitatively very similar solvation dynamics is observed.

their findings could not be reproduced, yet [21, 71]. But since Siefermann *et al.* were the only ones who directly excited water in order to generate solvated electrons, it cannot be excluded that the precursor molecule (or ion) is crucial. Hence, it the solvated electron with 1.6 eV binding energy might only appear if water molecules are excited with 4.65 eV pulses (two-photon process).

Suzuki *et al.* also studied the dynamics of the solvated electron [73]. They excited an iodide solution with 226 nm pulses (5.5 eV) into the lower CTTS state and followed the dynamics by ionisation with 260 nm. The two-dimensional plot of their time-resolved spectra appears qualitatively very similar to the spectra obtained in this work as a direct comparison in Figure 4.8 reveals. However, they analysed their data according to the model proposed from transient absorption experiments, namely in terms of three intermediate states on the path to the hydrated electron. First, excitation of the CTTS band of iodide would lead to a displacement of the electron cloud forming a contact pair within the same (original) solvation shell. Second, this contact pair dissociates forming a solvent separated state where water molecules have moved between the neutral iodine and the electron. And finally, the solvent separated state dissociates further forming a free solvated electron. They show spectra for each of the species discussed and the a number of lifetimes connected to their appearance and decay.

This interpretation therefore assumes the presence of these four discrete states that inter-convert. In our point of view this picture is not appropriate for dynamics in solution which is better described by a continuous picture. Each iodide ion or iodine-electron pair or hydrated electron experiences a slightly different and temporally changing environment. Even the nature of the CTTS state and its decay is better described by a

continuous picture: it is very diffuse and extends over several water molecules. It is immediately clear, that fluctuations of the water molecules will have a dramatic influence on the stability of this state. Indeed, Messina et al. find a broad distribution of CTTS decay times reflecting the highly inhomogeneous initial environments [74]. For this reason, we discarded the description with discrete states which is typically applied in gas phase spectroscopy, but we chose a continuous description as presented in Section 4.3.

5. Excited state dynamics of DNA bases and nucleosides

DNA bases are very photostable which is commonly ascribed to the existence of radiation-less decay channels. This is a very important property for living organisms because DNA bases are present in different biomolecules in living organisms. The most widely known is the deoxyribonucleic acid (DNA), which carries the genetic code. But they are also part of the RNA which is relevant for protein production and regulation. But they have also differing functions. For example, the DNA base adenine is part of the adenosine triphosphate (ATP) which responsible for the intracellular energy transfer. Guanosine triphosphate (GTP) is essential for signal transduction for specific proteins.

The existence of radiation-less decay channels in DNA bases is very important for living organisms, because it decreases their need for energetically costly enzymatic repair of the DNA. Another motivation to study the excited states of DNA is the ultrafast exciton transfer in DNA molecules which might be useful for potential applications in molecular electronics [75–77].

In the following sections, I will first give some general information on common aspects concerning the properties of the DNA bases and the data evaluation. Then, I will show and compare the one-colour signals of the nucleosides. And afterwards, I will discuss in detail the four DNA bases individually.

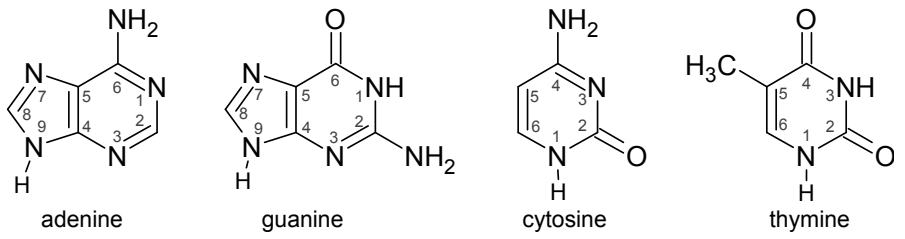

Figure 5.1. Chemical structure of the DNA bases.

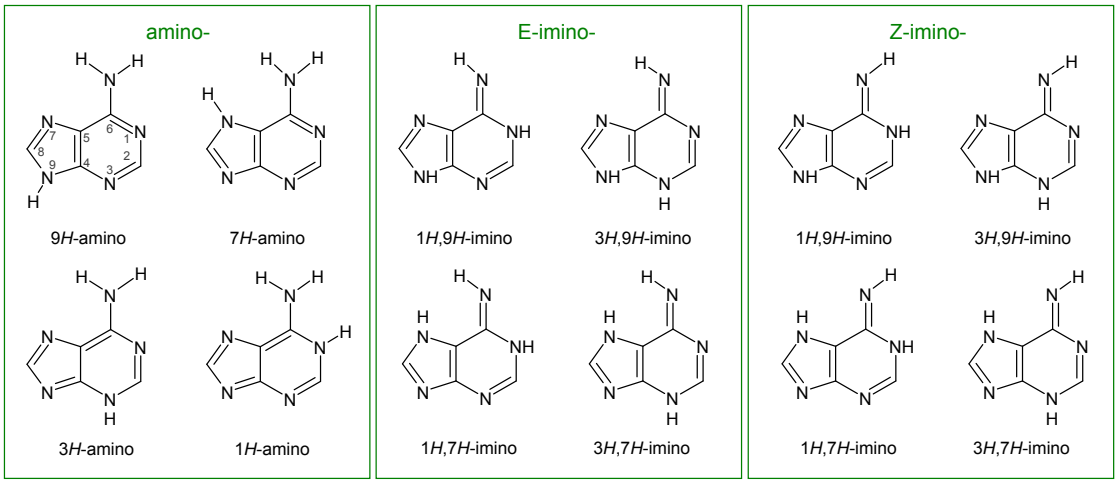

Figure 5.2. All possible tautomers of adenine. E- and Z-imino isomers are not equal due to the double bond connecting the imino-group to the $C6$ atom. Double bonds are not freely rotatable.

5.1. Introductory remarks

In Figure 5.1, the structure of the four DNA bases is shown. Natural DNA bases are aromatic heterocycles, two purines (adenine and guanine) and two pyrimidines (cytosine and thymine). According to international nomenclature, the ring atoms are numbered as given in the Figure 5.1. These numbers become relevant when the molecule is changed in a chemical reaction and the specific site has to be named, or when upon excitation nuclear rearrangement occurs changing the geometry of the molecule. In the ground state, the DNA bases are more or less flat with all heavy atoms lying in the same plane. Only the light hydrogen atoms of amino or methyl groups may stick out of the plane.

In contrast to carbon atoms, heteroatoms (here O and N) have free electron pairs where protons can easily be attached. The positive charge introduced by the proton can be neutralised by releasing a proton from another heteroatom and "flipping" bonds within the conjugated π-system. Conformational isomers, that quickly interchange mostly by migration of a single hydrogen atom or a proton are called tautomers. Due to the large number of heteroatoms present in the DNA bases, these molecules are prone to form tautomers. In adenine, there are three hydrogens attached to nitrogens. These hydrogens can easily move to another nitrogen accompanied by a change in the electron distribution in the aromatic ring. Theoretically, adenine can appear in twelve different tautomers as listed in Figure 5.2. These tautomers have different ground state energies and dipole moments, and therefore, are favoured or disfavoured in surroundings of different polarity. The electronic structure of tautomers can be very different and therefore, it is of importance to know, which tautomers exist in the present experiment. Additionally, if the excited state energies of two tautomers are similar, excitation of one tautomer can

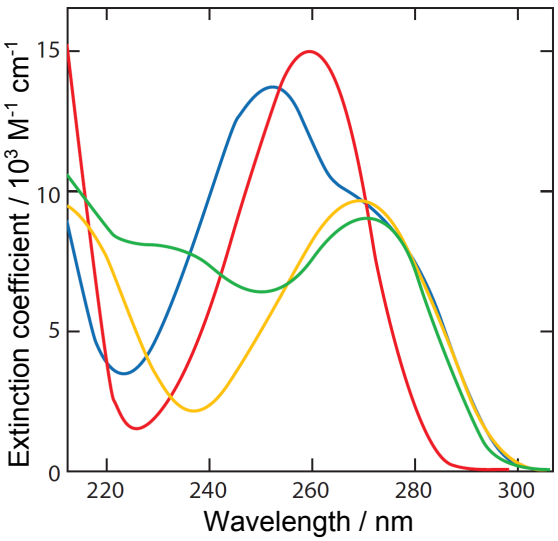

Figure 5.3. UV absorption spectrum of DNA bases in solution. red: adenine, blue: guanine, yellow: thymine, and green: cytosine.

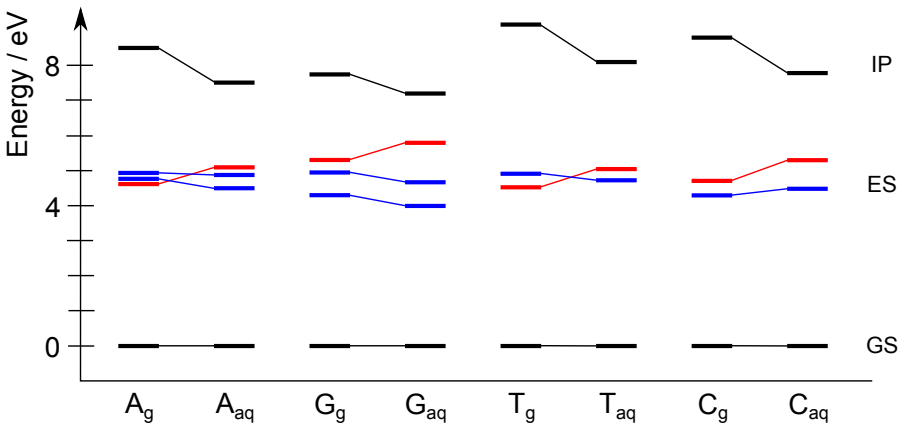

Figure 5.4. Vertical excitation and ionisation energies of the DNA bases in the gas phase and the solution (GS: ground state, ES: excited state, IP: ionisation potential). The optically bright $\pi\pi^*$ states are displayed in blue and the dark $n\pi^*$ states in red. For values and references see appendix A.2.

lead to excited state tautomerisation as has been observed by Kosma *et al.* [78].

In Figure 5.3, the absorption spectrum of the four DNA bases in aqueous solution is shown. The spectra of the different DNA bases are quite different, but they all show a broad absorption band in the ultraviolet region. The structure of the absorption spectrum gives some hints on the number of states lying in the Franck-Condon region. In the case of guanine for example (blue spectrum), the double-hump structure indicates that there are at least two bright states in the UV region.

Figure 5.4 shows the energies and character of excited states that are present in the Franck-Condon region of the isolated DNA bases and in aqueous solution (for values see

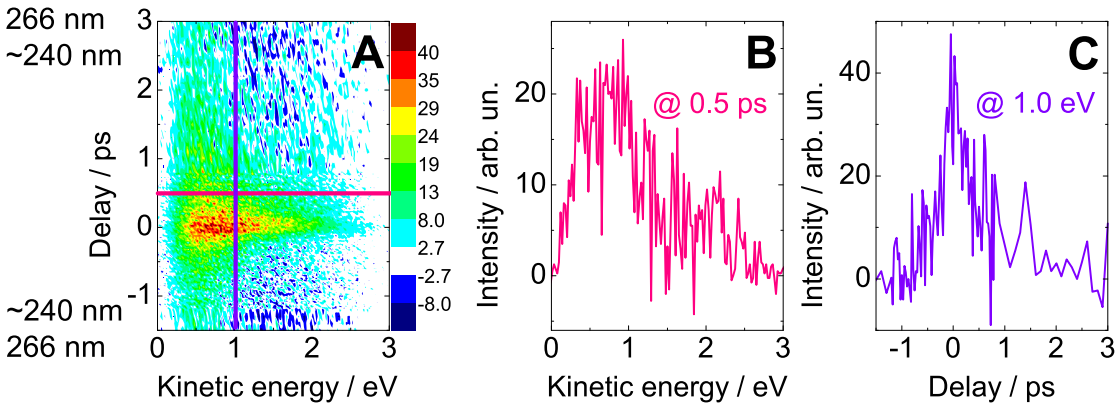

Figure 5.5. Two-dimensional contour plot of the time-dependent photoelectron spectrum for the example of guanosine in aqueous solution (A). The one-colour signals have been subtracted. Horizontal cuts give photoelectron spectra at a specific delay between pump and probe pulse (B). Vertical cuts give the time-dependent signal at a specific kinetic energy (C).

appendix A.2). In general, states with a larger dipole moment are stabilised in polar solvents such as water and therefore appear at lower energies. When going from the isolated base to the base in aqueous solution, the ππ* states (blue) are lowered in energy for most bases while the nπ* states (red) appear at higher energies.

As mentioned before, the absorption spectrum of the DNA bases is quite broad (see Figure 5.3). The wavelengths that are used for the experiments described in this work are 266 nm and around 240 nm. Pulses of either wavelength can be absorbed and can trigger the photoreaction. Hence, we expect a signal initiated by either pulse. Due to the set-up, we observe signal from excitation with 266 nm and ionisation with 240 nm at positive delays. At negative delay times, signal due to excitation with 240 nm and ionisation with 266 nm is observed. The measured signal will always be plotted in two-dimensional contour plots as shown in Figure 5.5A. The x-axis shows the electron kinetic energy and the y-axis the delay between both pulses. The colour is a measure for the number of photoelectrons at a given kinetic energy and pump-probe delay. Horizontal lineouts give the photoelectron spectrum of the excited molecule at a distinct delay. Vertical lineouts give the population dynamics at a distinct electron kinetic energy.

At long delays, we observe a slightly negative pump-probe spectrum which we assign to dead-time effects of the MCP detector working in counting mode. Figure 5.6 shows the photoelectron spectra of cytidine measured with 238 nm and 248 nm pulses at long positive (>3 ps, green) and long negative delays (<-2 ps, blue). Each spectrum is averaged over 20 individual spectra to improve the statistics. The error bars show the standard error of the mean. These spectra appear at delays where a time-dependent signal is not necessarily expected any more and persists for more than 150 ps. Additionally, the spectra are identical although the pump and probe wavelengths are interchanged. If

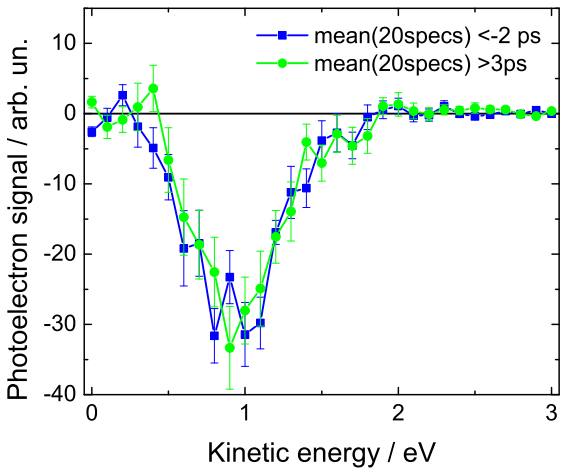

Figure 5.6. Measured time-dependent photoelectron signal of cytidine in solution at long positive (> 3 ps) and at long negative delays (< –2 ps). The data were taken with 266 nm and 249 nm pulses (40 nJ pulse energy, each). Each spectrum is an average of 20 individual spectra and the error bars are given by the standard error of the mean. The one-colour signals were subtracted. This bleach is about 4% of the total two-colour signal.

this slightly negative spectrum was due to a real long-lived signal (or bleach), it should depend on the probe photon energy and should not be identical if pump and probe pulse are interchanged. Therefore, this bleach signal is treated as an artefact without a physical meaning. This negative signal was included in the fit by an additional spectral offset which does not depend on time (see Appendix A.1).

From the intensity relation between signals at positive and negative delays, we can get additional information about the excited state absorption coefficients for different wavelengths. The following function was fitted to the data:

$$N(E_{\mathrm{kin}},t) = \sum_i a_i(E_{\mathrm{kin}})[P_i(t) \otimes G(t)], \tag{5.1}$$

where $a_i(E_{\mathrm{kin}})$ is the decay associated spectrum and $P_i(t)$ is the population dynamics of the contribution i convolved with a Gaussian cross-correlation function $G(t)$ (for an explicit fit function see equation A.7 in Appendix A.1). For exact fitting of the time-resolved data and exact retrieval of the excited state lifetimes, the cross-correlation width of the pump and probe pulses is crucial. In the calibration with NO (see Section 3.4) and when measuring the buffered NaCl solution, we obtain a non-resonant cross-correlation signal. Although the pulses are initially short, the width of this cross-correlation signal at the location of the liquid jet is about 200 fs (FWHM) for each of the two samples. Therefore, this parameter is kept constant at this value for all the fits discussed afterwards.

The amplitude of the signal $A_i = \int a_i(E_{\mathrm{kin}})\mathrm{d}E_{\mathrm{kin}}$ depends on the pulse intensities and

on the absorption cross-sections:

$$A \propto \alpha_{\mathrm{GS}}(\lambda_{pu}) \cdot I_{pu} \cdot \alpha_{\mathrm{ES}}(\lambda_{pr}) \cdot I_{pr}, \tag{5.2}$$

where in the pump step, the absorption coefficient of the ground state $\alpha_{\mathrm{GS}}(\lambda_{pu})$ and the pump pulse intensity I_{pu} contribute to the signal. For the probe step, it depends on the absorption coefficient in the excited state $\alpha_{\mathrm{ES}}(\lambda_{pr})$ and the probe pulse intensity I_{pr}. Since the assignment of "pump" and "probe" is unclear for dynamics at negative delays, they are replaced by λ_1=266 nm and λ_2=238–248 nm.

$$A^+ \propto \alpha_{\mathrm{GS}}(\lambda_1) \cdot I(\lambda_1) \cdot \alpha_{\mathrm{ES}}(\lambda_2) \cdot I(\lambda_2), \tag{5.3}$$

$$A^- \propto \alpha_{\mathrm{GS}}(\lambda_2) \cdot I(\lambda_2) \cdot \alpha_{\mathrm{ES}}(\lambda_1) \cdot I(\lambda_1). \tag{5.4}$$

The ratio of the signal amplitudes at positive and negative delays A^-/A^+ is then independent of the pulse intensities.

$$\frac{A^-}{A^+} = \frac{\alpha_{\mathrm{GS}}(\lambda_2) \cdot \alpha_{\mathrm{ES}}(\lambda_1)}{\alpha_{\mathrm{GS}}(\lambda_1) \cdot \alpha_{\mathrm{ES}}(\lambda_2)}. \tag{5.5}$$

The relative absorption of the ground state can be deduced from the absorption spectrum. Knowing the relation of A^-/A^+, we can draw conclusions on the relation of $\alpha_{\mathrm{ES}}(\lambda_2)/\alpha_{\mathrm{ES}}(\lambda_1)$. This gives an insight into the excited state ionisation cross-sections of the DNA bases in the UV region.

The lifetimes that are measured are influenced not only by the excited state lifetime itself but also by the Franck-Condon overlap with the ionic state. In general, the ionisation energy increases as the molecule leaves the ground state geometry which usually happens during excited state relaxation *via* a conical intersection. If the photon energy of the probe pulse is high enough, then the ionic state may be reached during the whole relaxation process. For very high photon energies (VUV or EUV photons), even the ground state can be ionised and the re-population of the ground state may be observed. In this work, UV pulses in the photon energy range of 4.6–5.2 eV are used. For these photon energies, it is not obvious that we can always ionise the excited state but we will surely not ionise the ground state in an one-photon process. Hence, we evaluate our data very critically with respect to the possibility that the measured lifetimes do not reflect the return to the ground state but rather reveal the movement out of the Franck-Condon window for ionisation.

In the next sections, I will discuss the data obtained from DNA bases in aqueous solution. Except stated differently, the concentration of the DNA base will be 10^{-3} mol/l.

Table 5.1. Expected and measured photoelectron kinetic energies of the one-colour two-photon photoelectron signal. The expected photoelectron band maximum $E_{\mathrm{kin}}^{\mathrm{expected}}$ is given by the difference between the total absorbed photon energy $2 \times \hbar\omega$ and the vertical ionisation energy (VIE) deduced by Seidel [80]. The measured photoelectron bands $E_{\mathrm{kin}}^{\mathrm{measured}}$ are always lower than the expected values. The maximum kinetic energy $E_{\mathrm{kin}}^{\mathrm{max}}$ were deduced from the logarithmic plots of the one-colour spectra providing a minimum value for the ionisation energy $\mathrm{IE}^{\mathrm{min}}$ which is quite close to the calculated adiabatic ionisation potential $\mathrm{AIP}^{\mathrm{calc}}$ of the solvated molecules. Numbers in parentheses give the uncertainty of the last digit.

molecule	$\hbar\omega$	VIE [80]	$E_{\mathrm{kin}}^{\mathrm{expected}}$	$E_{\mathrm{kin}}^{\mathrm{measured}}$	$E_{\mathrm{kin}}^{\mathrm{max}}$	$\mathrm{IE}^{\mathrm{min}}$	$\mathrm{AIP}^{\mathrm{calc}}$
	eV	eV	eV	eV	eV	eV	eV
adenosine	4.66	7.5(2)	1.8(2)	0.9(1)	2.6(1)	6.7(1)	6.60 [81]
	5.21	7.5(2)	2.9(2)	1.1(1)	3.6(1)	6.8(1)	6.60 [81]
guanosine	4.66	7.2(1)	2.1(1)	0.9(1)	2.9(1)	6.4(1)	6.32 [81]
	5.21	7.2(1)	3.2(1)	1.0(1)	3.9(1)	6.5(1)	6.32 [81]
thymidine	4.66	8.1(1)	1.2(1)	1.0(1)	2.6(1)	6.7(1)	6.66 [82]
	5.21	8.1(1)	2.3(1)	1.2(1)	3.5(1)	6.9(1)	6.66 [82]
cytidine	4.66	7.8(2)	1.5(2)	0.8(1)	2.4(1)	6.9(1)	6.64 [82]
	5.21	7.8(2)	2.6(2)	0.9(1)	3.0(1)	7.4(1)	6.64 [82]

5.2. One-colour two-photon photoelectron spectra

In general, the one-colour photoelectron spectra provide information on the ground state binding energies of the system of interest. Figure 5.7 shows the one-colour two-photon photoelectron spectra of the four nucleosides in aqueous solution. For all molecules, spectra obtained with two different wavelengths are shown: 266 nm (green line) and 238 nm (blue line). All spectra are plotted on a linear scale to identify the photoelectron band maximum ($E_{\mathrm{kin}}^{\mathrm{measured}}$, left) and on a logarithmic scale to deduce the maximum kinetic energy ($E_{\mathrm{kin}}^{\mathrm{max}}$, right). The values are summarised in Table 5.1. The spectra and values will be exemplified using the case of adenosine but the concept/explanation applies in the same way for the other molecules.

From EUV photoelectron spectroscopy, the vertical ionisation energy (VIE) of adenine has been deduced to 7.5 eV [80]. Due to inhomogeneous broadening occurring in solution, that signal has a full width at half maximum of about 1 eV. For a two-photon ionisation process with 266 nm (4.66 eV) and 238 nm (5.21 eV) pulses, we would therefore expect the photoelectron band maximum to be around 1.8 and 2.9 eV kinetic energy, respectively. However, the measured photoelectron band maximum is at 0.9 and 1.1 eV kinetic energy for two-photon ionisation with 4.66 and 5.21 eV pulses, respectively. This is significantly lower than the expected values. Additionally, one would expect the band maxima to be separated by the difference of the absorbed photon energy, *i.e.* 1.10 eV for a two-photon process. But they are separated by only 0.2 eV, which is even less than expected for a one-photon process. The logarithmic plot reveals that the spectrum obtained with 238 nm pulses extends to significantly higher kinetic energies than the spectrum obtained with

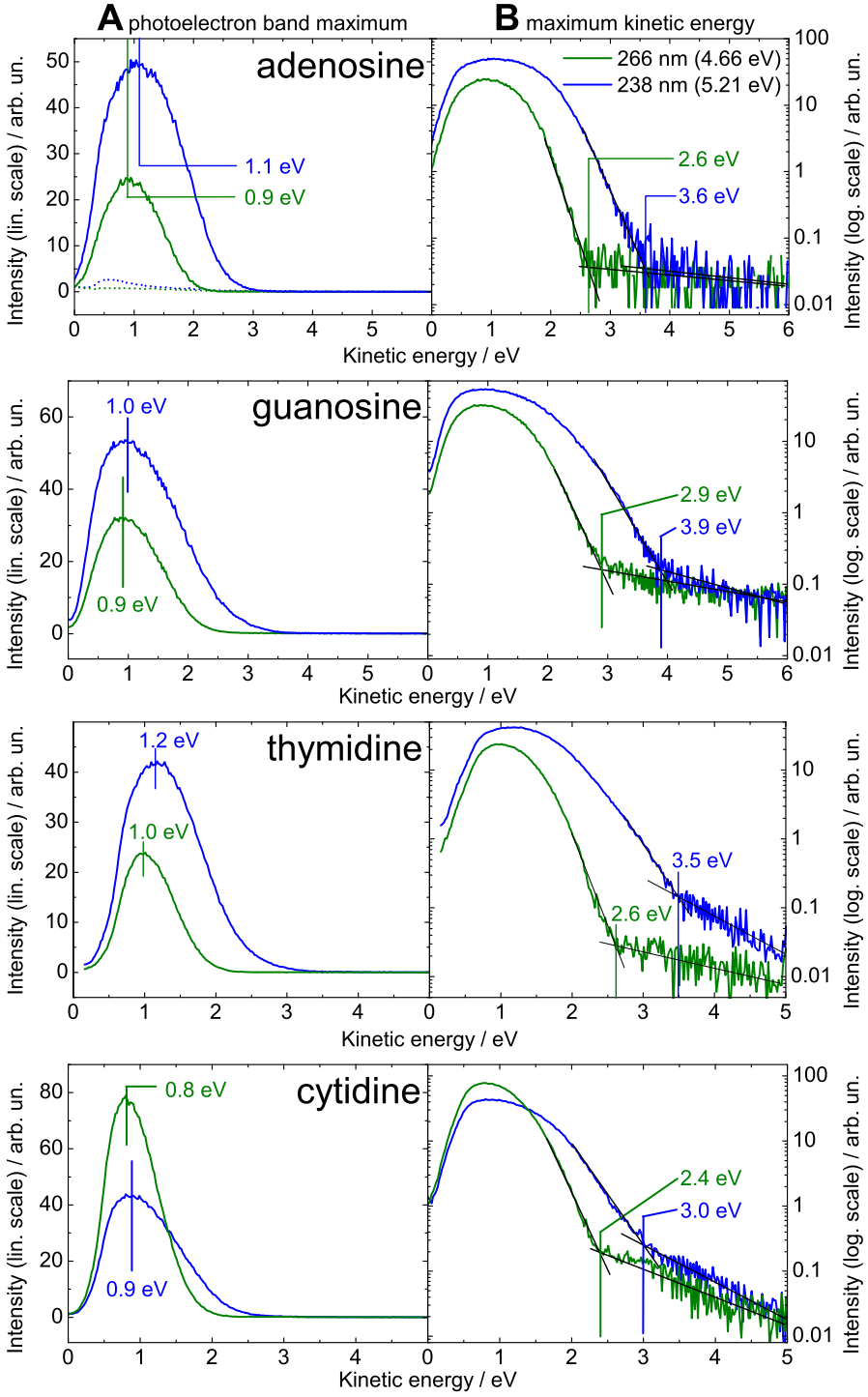

Figure 5.7. One-colour two-photon photoelectron spectra of the nucleosides in aqueous solution for 266 nm (green) and 238 nm (blue) pulses shown on a linear (A) and on a logarithmic (B) scale. top to bottom: adenosine, guanosine, thymidine, and cytidine. For each spectrum, the photoelectron band maximum (A) and the maximum kinetic energy (B) is identified. The dotted lines in the first plot show the one-colour spectra of the NaCl-buffer solution taken with 266 nm and 248 nm. Part of the figure is taken from Buchner *et al.* [79].

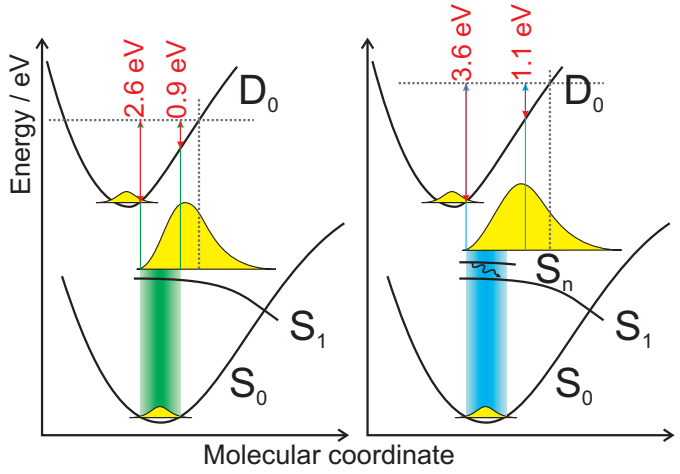

Figure 5.8. Illustration of the appearence of one-colour spectra exemplified on adenosine spectra using the corresponding potential energy curves (cf. Figure 5.12). Left: 266 nm (4.66 eV) pulses, right: 238 nm (5.21 eV) pulses. Initially, the molecule is in the ground state S_0. The coloured rectangle indicates the Franck-Condon (FC) region and absorption of a first photon populates the excited state S_1 (left) or S_n (right). Already within the pulse duration, the excited-state wave packet spreads, evolves away from the FC region, and nuclear relaxation sets in. This is indicated by the yellow shapes on the excited-state potential curve. In case of 5.21 eV excitation, the initialy populated state S_n relaxes into S_1 within 40 fs [83] which is indicated by a black arrow. Upon absorption of a second photon within the pulse duration, the excited-state wave packet is mapped onto the ionic state D_0. The values given above the ionic potential curve correspond to the maximum kinetic energy and the photoelectron band maximum determined from the measured spectrum (see top panel of Figure 5.7). The grey horizontal lines are photon energies ($2\ \hbar\omega$) and grey vertical lines indicate the end of the FC window for ionisation. Figure taken from Buchner *et al.* [79].

266 nm pulses. If we define the maximum kinetic energy as the intersection point between the high-energy tail of the spectrum and the noise level, then we find a maximum electron kinetic energy of 2.6 eV and 3.6 eV for the 266 nm and the 238 nm pulses, respectively. In contrast to the position of the band maxima, the difference between the maximum kinetic energies agrees well with the difference in absorbed photon energy.

These observations can be explained in terms of resonant two-photon ionisation with initial dynamics of the intermediate state occurring within the pulse duration of about 140 fs. This principle is sketched schematically in Figure 5.8. The molecule is initially in the ground state S_0. Absorption of a first photon populates the excited state S_1 or S_n, depending on the photon energy. For infinitely short pulses or negligible initial dynamics, absorption of the second photon would ionise the molecule from the Franck-Condon region. However, if the excited state evolves very quickly, nuclear rearrangement may already have started when the second photon of the same pulse is absorbed. Since the ionisation energy typically increases as the molecule leaves the ground state geometry, such initial dynamics results in lower photoelectron kinetic energies and photoelectron

bands which are significantly broader than supported by the Franck-Condon region. Therefore, the maximum of the photoelectron band $E_{\mathrm{kin}}^{\mathrm{measured}}$ cannot be related to the vertical ionisation energy (VIE) obtained with higher photon energies in a one-photon process. The ionisation energy derived from the photoelectron band maximum will be somewhat larger than the (true) value for the vertical ionisation energy. For higher excitation energies introducing more excess energy, the excited state can in general evolve faster as compared to lower excitation energy. Therefore, it is not surprising that for the 5.21 eV one-colour spectrum, a larger shift of the photoelectron band is observed than in the 4.66 eV spectrum. Additional broadening of the photoelectron band is initiated by the transition from S_n to S_1 within 40 fs [83].

From the maximum observed kinetic energy $E_{\mathrm{kin}}^{\mathrm{max}}$, a minimum value for the ionisation energy $\mathrm{IE}^{\mathrm{min}}$ of adenosine is deduced: (6.8 ± 0.1) eV and (6.7 ± 0.1) eV for 5.21 eV and 4.66 eV photon energy, respectively. These values are intriguingly close to the adiabatic transition energy of 6.60 eV calculated by Pluhařová *et al.* [81]. This suggests that the ionic ground state geometry is close to the Franck-Condon window for ionisation from the neutral ground state.

For guanosine, this finding of nuclear rearrangement starting within 140 fs is supported by the time-resolved fluorescence anisotropy measurements of Miannay *et al.* who found values below 0.2 for all times indicating a substantial geometrical change of the molecule faster than 100 fs [84].

For cytidine, the minimal ionisation energy $\mathrm{IE}^{\mathrm{min}}$ is larger than the calculated AIP. This observation can be interpreted in two ways (which may both be true). Firstly, the potential of the excited state has a large gradient in the FC region of the ground state accelerating the excited wave packet and increasing the ionisation potential of the excited state instantaneously. Secondly, the potential minimum of the ionic ground state geometry is not as close to the FC region of the ground state as in the other nucleosides.

5.3. Adenine and adenosine

5.3.1. Current state of knowledge

The adenine molecule can be present in the form of different tautomers which have different ground state energies. Figure 5.9 shows the six most stable tautomers of isolated adenine and the energy difference to the A1 tautomer [85]. In the gas phase, only one tautomer (A1 or 9*H*-Ade) is present since the other tautomers are substantially less stable. In aqueous solution, however, the situation is different. Due to interaction with the polar solvent, geometries with a large dipole moment are stabilised [81, 86]. Theoretical [86, 88–90] and experimental findings [91–94] lead to the conclusion, that

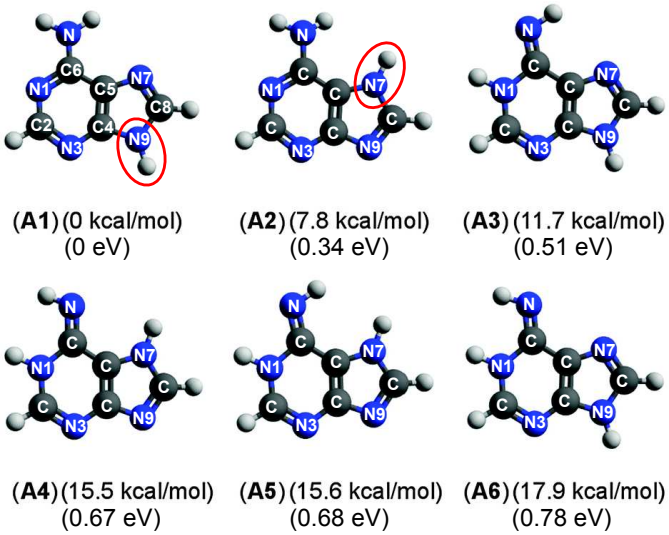

Figure 5.9. Tautomeric forms of isolated adenine and their ground state energies relative to the lowest energy tautomer [85]. In aqueous solution, the tautomer A2 is stabilised by interaction with the polar solvent and therefore also appears in significant amounts (about 20% [87]).

two tautomers co-exist in aqueous solution: the 7*H*-Ade (A2) and the 9*H*-Ade (A1). These two tautomers have similar ground state energies in water.

Excited state dynamics of adenine were previously investigated by transient absorption [87] and fluorescence up-conversion experiments [95, 96]. Cohen *et al.* performed transient absorption studies of adenine and methylated adenine derivatives to assign the lifetimes of different tautomers [87]. For adenine in solution, they measured a bi-exponential decay with lifetimes of (180±30) fs and (8.8±1.2) ps. Furthermore, they found lifetimes around 200 fs for adenine derivatives that are methylated at positions *N*1, *N*3, and *N*9, but about 4 ps in case of methylation at *N*7. Since the 1*H*- and 3*H*-tautomer of adenine are less stable, Cohen *et al.* assigned the 180 fs lifetime to the excited state relaxation of the 9*H*-tautomer and the 8.8 ps to the 7*H*-tautomer. Fluorescence up-conversion experiments of adenine and adenosine in solution performed in the group of Gustavsson [95, 96] also reveal similar excited state lifetimes. For adenine, they found a bi-exponential decay where the faster lifetime is between (340±70) fs and (670±140) fs depending on the pump wavelength and suggest that below 265 nm another decay channel plays a role involving the $\pi\sigma^*$ state which shortens the excited state lifetime. For adenosine, they found an excited state lifetime of about (310±50) fs which is independent from the excitation wavelength.

Ullrich *et al.* measured the time-dependent photoelectron spectra of isolated adenine [97]. They found a bi-exponenital decay of the $\pi\pi^*$ state with lifetimes of <50 fs and 750 fs. Kang *et al.* studied the time-resolved transient ion signal of isolated adenine and adenine derivatives [98]. They found excited state lifetimes of around 1 ps for all the

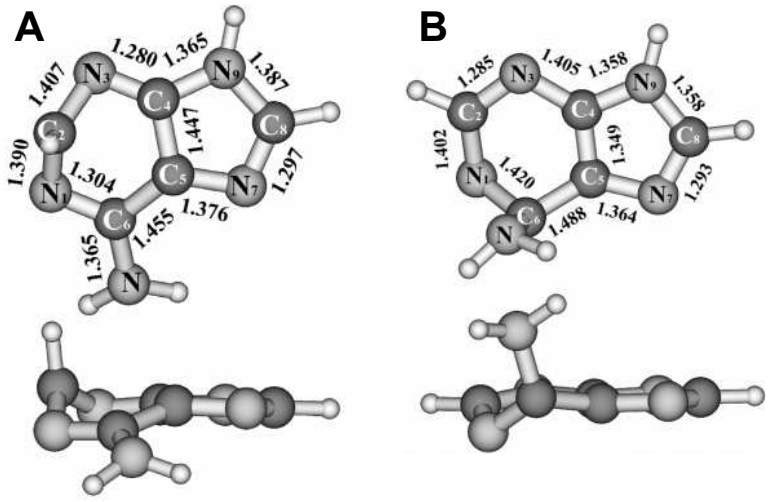

Figure 5.10. The most important conical intersections of isolated adenine calculated using CASSCF theory [102]. The CI assigned to a transition from the ππ* state to the ground state is connected with an envelope puckering at *C*2 (A). The CI of the nπ* state with the ground state is an out-of-plane distortion of the *C*6-atom and the amino group (B). Both structures are shown from the top and in side view. The bond lengths are given in angstroms. Figure taken from Ref. [102].

adenine derivatives which they studied.

Theoretical studies of isolated adenine (especially the 9*H*-tautomer) in the gas phase identified several conical intersections (CI) relevant for the excited state relaxation (ππ*/nπ*, ππ*/πσ*, nπ*/S_0, ππ*/S_0, πσ*/S_0) [83, 97, 99–107, and references therein]. Starting from the ground state geometry of adenine, where all ring-atoms lie in the same plane, these CIs are associated with geometrical changes of the molecule. The two most important CIs include an envelope puckering at the *C*2-atom (^{2}E, ππ*/S_0) and a pronounced out-of-plane distortion of the *C*6-atom and the amino group ($^6S_1$, nπ*/S_0). These two CIs are illustrated in Figure 5.10. Calculations reveal the existence of other CIs connected with a stretch of the *N*9–*H* bond (πσ*/S_0) and/or *C*8–*N*9 bond breaking (for labelling of atoms, see Figure 5.9). For excitation energies around 5.0 eV (the maximum of the absorption band in the gas phase), two mechanisms were found to explain the lifetimes observed in experiments with isolated adenine: A direct decay of the ππ* state to the ground state S_0 (*via* ^{2}E) and a transition from the ππ* state to the nπ* state are responsible for the ultrafast lifetime below 200 fs, whereas the subsequent decay of the nπ* state to the ground state S_0 (*via* $^6S_1$) explains the second, slightly longer lifetime below 1 ps. For excitation energies above 5.3 eV, another channel arises: the initially excited ππ* state decays to an πσ* state which finally relaxes to the ground state S_0. This channel is associated with an elongation of the *N*9–H bond [102, 108–110].

Theoretical studies of adenine in solution are rare because not only all the relevant electronic states have to be described as correctly as necessary and reasonable but also the effect of the surrounding solvent molecules has to be included. There have been different approaches to account for the effect of the environment on the relaxation of adenine [83, 111–114]. Mitrić *et al.* used the time-dependent density functional tight binding method combined with a surface hopping algorithm to calculate the non-adiabatic relaxation of microsolvated adenine [114]. After excitation with 260 nm light into S_3 ($\pi\pi^*$), they found a 16 fs transition into S_1 ($n\pi^*$) and a time constant of 200 fs for re-population of the ground state. Lan *et al.* recently studied the non-adiabatic dynamics of 9*H*-Ade in aqueous solution using surface-hopping quantum mechanical- molecular mechanical (QM/MM) simulations [83]. They found a relaxation mechanism that also appears for the gas phase (a two-step $\pi\pi^*\rightarrow n\pi^*\rightarrow S_0$ pathway via the $^6S_1$-CI). Due to a slight non-planarity of the molecule in solution (out-of-plane amino group), the molecule is oriented towards the $^6S_1$ conical intersection. Thus, this pathway is dynamically favoured and dominates the relaxation. This would also explain the faster relaxation in solution with respect to the gas phase, i.e. $<$350 fs in solution vs. $\sim$1 ps in the gas phase.

Lan *et al.* also calculated the vertical energies of the first three excited states of 9*H*-Ade in a water sphere of 20 Å diameter. For ten snapshot geometries obtained after ground state minimisation, they found the S_1 state ($n\pi^*$ character) between 4.45 and 4.69 eV. The S_2 and S_3 states (both $\pi\pi^*$ character) always lie very close (within 0.1 eV) in the range of 4.69–4.95 eV [83]. After excitation of the S_2 state, Lan *et al.* found an ultra-fast population transfer into the S_1 state within 40 fs and a lifetime of 410 fs for internal conversion from the S_1 state into the ground state.

For the second tautomer (7*H*-Ade), there has been significantly less theoretical activity. Marian et al. found some higher potential barriers for the relaxation into the ground state for the isolated 7*H*-Ade compared to 9*H*-Ade [115]. These barriers would explain the larger excited state lifetime assigned to 7*H*-Ade in solution.

In adenosine, the sugar moiety is attached to position *N*9 and blocks the hydrogen (or proton) migration which is necessary to form the second tautomer which is also present in solution. This is shown in Figure 5.11. For adenosine itself, there are no simulations of the excited state dynamics in solution, yet. Only recently, Tuna *et al.* explained the significantly faster relaxation of adenosine as compared to adenine in the gas phase [116–119]. They found that an intra-molecular hydrogen bond between the sugar moiety and the *N*3 atom of the adenine moiety led to a low-lying conical intersection with the ground state [116]. However, in water there are lots of other possibilities to form hydrogen bonds. Due to its structure, we can assume that adenosine behaves very similar to the 9*H*-Ade. Fluorescence up-conversion experiments on the excited state relaxation of adenosine show that it relaxes a bit slower than the contribution assigned to 9*H*-

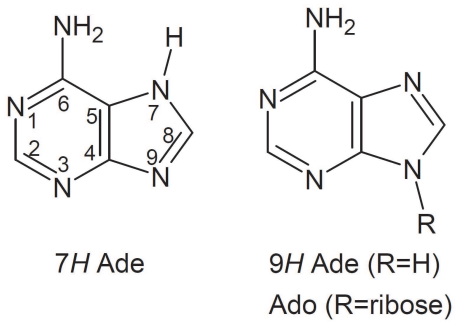

Figure 5.11. Chemical structure of the two relevant tautomers of adenine: the 7*H* Ade and the 9*H* Ade. In case of adenosine (Ado), a sugar moiety named ribose is covalently bound to the *N*9 position, and formation of the 7*H* tautomer is therefore excluded. Figure taken from Buchner *et al.* [79].

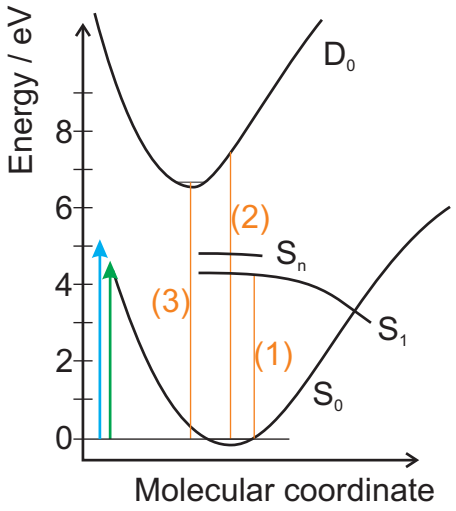

Figure 5.12. Schematic representation of the potential energy curves of the 9*H* tautomer of adenine in water, where S_0 is the ground state, S_1 is the excited state, and D_0 is the ionic ground state. Higher excited states are referred to as S_n. The green and blue arrows indicate the photon energies of pump and probe pulses applied in the present work (4.66 eV and 5.21 eV). The relative positions of the curves are given by (1) the UV/Vis absorption spectrum [120], (2) the vertical ionisation energy [80], and (3) the adiabatic ionisation potential [81]. The general shape of S_1 is adapted from Ref. [100]. Figure taken from Buchner *et al.* [79].

adenine [96]. It is speculated that due to the more efficient coupling to the bath *via* the sugar moiety, the excess energy is dissipated faster and the molecule needs more time to reach the conical intersection(s). First results on excited state dynamics of adenosine from a collaboration with R. Mitrić are discussed in Section 5.3.4.

Figure 5.12 shows a schematic of the potential energy curves for the 9*H* tautomer of adenine in water. To define the positions of the curves, experimental and theoretical values (orange) are used: (1) UV/Vis spectra show that the absorption of adenine in water starts at about 4.3 eV [120]. This is the lowest absorbable photon energy and therefore

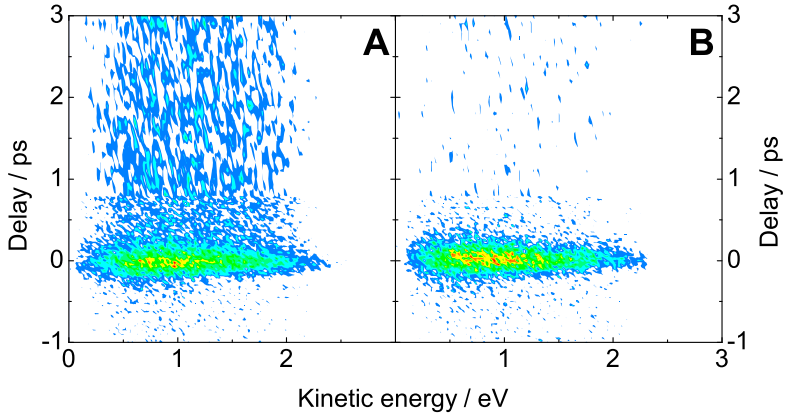

Figure 5.13. Time-resolved photoelectron spectrum of adenine (A) and adenosine (B) in aqueous solution. At positive delays, the molecules are excited with the 266 nm pulse and ionised with the 238 nm pulse (4.66 eV and 5.21 eV photon energy, respectively). At negative delays, pump and probe pulses are interchanged. The one-colour two-photon signals have been subtracted. Figure taken from Buchner *et al.* [79].

represents the 0-0 transition between the ground state S_0 and the first excited state S_1 ($\pi\pi^*$). (2) The vertical ionisation energy of adenine in aqueous solution was deduced experimentally to be 7.5 eV [80]. (3) The adiabatic ionisation potential of adenosine (corresponding to the 9*H* tautomer) in water has been calculated by *ab initio* methods together with the equilibrium polarisable continuum model to be about 6.6 eV [81]. The general shape of the excited state S_1 is adapted from Blancafort, who calculated the excited-state potential energy surface for different relaxation paths [100]: In the region of vertical excitation from the ground state, the excited state S_1 is quite flat and bends downwards near the conical intersection (there are several conical intersections with the ground state; we did not pick any specific one). According to Lan *et al.*, the higher excited states S_2 and S_3 lie very close together, directly above 4.7 eV [83]. We indicated those by S_n.

5.3.2. TRPES results - spectra

In Figure 5.13, the time-resolved photoelectron spectra of adenine (A) and adenosine (B) in aqueous solution are shown. These spectra show the time-dependent kinetic energy distribution of the photoelectrons, which directly depends on the population of the excited state(s). Around the temporal overlap of the pump and probe pulses, a strong and short-lived photoelectron signal appears for both molecules. This photoelectron distribution is quite broad and extends over a large range of more than 2 eV. In the case of adenine (see Figure 5.13A), a significant fraction of the signal persists towards positive delays (266 nm pump, 238 nm probe) for several picoseconds. As will be discussed later, this longer-lived signal stems from the 7*H*-tautomer that is only present in aqueous

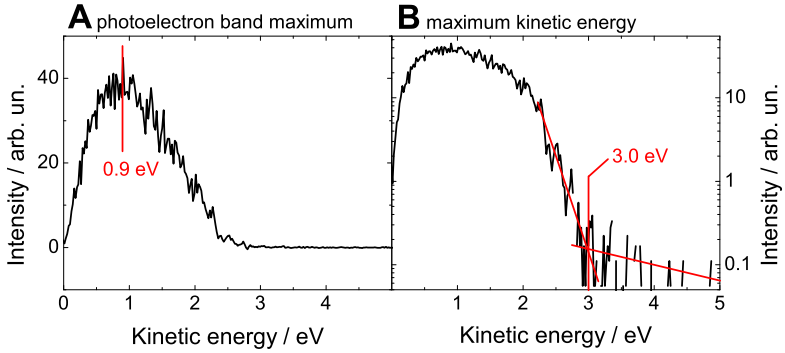

Figure 5.14. Photoelectron spectrum of adenosine in aqueous solution at the temporal overlap (± 0.1 ps) of both pulses (4.66 eV and 5.21 eV photon energy). The spectrum is shown on a linear scale (A) in order to identify the photoelectron band maximum of 0.9 eV and on a logarithmical scale (B) to deduce the maximum kinetic energy of 3.0 eV. The one-colour two-photon signals have been subtracted. Figure taken from Buchner *et al.* [79].

solutions of adenine, while the short-lived signal is assigned to the 9*H*-tautomer existing in aqueous solutions of adenosine as well [87].

In Figure 5.14, the pump-probe spectrum of adenosine in aqueous solution around the temporal overlap of both pulses is shown. This spectrum is averaged over the delay range (0.0 ± 0.1) ps. At these delays, ionisation due to absorption of one photon of each pulse is expected. According to the one-photon ionisation energy of adenosine [80], the photoelectron band should be centred around $(4.66 + 5.21 - 7.5)\,\text{eV} = 2.37\,\text{eV}$. In agreement with the findings for the one-colour two-photon ionisation discussed in the previous section, also the time-dependent photoelectron spectrum appears at lower kinetic energies than expected.

In Figure 5.15, the photoelectron distribution of the excited adenosine is shown for different delays. To compare the temporal change of the spectral shape, each spectrum is fitted with a function of the type $y = A \cdot x \cdot \exp(-Bx^2)$, and the fit results are scaled to 1 and shown in the insets. In the spectra shown in Figure 5.15A, the molecule is excited with 266 nm light (4.66 eV photon energy) and ionised with 238 nm light (5.21 eV). The spectra are shown for delays (0.0 ± 0.1) ps, (0.2 ± 0.1) ps, and (0.3 ± 0.1) ps. With increasing delay, the spectrum shifts slightly towards lower kinetic energies and becomes more narrow. The spectra shown in Figure 5.15B show the same qualitative behaviour for negative delays, i.e. for excitation with 238 nm and ionisation with 266 nm pulses. The spectral shift and the narrowing, however, are much more pronounced than for positive delays.

To get a more quantitative understanding of the spectral shift, it is described in terms

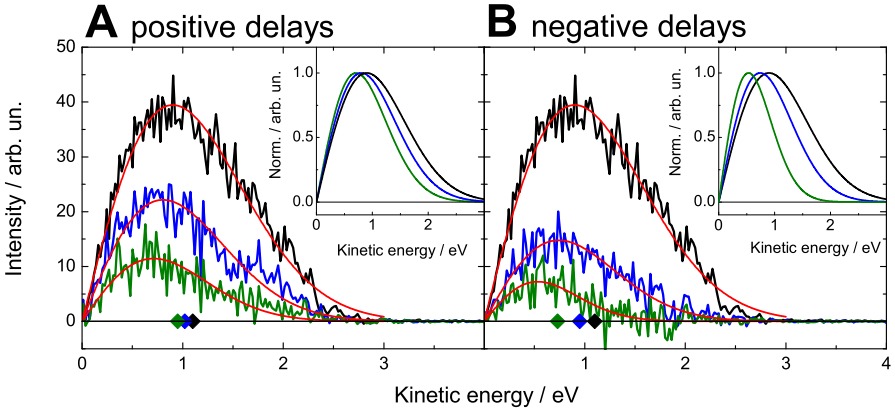

Figure 5.15. Time-resolved photoelectron spectra of adenosine in aqueous solution. A: excitation with 266 nm light and ionisation with 238 nm corresponding to positive delays, B: *vice versa*. For both excitation energies, spectra at delays 0.0 ps (black), 0.2 ps (blue), and 0.3 ps (green) are shown. All spectra are averaged over ± 0.1 ps to increase the signal-to-noise ratio. The diamonds mark the average kinetic energy of the corresponding spectrum. To compare the time-dependent shape of the spectrum, a function $y = A \cdot x \cdot \exp(-Bx^2)$ was fitted to the spectra. The insets show the corresponding fit results with their maximum scaled to 1 in the same colour code. Figure taken from Buchner *et al.* [79].

of an average kinetic energy (AKE) defined as an expectation value:

$$\mathrm{AKE} = \frac{\int_0^\infty E_{\mathrm{kin}} I(E_{\mathrm{kin}}) \mathrm{d}E_{\mathrm{kin}}}{\int_0^\infty I(E_{\mathrm{kin}}) \mathrm{d}E_{\mathrm{kin}}}, \tag{5.6}$$

where $I(E_{\mathrm{kin}})$ is the signal intensity at the kinetic energy E_{kin}. The AKE is illustrated by the diamonds in Figure 5.15A and B. After excitation with 4.66 eV photons, the AKE shifts only slightly changing from 1.10 eV at 0 ps to 1.02 eV at 0.2 ps, and to 0.95 eV at 0.3 ps. For excitation with 5.21 eV (negative delay direction with 238 nm pump and 266 nm probe pulses), the AKE changes faster, namely from 1.10 eV at 0 ps to 0.95 eV at 0.2 ps and to 0.73 eV at 0.3 ps.

In Figure 5.16, this behaviour is sketched schematically for the delays 0 ps and 0.3 ps in positive (left) and negative (right) temporal direction. The excited state is prepared by absorption of a pump photon (4.66 eV or 5.21 eV), and the FC region is indicated by a green/blue rectangle. At delay $\Delta t = 0$ ps, dynamics occurring within the pulse duration broadens the wave packet in the same way as explained for the one-colour signals which is indicated by the yellow shapes on the excited state potential curves. Immediate absorption of a probe photon leads to a maximum kinetic energy of 3.0 eV (see Figure 5.14) and an AKE of 1.10 eV. These numbers appear for both wavelength combinations because at $\Delta t = 0$ ps, the pump and probe pulses are interchangeable. Differences occur in the spectra at $\Delta t = 0.3$ ps. At this delay, the population has decreased due to internal conversion at a conical intersection with the ground state. The remaining population

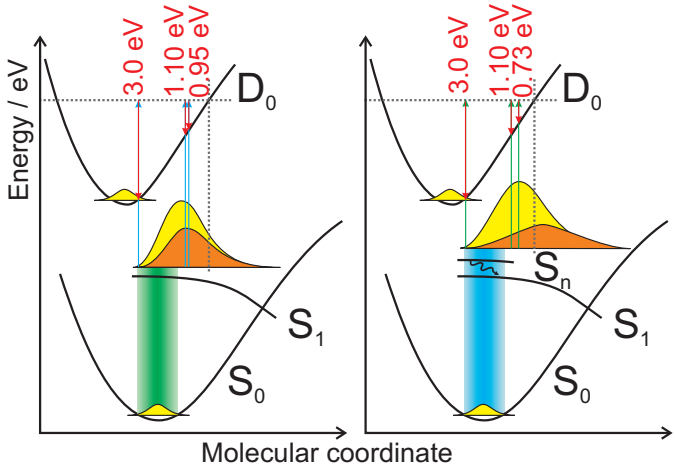

Figure 5.16. Illustration of the appearance of the time-dependent spectra using the potential energy curves previously shown in Figure 5.12. Initially, the molecule is in the electronic ground state S_0. Absorption of a pump photon in the Franck-Condon region is indicated by a green (4.66 eV) or blue (5.21 eV) rectangle. The wave packet in the excited state is broadened by dynamics occurring within the pulse duration at $\Delta t = 0$ ps (yellow shapes) and by further nuclear rearrangement at $\Delta t = 0.3$ ps (orange shapes). Upon absorption of a probe photon (blue and green arrows corresponding to 5.21 and 4.66 eV, respectively), the excited-state wave packet is mapped onto the potential curve of the ionic ground state D_0. The numbers above the arrows give the values for the maximum kinetic energy at $\Delta t = 0$ ps, the average kinetic energy (AKE) at $\Delta t = 0$ ps, and the AKE at $\Delta t = 0.3$ ps. The grey horizontal lines reflect the sum of the photon energies and grey vertical lines indicate the end of the Franck-Condon window for ionisation. Figure taken from Buchner *et al.* [79].

has moved towards the conical intersection. This is indicated by the orange shapes. The value of the AKE at $\Delta t = 0.3$ ps is smaller for excitation with higher photon energy due to the accelerated dynamics occurring when higher excess energy is introduced into the molecule.

5.3.3. TRPES results - population dynamics

To evaluate the population dynamics and excited state lifetimes of adenine and adenosine, the photoelectron signal is integrated over all kinetic energies and plotted *versus* the pump-probe delay. In Figure 5.17, the spectrally integrated photoelectron signals of adenosine are shown for three different probe-photon energies (248 nm (A), 243 nm (B), and 238 nm (C)). These traces are fitted by a sum of two contributions, namely a single component for each temporal direction. For further information on the fit function, see appendix A.1. The results of these fits are summarised in Table 5.2. The lifetimes extracted for each case are very similar: about 150 fs for the positive temporal direction and about 130 fs for the negative temporal direction.

For positive delays, the molecules are always excited with 266 nm pulses. The ex-

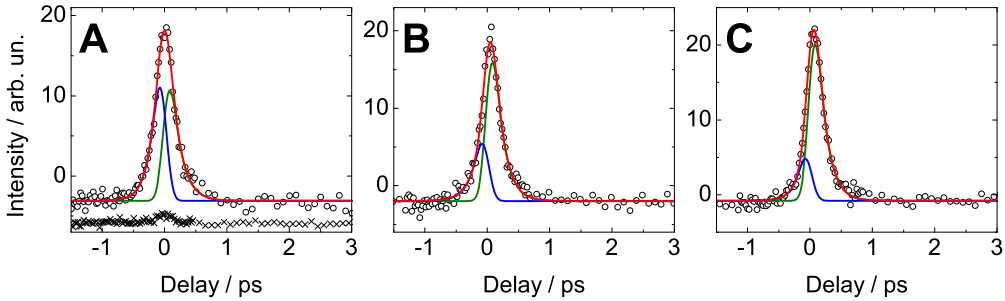

Figure 5.17. Energy-integrated photoelectron signal and fit of adenosine for different probe wavelengths: 248 nm (A), 243 nm (B), and 238 nm (C). The pump-wavelength is constant at 266 nm (4.66 eV). The open circles represent data points. The blue and green lines fit the population dynamics in the positive and negative delay direction; the red line is the cumulative fit. For comparison, also the signal of the buffered NaCl solution without adenosine is shown (crosses in (A)). This signal was measured at the same wavelength but at twice the pulse energy. For clarity, this signal is displaced vertically. Figure taken from Buchner *et al.* [79].

Table 5.2. Excited state lifetimes of adenosine. The intensity ratio between contributions to positive and negative delays $A_{\mathrm{rel}} = A^-/A^+$ relates to the relative ionisation cross-sections of the excited state.

	Photon energies / eV		Lifetime	
	pump	probe	τ / fs	A_{rel}
positive delays	4.66	5.00	150±10	
	4.66	5.10	150±10	
	4.66	5.21	150±10	
negative delays	5.00	4.66	130±10	1.1(1)
	5.10	4.66	150±20	0.41(5)
	5.21	4.66	120±20	0.30(4)

tracted lifetimes are identical without any dependence on the probe wavelength. We observe a lifetime of (150±10) fs. This is very close to the value of (170±10) fs that Onidas *et al.* observed using the fluorescence up-conversion method [121]. Somewhat larger values of (290±40) fs and (310±50) fs were obtained from transient absorption measurements by Pecourt *et al.* [122] and from fluorescence up-conversion experiments by Pancur *et al.* [96], respectively.

At negative delays, the dynamics are initiated by a photon energy that is varied between 5.0 and 5.2 eV and probed by 4.66 eV. With these pump photon energies, higher excited states are initially populated. These states decay within the pulse duration to the S_1 state resulting in higher excess energy as compared to excitation with a 4.66 eV pump photon energy. With increasing excess energy in the S_1 state the conical intersection with the S_0 ground state can be reached in a shorter time. Additionally, also higher-lying conical intersections may play an increasing role which also would lead to an accelerated relaxation. Thus, for the higher excitation energy, a smaller lifetime is expected. The

slight increase of the pump photon energy from 5.0 to 5.2 eV does not reveal a significant change in the observed excited state lifetimes. However, the mean lifetime of about 130 fs is slightly shorter compared to the lifetime observed for excitation with 4.66 eV photon energy which was discussed in the previous paragraph, i.e. 150 fs. A similar behaviour was reported by Pancur *et al.* who measured fluorescence up-conversion of adenosine using tunable pump pulses in the UV range [96]. They observed slightly longer fluorescence lifetimes for longer excitation wavelengths (>260 nm, lower pump photon energies) compared to excitation with shorter wavelength. Additionally, in this temporal direction, the probe pulse is only 4.66 eV. For a smaller probe photon energy, the measured excited state dynamics might be limited by the Franck-Condon window for ionisation. As the excited state evolves and nuclear rearrangement occurs, the potential energy of the ionic ground state typically increases. Thus, there is a minimum photon energy that is necessary to ionise the excited state all along the path to the conical intersection. Therefore, it cannot be excluded that the shorter lifetimes measured for the negative temporal direction is in part due to the smaller probe photon energy used in these experiments.

As stated in Table 5.2, the intensity ratio A_{rel} increases with increasing excitation wavelength λ_2, i.e. with decreasing photon energies between 5.2 and 5.0 eV. The relative absorption of the ground state ($\frac{\alpha_{\mathrm{GS}}(\lambda_2)}{\alpha_{\mathrm{GS}}(266\mathrm{nm})}$) can be retrieved from the absorption spectrum (see Figure 5.3). With increasing λ_2, the relative absorption of the ground state increases from 0.4 at 238 nm to 0.6 at 243 nm and reaches 0.8 at 248 nm. According to equation 5.5, the relative absorption of the excited state is then given by:

$$\frac{\alpha_{\mathrm{ES}}(\lambda_2)}{\alpha_{\mathrm{ES}}(266\mathrm{nm})} = \frac{\alpha_{\mathrm{GS}}(\lambda_2)}{\alpha_{\mathrm{GS}}(266\mathrm{nm}) \cdot A_{\mathrm{rel}}} \tag{5.7}$$

Hence with increasing λ_2 (between 238 and 248 nm), the relative absorption of the excited state ($\frac{\alpha_{\mathrm{ES}}(\lambda_2)}{\alpha_{\mathrm{ES}}(266\mathrm{nm})}$) yields values of 1.3 at 238 nm, 1.5 at 243 nm and 0.7 at 248 nm.

For adenine, the time-dependent signal is more complex due to the second tautomer co-existing in aqueous solution. The time-dependent signal for adenine is shown in Figure 5.18 for the same wavelength combinations as for adenosine. Due to the presence of the $7H$ and $9H$ tautomer, the signal was fitted with two contributions in positive direction. We assume global lifetimes τ_1^+ and τ_2^+ ("+" refers to positive delays) which are independent of the probe wavelength, because the dynamics is initiated by the same photon energy (4.66 eV) and the probe wavelength is changed only slightly. In negative temporal direction, the second contribution is not obvious from the data. Hence, only one contribution was chosen, possibly yielding a mean lifetime of both contributions (not common for the different pump wavelengths). The results of these fits are given in Table 5.3.

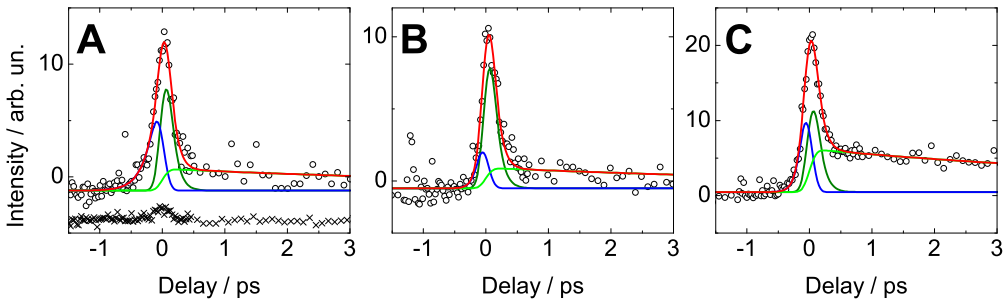

Figure 5.18. Energy-integrated photoelectron signal of adenine in aqueous solution and global fit for different probe wavelengths: 248 nm (A), 243 nm (B), and 238 nm (C). The crosses in (A) again reveal the signal of the blank buffered NaCl solution measured with the same wavelengths but at twice the pulse energy. For clarity, this signal is displaced vertically. Figure taken from Buchner *et al.* [79].

Table 5.3. Excited state lifetimes and intensity ratios of the contributions of adenine. (∗) For positive delays, the intensities of the fast and the slow component are compared by the intensity ratio given by $\alpha = A_2^+/A_1^+$. The intensity ratio given for the negative delays denotes the ratio between the total contributions to negative and positive delays ($\beta = A_1^-/(A_1^+ + A_2^+)$). †This lifetime was kept constant.

	Photon energies / eV		Lifetimes		Intensity ratio (∗)	
	pump	probe	τ_1 / fs	τ_2 / ps	α	β
positive delays	4.66	5.00	90±10	8±2	0.07(2)	
	4.66	5.10			0.06(2)	
	4.66	5.21			0.18(3)	
negative delays	5.00	4.66	180±30			0.4(2)
	5.10	4.66	70±30			0.4(3)
	5.21	4.66	75±10			0.8(2)

Upon excitation with 4.66 eV pulses, a short lifetime in the range of $\tau_1^+ = 100$ fs is observed which is slightly shorter than the excited state lifetime of adenosine (150 fs) and therefore is assigned to the $9H$ tautomer. But compared to adenosine a second contribution with a lifetime of a few ps appears. This second contribution is due to the $7H$ tautomer as has been shown by Cohen *et al.* [87]. The extracted lifetime for this tautomer is $\tau_2^+ = 8 \pm 2$ ps, which is in agreement with the lifetimes measured in transient absorption and fluorescence up-conversion experiments, i.e. (8.8 ± 1.2) ps [87] and (8.4 ± 0.8) ps [96], respectively. Therefore, we can assume that the Franck-Condon window for ionisation is accessible during the whole relaxation dynamics of the excited state.

However, the relative amplitude of the two contributions at positive delays ($\alpha = A_2^+/A_1^+$) depends on the probe wavelength: for 5.2 eV, α is about three fold higher than for 5.0 and 5.1 eV. Since the two contributions were assigned to the $7H$ and $9H$ tautomer and the relative abundance of these tautomers obviously does not change with

the probe wavelength, this change in α has to be assigned to a wavelength-dependent ionisation cross-section. This indicates that the cross-section for ionisation of the excited $7H$ tautomer drops drastically when decreasing the probe photon energy below 5.2 eV.

For the negative temporal direction (excitation with 5.0–5.2 eV photons), the second contribution assigned to the $7H$ tautomer should in principle appear, too. But the data show no hint for the existence of this component for negative delays. Instead, we observe a short lifetime below 200 fs which might be assigned to the $9H$ tautomer. The lack of signal lasting for longer than a ps can be interpreted in three ways: higher excitation energy, insufficient probe photon energy, and low ionisation cross-sections. Firstly, the higher excitation energy may accelerate the dynamics to such an extent, that the lifetimes of $9H$ and $7H$ tautomer become similar and cannot be discriminated. Marian *et al.* proposed a barrier along the excited state relaxation pathway of the $7H$ tautomer [115] explaining its longer lifetime. Due to the high excitation energy at negative delays, the excited state relaxation of the $7H$ tautomer might easily overcome this barrier or different relaxation pathways become accessible. Secondly, the probe wavelength (4.66 eV) may not suffice to ionise the excited state. This explanation can be easily ruled out by looking at the excited-state spectra: with 5.2 eV probe photon energy, the spectrum of the $7H$ tautomer extends to about 2 eV (see Figure 5.13A). With a probe photon energy of 4.66 eV, a spectrum extending to about 1.5 eV would be expected. Thirdly, the ionisation cross-section is very low for this probe wavelength. Given that we only observe small signals for ionisation with 5.0 eV as compared to 5.2 eV, a further decrease of the cross-section with decreasing probe photon energy seems reasonable.

Higher photon energies for ionisation may help to evaluate the real lifetimes related to the residence in the excited state and rule out Franck-Condon effects. Therefore, we have also performed measurements using 200 nm (6.2 eV) and 266 nm (4.66 eV) pulses. However, at this wavelength combination, a new process complicates the observed dynamics. Figure 5.19 shows the corresponding time-resolved photoelectron spectra of adenosine and adenine in solution. With these wavelengths, a transient signal is exclusively observed for excitation at 200 nm. Additionally, this signal is extremely long-lived with about 5–10% of the population persisting for more than 100 ps. Such a long-lived signal is not expected for DNA bases and suggests the presence of solvated electrons.

In Figure 5.20, the spectrum of the solvated electrons generated by photoexcitation of adenine (black triangles) is compared to the spectrum of the solvated electron generated by photodetachment of iodide ions (grey circles). The binding energy of solvated electrons close to adenine is 3.8 eV which is obviously somewhat higher than observed after iodide photodetachment (3.4 eV). Additionally, the spectral shape is quite different: it may either include more than just a single contribution or it may also be due to a different broadening mechanism (e.g. homogeneous broadening would lead to Lorentzian

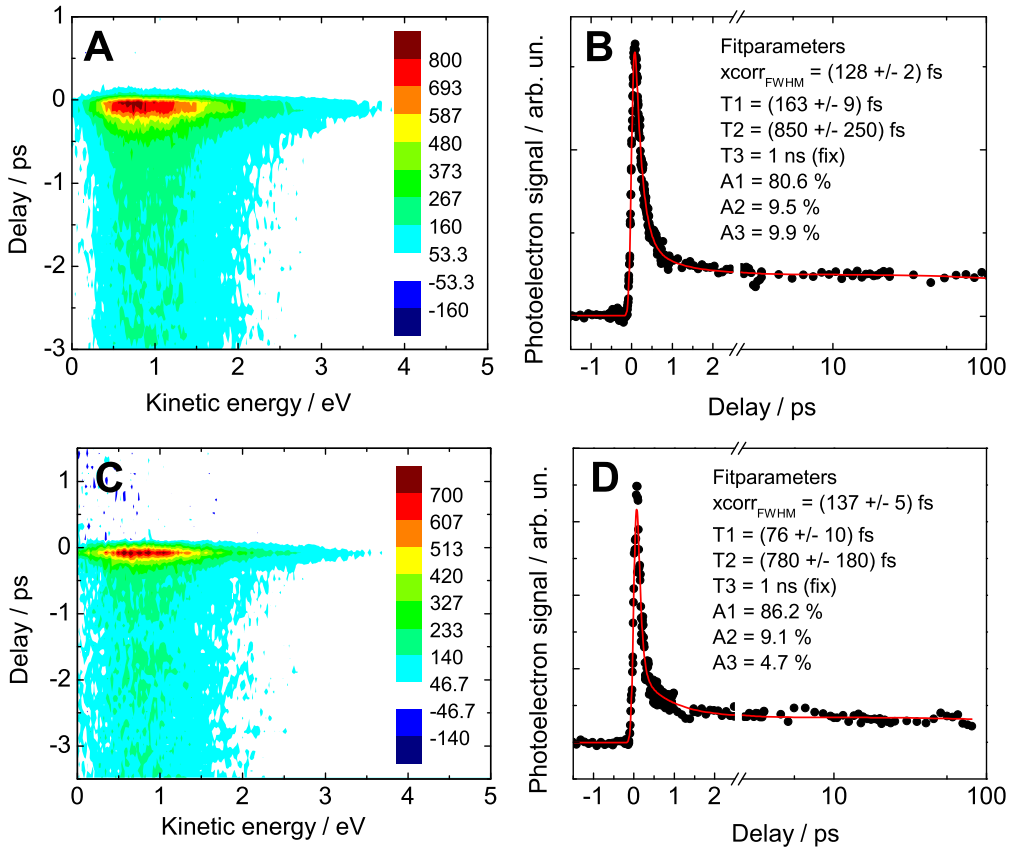

Figure 5.19. Time-resolved photoelectron spectrum of adenosine (A, B) and adenine (C, D) in solution measured with 200 and 266 nm pulses. Dynamics are initiated by the 200 nm pulse (10–30 nJ) and probed with 266 nm ($\sim$1.4 µJ). In B and D, the time axis is inverted in order to cover the whole delay range.

line shapes).

A channel for formation of solvated electrons from DNA bases has been proposed by Sobolewski and Domcke [99, 102, 123]. They studied the excited state dynamics of 9*H*-adenine applying different theoretical methods and found an additional relaxation channel *via* a repulsive $\pi\sigma^*$ state which is associated to elongation of the N–H bond. The existence of this channel was proven by the detection of fast hydrogen atoms after excitation of 9*H* adenine in the gas phase [107, 124]. In aqueous solution, hydrogen atoms undergo spontaneous charge separation forming a hydronium cation (H_3O^+) and a solvated electron [125, 126]. This could be the process leading to the solvated electrons observed upon excitation of adenine with 200 nm photons (see Figs. 5.19 and 5.20).

In order to observe the relaxation dynamics of the DNA bases, a signal induced by the probe pulse should be minimised. For DNA bases, this is the case at wavelength above 300 nm where the ground state does not absorb. However, these wavelength provide only a small Franck-Condon window for ionisation – if the excited state of the molecule can

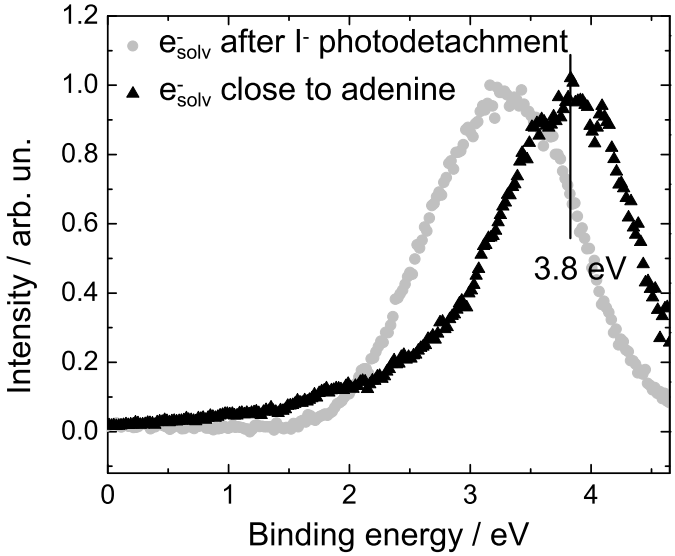

Figure 5.20. Comparison of the spectrum obtained from adenine solution with the spectrum of the solvated electron at large delays (see Fig. 4.4). In both cases, 200 nm pulses initiate the dynamics and 266 nm pulses probe it. The adenine spectrum (black triangles) is averaged over all delays >2 ps. The binding energy is somewhat higher for solvated electrons generated from adenine and also the line shape seems different.

be ionised at all with these low photon energies (∼4 eV). As a compromise between high photon energies for a large FC window and low ground state absorption to reduce probe-induced signal at negative delays, the subsequent measurements were conducted using probe pulses in the range of 240 nm (∼5.2 eV) where most DNA bases have a minimum in the absorption spectrum.

5.3.4. Comparison with theory

Motivated by these results, a collaboration with Roland Mitrić and co-workers was initiated. They combine the field induced surface-hopping (FISH) method [127] with a quantum mechanics/molecular mechanics (QM/MM) approach [128] to simulate excited state dynamics of molecules in the center of a large water droplet. The QM part is a semi-empirical method (OM2) including the adenosine molecule and three explicit water molecules while the MM part is a classical force field approach. Their specific method takes into account all single and double excitations out of the four most relevant configurations of the considered electronic states.

In Figure 5.21A, a snapshot of adenosine embedded in a water sphere of ∼ 26 Å radius is shown. Ground state QM/MM dynamics performed at 300 K give the thermal ensemble and hence provides the starting point for calculating the absorption spectrum and the non-adiabatic dynamics. The absorption spectrum obtained from a thermal ensemble of

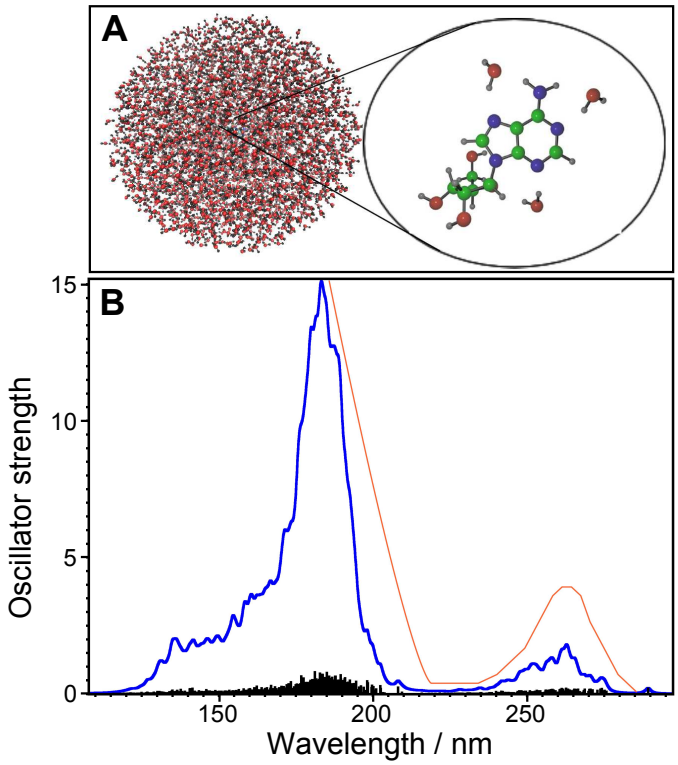

Figure 5.21. Adenosine is embedded in a water sphere of ∼26 Å radius (A). The calculated absorption spectrum (B, blue line) of this system includes the lowest 25 excited states calculated at the OM2 level for the thermal ensemble of 70 structures at 300 K. Individual transitions are given by the black sticks. The red line represents the experimental spectrum obtained by Arce *et al.* [129].

70 structures including the lowest 25 excited states is shown in Figure 5.21B. The peak position at about 260 nm and its width corresponds to the experimental spectrum. This agreement suggests that the chosen model may be also suitable to get proper information on dynamical simulations.

In the calculations, Mitrić and co-workers have simulated laser-induced non-adiabatic dynamics by applying a Gaussian pump pulse with similar parameters as used for our experiments at MBI: 4.66 eV photon energy, 3.5×10^{12} W/cm^2 intensity, and 33 fs temporal width (FWHM, Fourier-transform limited). They have applied this pulse to 50 initial conditions obtained from the ground state QM/MM dynamics and propagated these for 1 ps. Figure 5.22 shows the result of one typical trajectory and the corresponding geometry at three selected delays. At t=0 ps, the molecule is in the ground state (0 eV relative energy) with excited state energies around 5 eV and the ionic ground state above 8 eV. Due to structure fluctuations, also the energy gap between ground and excited states fluctuates and the molecule can be excited when the energy gap is around 4.66 eV. The pump pulse (centred at t=40 fs) initially populates the bright state

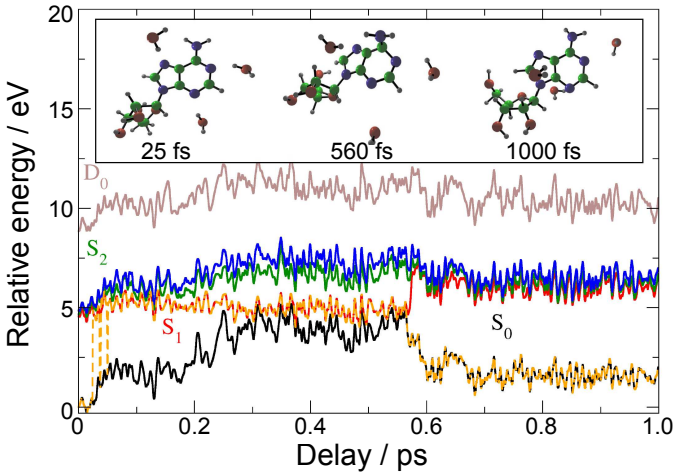

Figure 5.22. Relative energies of the lowest four electronic states (S_0–S_3) and the ionic ground state (D_0) of adenosine in water calculated from a single trajectory. At t=0 ps, the molecule is in the ground state (black). In the Franck-Condon region, the first three excited states lie in close proximity just below 5 eV (red, green and blue line). At t=40 fs, the molecule is excited by a 4.66 eV Gaussian laser pulse (33 fs pulse duration, 3.5×10^{12} W/cm^2 intensity). The dashed orange line marks the actual state that the trajectory resides in. At t$\sim$560 fs, this trajectory reaches a conical intersection and returns to the ground state. The inset shows geometries of the molecule at different delays: at 25 fs the molecule ist still in S_0 (planar aromatic ring), at 560 fs, the conical intersection is reached (puckering of the aromatic ring), and at 1 ps the molecule is back in S_0 (planar again).

S_2. The geometry of the just excited molecule (at 25 fs) still resembles the ground state geometry with a planar aromatic ring. Within a few fs, the population relaxes from S_2 to S_1 and the geometry starts to change. This is revealed by an increase of the relative energy of both the neutral and the ionic ground state. As dynamics in the excited state proceeds, the puckering ring mode on *C*6 (carrying the amino group) is populated and charge density accumulates on this site. For this specific trajectory, the geometry of the conical intersection of S_1/S_0 is reached at about 560 fs and the population is transferred to the ground state. The corresponding snapshot shows a slightly distorted 5-membered ring and a displaced amino group. Afterwards, the molecule returns back to the original geometry as the structure at 1 ps reveals a planar adenine moiety. Cooling of the hot ground state is not fully completed within the propagation time of 1 ps.

In Figure 5.23, the results of 50 trajectories propagated over 1 ps are shown. Again, the exciting Gaussian pulse is centred at 40 fs. Therefore, the population of S_0 (*i.e.* the ground state) is maximum at t=0 ps. The incoming laser pulse couples the ground state with the excited states and populates these. But the populations of S_2 and S_3 relax extremely fast to S_1. In total, about 70 % of the 50 trajectories reach the excited state S_1, while about 30 % stay in the ground state. About 60 % of the excited trajectories decay to the ground state through a conical intersection associated with a puckering

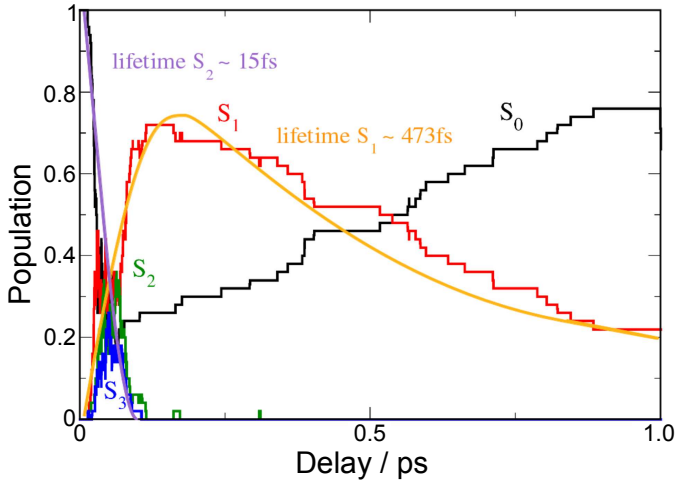

Figure 5.23. Excited state population of the three lowest excited states averaged over 50 trajectories. The initially populated state S_2 relaxes with a lifetime of about 15 fs to S_1 (violet line). The latter decays with a lifetime of about 470 fs into the ground state (orange line).

mode centred on a carbon atom in the adenine moiety ($C2$ or $C6$). The remaining 40 % do not reach a conical intersection with the ground state within the propagation time of 1 ps. An exponential fit to the S_2 population reveals a lifetime of only $\sim$15 fs. Already about 50 fs after excitation (at $\sim$100 fs), the population of S_1 reaches its maximum of about 70 %. Then the S_1 decays radiationless to the ground state with a lifetime of about 470 fs, which is on the same order of magnitude as the measured excited-state lifetime of adenosine in solution, *i.e.* 170 fs. This is a good agreement since there is a large number of uncertainties in the theory and experiment, i.e. the exact lifetime strongly depends on the excess energy and the details of the potential energy surfaces.

Figure 5.24 shows the corresponding time-dependent binding energy calculated from the energy gap between the current state (S_{0-3}) and the ionic ground state (D_0). Again, the exciting pulse is centred at 40 fs. Therefore, at t=0 fs, all trajectories reside in S_0 (*i.e.* the ground state) and a large signal is observed at binding energies >8 eV. Upon interaction with the pulse, 70 % of the trajectories change to the excited states S_{1-3} and a large contribution at $\sim$4 eV binding energy appears. Due to the $\sim$15 fs transition from the S_2 state (and S_3) to the S_1 state, the spectrum shifts by about 1 eV to higher binding energies and broadens. This spectral component stays at about 5 eV, broadens further and finally decays leading to an increase (and also slight shift) of the signal around 8 eV. The re-population of the ground state leaves the molecule in vibrationally excited states which do not relax completely within the propagation time of 1 ps. Therefore, the energy of the ground state also shows some time-dependence appearing slightly shifted to lower binding energies.

From the data described above, Mitrić and co-workers calculated the difference be-

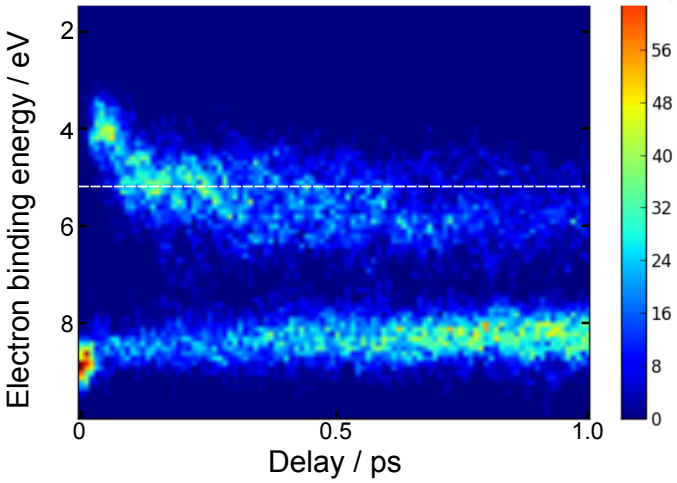

Figure 5.24. Simulated time-resolved electron binding energies of excited solvated adenosine averaged over the same 50 trajectories. Electron binding energies are obtained from the difference between the actual state S_n and the ionic ground state D_0. The dashed white line marks 5.2 eV binding energy, the highest energy accessible by the probe photons used in the experiments described in this thesis.

tween the probe photon energy (i.e. 5.21 eV) and the electron binding energy shown in Figure 5.24 in order to compare their results to the measured photoelectron spectra. Figure 5.25 shows a direct comparison of these calculated spectra (A) with the measured ones (B, discussed in detail in Section 5.3.2). For these simulated photoelectron spectra, again a Fourier-transform-limited pulse of 33 fs duration is included. However, in the experiment, a cross-correlation of about 200 fs (FWHM) was determined. Hence, the time-dependent shift of the simulated spectrum should be smeared out due to the actual probe pulse duration of ∼140 fs. Taking this into account, we find a good agreement between the simulated spectra and the experimental spectrum. However, after 200 fs, the S_1 contribution below 0.5 eV is absent in the measured spectra but still prominent in the simulated spectra. This reflects the different retrieved lifetimes that have been discussed in the paragraph before last. Another value that has not been treated in the theoretical description is the ionisation cross-section of the excited state. This can change time-dependently and therefore may lead to discrepancies between experiment and simulations. A third source for the observed discrepancy is the calculated energy of the excited S_1 and the ionic D_0 state.

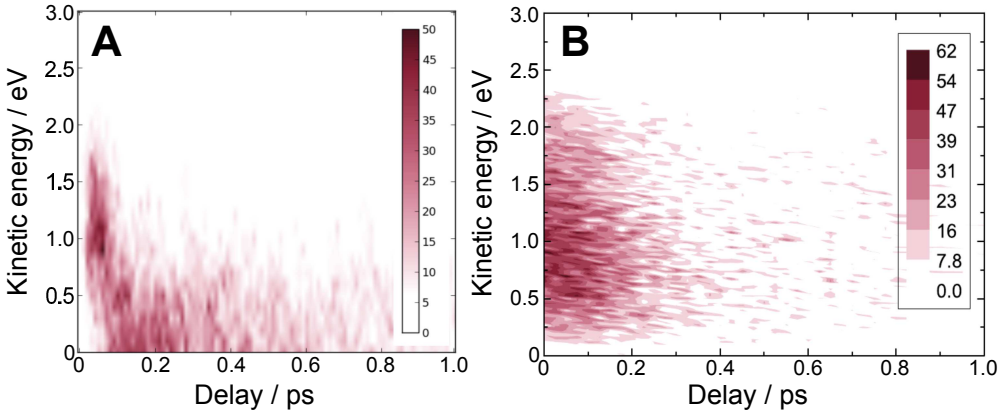

Figure 5.25. Time-resolved photoelectron spectrum of adenosine in a large cluster (A, simulated) and in aqueous solution (B, experiment).

5.4. Guanine and guanosine

5.4.1. Current state of knowledge

Besides adenine, guanine is the second purine base. For isolated guanine, theoretical studies identified several tautomeric structures with almost equal energy suggesting a broad variety of tautomers in gas phase experiments. Figure 5.26 shows the lowest tautomers of guanine found by a recent stuy [85]. For guanine in water, an enormous stabilisation of tautomers that have large dipole moments and that are rare in the gas phase has been predicted by calculations [130]. But comparison of IR and NMR spectra of different guanine derivatives have shown that at neutral pH values only the keto-amino tautomers of guanine (G1 and G2) are present in solution [131]. Since guanine is only very weakly soluble in water, we only studied its nucleoside guanosine with the sugar moiety attached to the $N9$ atom. Therefore, the $9H$-keto-amino tautomer (G2) will be considered for the interpretation of the data presented in this work.

For the relaxation of the excited $9H$-keto-amino guanine, different pathways have been identified in theoretical studies over the last decade. The excited $\pi\pi^*$ state can directly relax to the ground state via a conical intersection which is characterised by an out-of-plane (oop) movement of the $C2$ atom and a displacement of the NH_2 group [132–137]. This CI is called the *oop-NH_2* CI and is shown in Figure 5.27. Two only slightly different CIs with the same characteristics were found by Yamazaki et al. [136] (*ethylenic I* and *ethylenic II*) and further studied by Barbatti *et al.* [137]. The second pathway runs via an $n\pi^*$ state leading to a CI which is characterised by a puckering of the $C6$ atom and an oop motion of the carbonyl oxygen [132, 134, 135, 137]. A third pathway includes the $\pi\sigma^*$ state which has a conical intersection with the ground state at stretched NH bond lengths [136]. This relaxation path is only accessible about 0.4 eV

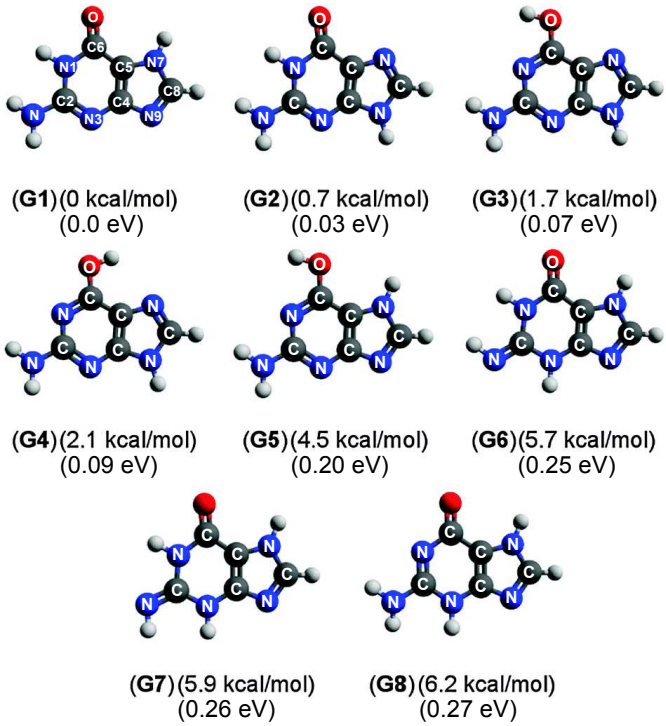

Figure 5.26. Tautomeric structures and relative energies of isolated guanine [85]. Shown are the structures with lowest energies. In pH neutral solution, only the keto-amino tautomers (G1 and G2) are present [131].

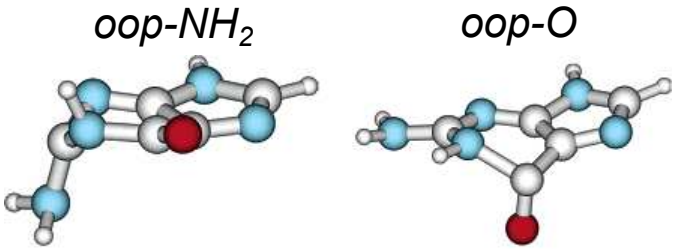

Figure 5.27. Geometries of two conical intersections of excited states with the ground state occurring in isolated guanine [132]. The *oop-NH_2* CI characterises a barrierless pathway from the ππ* state to the ground state. The *oop-O* CI is accessible after population transfer to the nπ* state.

above the absorption maximum of the first ππ* state in isolated guanine and therefore is not expected to play a role in the experiments. According to Barbatti *et al.*, only 5% of the population which initially starts in the ππ* state relaxes *via* the nπ* state [137]. The majority (95%) decays barrierless directly towards one of the *ethylenic* CIs. A recent molecular dynamics simulation of solvated guanine concluded that the *oop-O* CI is much more important in solution than in the gas phase [138]. About 42% (71%) of the trajectories started on the S_1 (S_2) state relax towards this CI.

In fs-transient absorption experiments, Kohler *et al.* found an excited state lifetime

of (460±40) fs for guanosine in aqueous solution [122, 139]. Peon and Zewail applied the fs-fluorescence up-conversion method to guanosine and GMP in aqueous solution. They found lifetimes of (690±100) fs and (860±100) fs for guanosine and GMP, respectively [140].

In a more recent study, Karunakaran *et al.* applied the transient absorption method to guanosine monophosphate (GMP) in aqueous solution probing the excited state with a broad band pulse of 270–900 nm [141]. They varied the excitation wavelength from the absorption maximum (267 nm, exciting L_a and L_b) to the low energy onset (287 nm, exciting only L_a) in order to observe spectral differences in the excited state. The absence of spectral differences indicates that the transition from the L_b to L_a must be faster than 100 fs and the whole dynamics observed in both cases reveals the relaxation along the L_a potential. Besides this ultrafast transition, they observe decay times of about $\tau_1 = 220$ fs and $\tau_2 = 900$ fs for in the wavelength region between 400 and 900 nm. In the wavelength region between 270 and 400 nm, the signal rises with $\tau_1 = 250$ fs and then decays bi-exponentially with $\tau_2 = 1$ ps and $\tau_3 = 2.5$ ps. Karunakaran *et al.* assign the observed lifetimes with the help of quantum-chemical calculations as follows: τ_1 (∼250 fs) denotes the transition from the FC region to a (preudo-)minimum on the L_a potential, τ_2 (∼1 ps) reveals the internal conversion from the L_a to the hot ground state which cools down with τ_3 (2.5 ps).

Shortly after these findings, Miannay *et al.* published their results on GMP contradicting this assignment [84]. They measured the fluorescence up-conversion signal of GMP in solution wavelength-resolved. They emphasise that all the observed signal must stem from a very flat excited state potential. They observe a quite complex behaviour of the time-dependent fluorescence up-conversion signal at different probe-wavelength. A global fit to their data reveals lifetimes of 0.16, 0.67 and 2.0 ps. Although the obtained lifetimes are comparable to the lifetimes obtained by Karunakaran *et al.*, their assignment must be revisited. The 2 ps lifetime cannot be assigned to hot-ground-state cooling because this would not show up in fluorescence. Hence, also the long lifetimes must be assigned to excited state relaxation. In Figure 5.28, these different assignments are visualised schematically. Applying time-resolved photoelectron spectroscopy, we contribute with a complementary method and improve this assignment.

5.4.2. TRPES results

Figure 5.29 shows the time-resolved photoelectron spectra of guanosine solution obtained by 266 nm pump and a tunable probe ranging from 238 nm to 248 nm. At negative delays, the signal stems from tunable pump and 266 nm probe pulses. In all three cases, a very broad photoelectron distribution at time zero is observed ranging up to about 2.5 eV

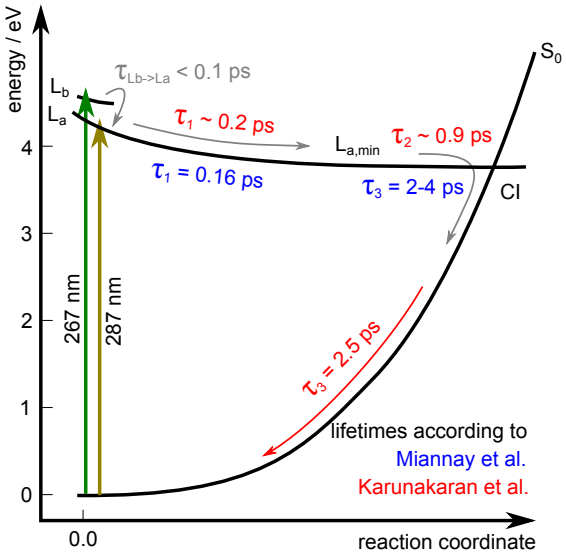

Figure 5.28. Schematic representation of the potential energy curves for guanosine and assignment of observed lifetimes as proposed by Karunakaran *et al.* [141] (red) and Miannay *et al.* [84] (blue), grey accounts for both. The ground state S_0 is excited vertically by the pump pulse (267 nm or 287 nm) to the bright excited states L_a and L_b. Both groups agree on the sub-100 fs $L_b \rightarrow L_a$ population transfer and the ~200 fs lifetime to leave the FC region. While Karunakaran propose a pseudominimum on the L_a potential and a ~1 ps population transfer to the hot ground state which cools down with a lifetime of about 2.5 ps, Miannay assign all their observed signal (up to 4 ps at 600 nm probe) to the excited state relaxation.

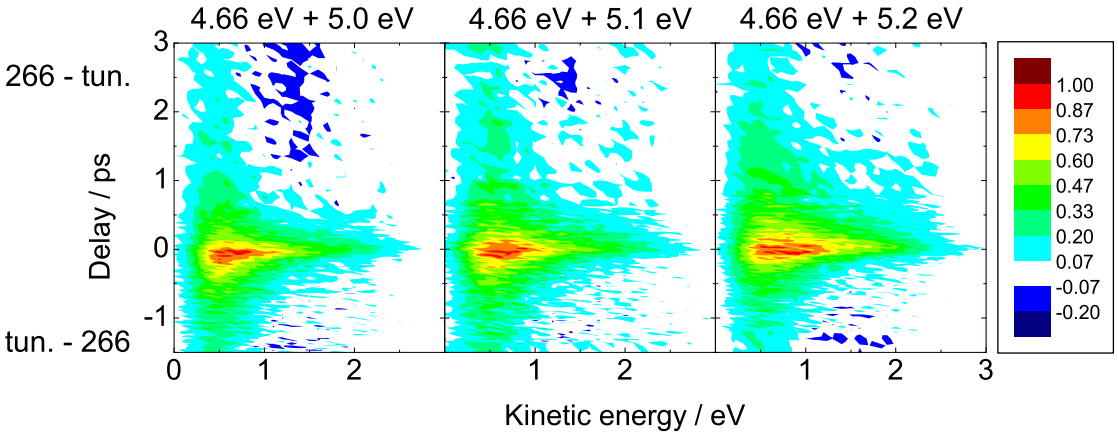

Figure 5.29. Time-resolved photoelectron spectra of a buffered 1 mM guanosine solution. For each wavelength combination, the raw data is shown as colour plot.

photoelectron kinetic energy. With increasing delays, the signal seems to shift towards lower kinetic energy and gets more narrow. The time-dependent spectral shape of the signal seems to be quite complex. Already from the raw data, it is obvious that a single contribution with a single lifetime would not fit the data satisfactorily. Therefore, the

Table 5.4. Lifetimes and relative intensity (A_{rel}= A_{slow}/A_{fast}) of the corresponding contributions of guanosine obtained for different pump and probe photon energies. (Parentheses show the uncertainty of the last digit as obtained from the fit.) †This lifetime was kept constant.

	pump / eV	probe / eV	τ_{fast} / fs	τ_{slow} / ps	A_{rel}
positive delays	4.66	5.00	380±10	2.4±0.1	0.32
	4.66	5.10	260±60	2.3±0.4	0.34
	4.66	5.21	250±20	2.1±0.1	0.42
negative delays	5.00	4.66	40±10	1.1±0.1	0.24
	5.10	4.66	60±30	1.1†	0.34
	5.21	4.66	60±10	1.0±0.1	0.29

signal was fitted globally with a sum of two spectrally different contributions. Based on the findings from Karunakaran et al. [141] and Miannay et al. [84], a sequential model was assumed:

$$S_0 \xrightarrow{\hbar\omega} S_m \xrightarrow{k_1} S_n \xrightarrow{k_2} S_0. \tag{5.8}$$

In this model, the first contribution S_m is prepared by the pump pulse and decays mono-exponentially with the time constant k_1. The signal of the second contribution S_n rises with time constant k_1 and then also decays mono-exponentially with a different time constant k_2. A two-dimensional fit is performed (for the explicit fit function, see equation A.6 in Appendix A.1). Lifetimes similar to the ones obtained by Karunakaran *et al.* and Miannay *et al.* (200 fs and 2 ps) were taken for parameter initialisation.

Figure 5.30 summarises the results of the two-dimensional fits. In the first row (A–C), the raw data are compared to the fit revealing a very good agreement. In the second row (D–F), the residuals are plotted with maximum values of ±15% of the total signal. Again, the fit is plotted on top to easily assign systematic discrepancies if present. However, the residuals are dominated by statistical deviations and reveal a very good agreement of the fits with the datasets. In the third row (G–I), the individual population dynamics for each contribution is plotted. In the last row (J–L), the decay-associated spectra for the individual contributions are shown with the same colour code as the corresponding contribution in the population dynamics.

The lifetimes and relative amplitudes obtained from these 2-dimensional fits are summarised in Table 5.4. There is a faster decaying and a slower decaying contribution for each temporal direction, named τ_{fast} and τ_{slow}, respectively. For positive delays (266 nm pump, tunable probe), the lifetimes are τ^{+}_{fast}= 250–380 fs and τ^{+}_{slow}=2.1–2.4 ps. For negative delays (tunable pump, 266 nm probe), the lifetimes are τ^{-}_{fast}=40–60 fs and τ^{-}_{slow}=1.0–1.1 ps. Due to the poor statistics of the second dataset, τ_{slow} at negative delays was kept constant at 1.1 ps. Both, the fast and the slow lifetime are faster at negative

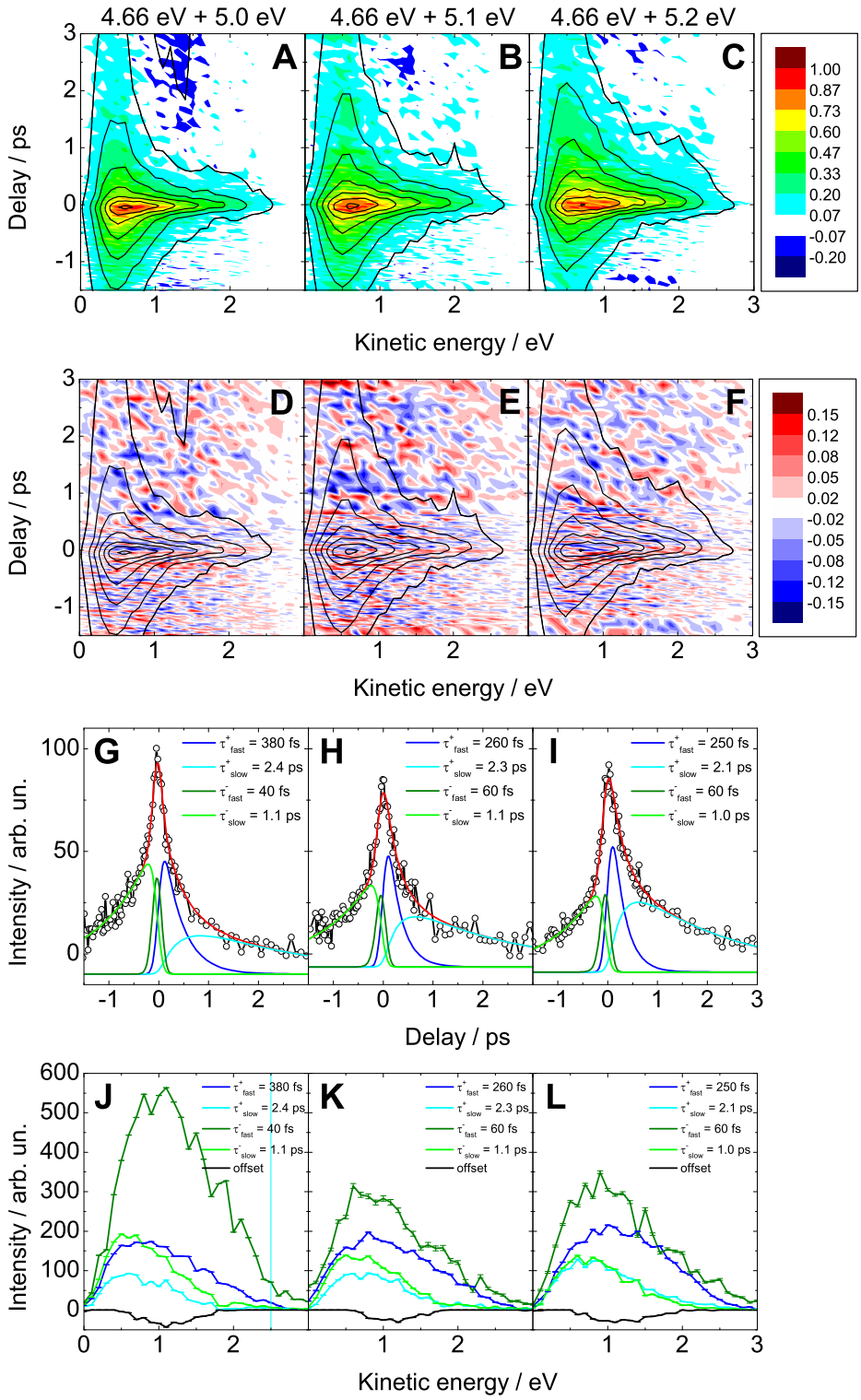

Figure 5.30. Results obtained from fitting the TRPES of guanosine obtained with 266 nm and tunable UV pulses (left column: 248 nm, center column: 243 nm, right column: 238 nm). A–C: Comparison of the global fit (lines) with the measured data (colour), D–F: Residuals (colour) and the global fit (lines), where the colour scale covers a range of ±15 % of the maximum photoelectron signal, G–I: Population dynamics of the individual contributions, J–L: Decay associated spectra of the individual contributions with error bars with the same colour code as in the population dynamics.

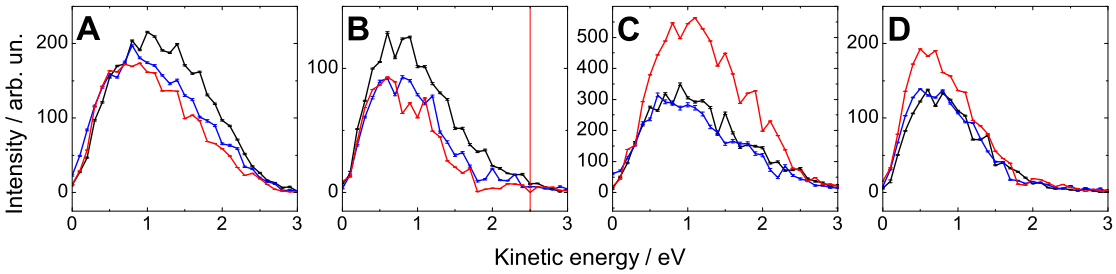

Figure 5.31. Comparison of decay-associated spectra of guanosine solution obtained with different wavelengths. The spectra associated to τ^+_{fast} (A) and τ^+_{slow} (B) were obtained with 4.66 eV pump and different probe phonon energies (red: 5.0 eV, blue: 5.1 eV, and black: 5.2 eV). The spectra associated to τ^-_{fast} (C) and τ^-_{slow} (D) were obtained with different pump phonon energies (red: 5.0 eV, blue: 5.1 eV, and black: 5.2 eV) and 4.66 eV probe photon energy.

delays.

The value A_{rel} gives the relative intensity of the slow contribution with respect to the fast contribution. For a complete population transfer from the first to the second contribution, A_{rel} is 1. In all cases, about one third of the fast decaying population also appears in the slower decaying contribution.

In Figure 5.31, the decay-associated spectra obtained from different wavelength combinations are compared to evaluate the wavelength-dependency. The spectra associated to τ^+_{fast} (A) and τ^+_{slow} (B) were obtained with 4.66 eV pump and different probe phonon energies between 5.0 and 5.2 eV. The general shape of the observed spectra is very similar. At the low-energy side, they are even identical whereas on the high-energy side, the spectra seem to be shifted: extending to slightly higher kinetic energies for higher probe photon energies. Hence, in all three cases the same excited distribution is probed with slightly different photon energies and the spectra are cut off at low kinetic energies due to the magnetic bottle or effects in the liquid jet. The spectra associated to τ^+_{slow} are more narrow and peak at smaller kinetic energies than the spectra associated to τ^+_{fast}.

The spectra associated to decays at negative delays τ^-_{fast} and τ^-_{slow} are shown in Figures 5.31 C and D, respectively. These spectra were obtained with different pump photon energies between 5.0 and 5.2 eV and 4.66 eV probe photon energy. These spectra reveal identical shape only differing in the intensity. This is due to the same probe-photon energy in this temporal direction. This indicates that, varying the pump-photon energy by about 0.2 eV does not change the excited state spectrum.

Comparing the spectra associated to the fast decays τ^+_{fast} and τ^-_{fast}, we find surprising similarities. Even more surprisingly, the spectra associated to the slow decays τ^+_{slow} and τ^-_{slow} are also almost identical although the probe photon energy differs by up to 0.55 eV.

5.4.3. Discussion

The time-resolved photoelectron spectra of guanosine in solution reveal excited state lifetimes that depend on the excitation wavelength. For excitation with 266 nm, excited state lifetimes of about 300 fs and 2 ps were found. The time-dependent spectra reveal a binding energy of about 4.2 eV for the excited state. For excitation around 5 eV, the lifetimes are significantly shorter with about 50 fs and 1 ps. However, the spectra for the fast and the slow contribution are quite similar for the different temporal directions. For both temporal directions, only about one third of the population of the fast contribution appears in the slow contribution.

Motivated by these results, a collaboration with Walter Thiel and co-workers was initiated. Based on their results on hydrated guanine [138], they are currently calculating the time-dependent ionisation energies of guanine in solution (a common publication is being prepared). Preliminary results indicate, that for delay times after about 100 fs the ionisation potential of the excited state is constant at a value of about 4.5 eV (the original value from the simulation has been re-calibrated by comparison of the initial ionisation energy of the excited state (3.54 eV [142]) with the energy gap between the first ground state absorption maximum (∼4.6 eV) and one-photon ionisation energy of the molecule in the ground state (7.2 eV [80])) [142]. Therefore, the potential hypersurface of the ionic ground state must be parallel to the excited state along the relaxation paths. The probe photon energy that we applied in the experiment was up to 5.2 eV. Due to the broad bands in solution, we are able to ionise the excited state along the whole pathway on the S_1 state.

These results are explained with the help of Figure 5.32 which shows schematically the potential energy curve for the ground state, the first exited state, and the ionic ground state of guanosine in solution. For positive delays (A), the molecule is excited with a 266 nm pulse (4.66 eV) preparing the excited state. In the FC region, the excited state potential shows a strong gradient accelerating the excited-state wave packet. At the temporal overlap of the pulses, ionisation of the excited state with a probe pulse of 238 nm will therefore lead to a broad distribution of kinetic energies in the photoelectron spectrum. The wave packet leaves the FC region within about 300 fs. As the wave packet leaves the FC region, the wave packet spreads but the ionic potential curve is now almost parallel to the excited state potential and the observed photoelectron spectrum gets more narrow. The molecule returns to the ground state with a lifetime of about $\tau^{+}_{\mathrm{slow}} \sim 2\,\mathrm{ps}$.

At negative delays (Figure 5.32B), the molecule is excited with higher photon energies up to 5.2 eV (238 nm). The photoelectron spectrum at the temporal overlap is as broad as for positive delays because the potential of the excited state has the same gradient. But with the higher photon energies, a lot more excess energy is introduced in the excited

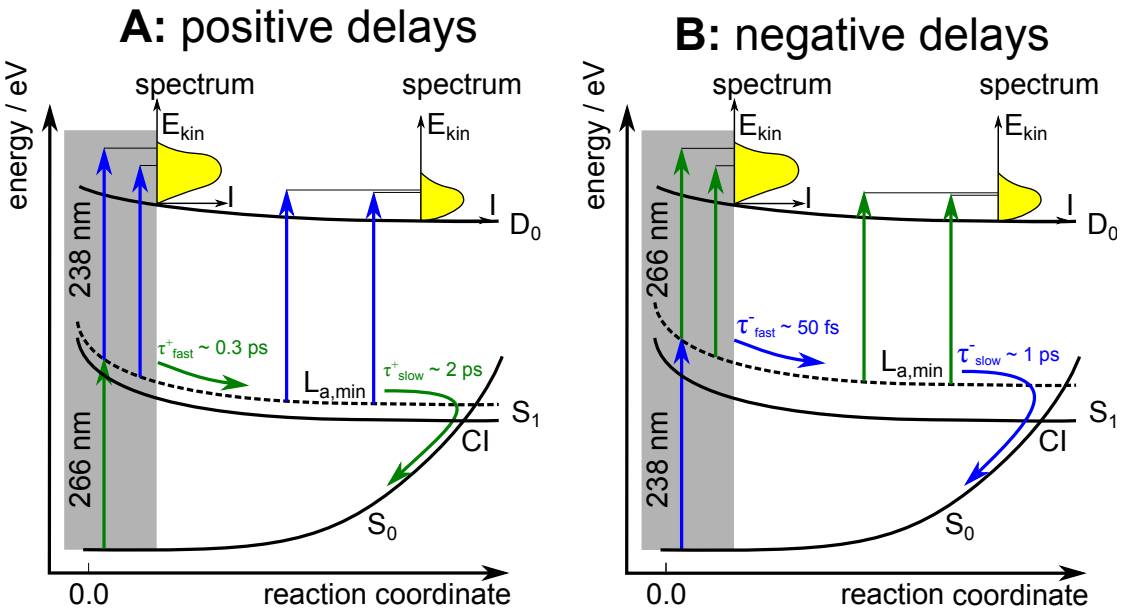

Figure 5.32. Potential energy diagramm for guanosine in solution in order to explain the different results obtained for positive (A) and negative (B) delays. The fast lifetime τ^{+}_{fast} corresponds to the wave packet leaving the FC region (grey) on the excited state S_1 whereas the slow lifetime τ^{+}_{slow} reveals the transfer to the electronic ground state S_0. The spectra associated to τ^{+}_{fast} and τ^{-}_{fast} are broad due to the potential gradient on the excited state in the FC region. At longer delays, the potential curves of the excited state S_1 and the ionic state D_0 are almost parallel leading to a narrowing in the photoelectron spectrum although the wave packet broadens while it evolves on the excited state. The initially excited vibronic level is retained (dashed line) which explains the similarity of spectra at long delays for both temporal directions.

state. This leads to an acceleration of the wave packet dynamics and the FC region is left with a much shorter lifetime of about 50 fs. Again, the wave packet spreads but due to the ionic potential being parallel to the excited state potential, the photoelectron spectrum becomes narrow. The electron kinetic energies are the same as for positive delays, because the vibrational energy is conserved. Due to the accelerated dynamics, the excited state only has a lifetime of 1 ps.

Wavelength dependence. The wavelength dependence only appears in the spectra and lifetimes in positive delays, where the probe-wavelength is varied. For higher photon energies in the probe step, the photoelectron spectrum extends to slightly higher kinetic energies. However, regarding the variation in the lifetime, open questions remain. The lifetime changes from 250 fs for 5.2 eV and 5.1 eV probe photon energy to 380 fs for 5.0 eV photon energy. Limitations due to the FC window for ionisation (too low photon energies) would affect the lifetime in opposite direction, namely shorten the lifetime when the probe photon energy is decreased. For negative delays, the pump wavelength is varied between 5.0 and 5.2 eV. For this direction, the measured lifetimes and decay-associated spectra are identical. Hence, for excitation with high excess energy, slight

changes in the excitation energy do not change the results.

Heggen *et al.* simulated the excited state dynamics of guanine in solution and identified different conical intersections between the excited state and the ground state [138]. However, the hopping time for the different types of S_1/S_0 hopping structures is very similar (200–500 fs). Additionally, the ionisation energy of the excited molecules is also very similar for the different structures [142]. Therefore, we propose the assignment given in Figure 5.32. However, due to the extraordinary good match of the simulated lifetime with the experimental τ^{+}_{fast}, an alternative assignment may also be plausible: τ_{fast} refers to the relaxation of the excited state and τ_{slow} to a second pathway which has not been observed in the simulations.

Comparison with previous results. Karunakaran *et al.* measured the transient absorption of GMP excited with 267 nm and 287 nm and assigned the lifetimes in the following way: 250 fs for transfer from the FC region to the $L_{a,\mathrm{min}}$, 1 ps for transition into the hot ground state and finally 2.5 ps for the hot ground state relaxation [141]. This assignment was challenged by Miannay *et al.* who measured the fluorescence up-conversion signal of GMP excited with 266 nm [84]. They found a dependency of the measured lifetimes on the selected fluorescence wavelength revealing a time-dependent shift of the fluorescence spectrum. A global fit gave lifetimes of 160 fs, 670 fs and 2.0 ps - all assigned to relaxation on the L_a (S_1) potential surface. Since it seems unlikely that the (hot) ground state can be ionised with a probe photon energy of about 5 eV, my results indicate that the excited state is occupied for about 2 ps and therefore support the latter assignment.

5.5. Thymine and thymidine

5.5.1. Current state of knowledge

Figure 5.33 shows the lowest energy tautomers of isolated thymine. The canonical tautomer is the keto-tautomer (T1). In a polar environment (e.g. aqueous solution), tautomers with large dipole moments are stabilised. The dipole moments and energies of the tautomers of isolated thymine suggest that in aqueous solution only the keto-tautomer (T1) is present with significant abundance [143]. In the case of thymidine, the sugar moiety is attached to the $N1$ position - also favouring the same tautomer (T1).

In the gas phase, the first excited state of thymine in the Franck-Condon region is an optically dark $n\pi^*$ state and the second excited state is a bright $\pi\pi^*$ state (see Figure 5.4). The transition into this second excited state leads to an intense absorption band at around 250 nm (4.95 eV) in the gas phase [144]. Further excited states ($\pi\pi^*$) were observed at about 6.2 eV and 7.4 eV in the gas phase [144] but are to high in energy to play any role in the deactivation process.

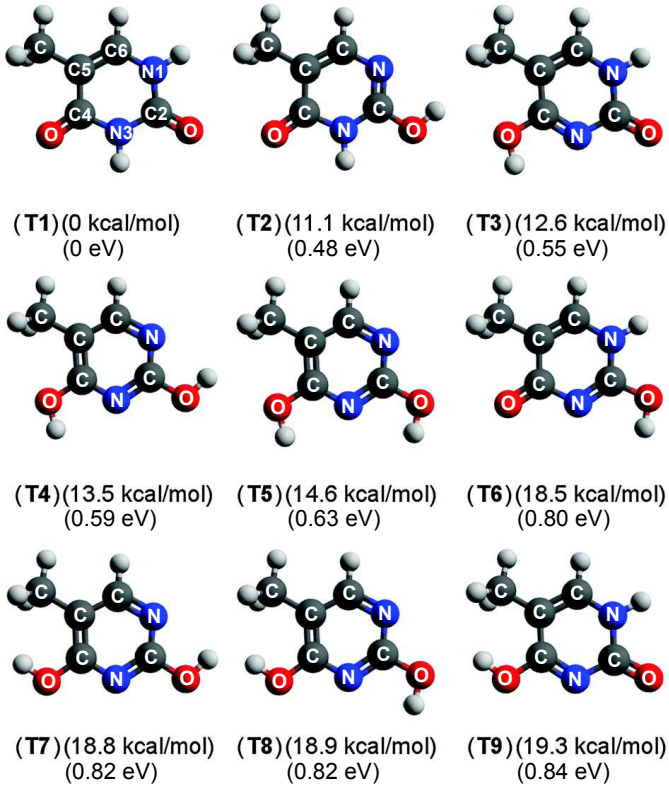

Figure 5.33. Tautomeric structures of isolated thymine and their relative ground state energies [85]. In this case, the energy difference to the lowest energy tautomer is too large to be compensated by a higher stabilzation due to a larger dipolemoment [143].

Time-resolved spectroscopy on isolated DNA bases has been performed by Kang *et al.* and Ullrich *et al.* [145, 146]. Kang *et al.* measured the transient ion signal after excitation with 267 nm and delayed ionisation with 800 nm pulses in a three-photon process [145]. Besides a Gaussian cross-correlation signal, they found a bi-exponential decay with lifetimes of 6.4 ps and >100 ps. The latter was assigned to a low-lying triplet state accessible in the gas phase. Ullrich *et al.* performed time-resolved photoelectron spectroscopy on isolated DNA bases. They used 250 nm (4.96 eV) pulses to excite the molecules and 200 nm (6.20 eV) pulses to ionise. They do not observe any time-dependent spectral change of the photoelectron signal and fitted their signal with three exponentially decaying contributions, where the longest was fixed to 6.4 ps (taken from Kang *et al.*). The other two lifetimes were <50 fs and 490 fs for thymine [146]. The triplet state was not observed in this case. Very recent experimental data on isolated thymine show a 200 fs electronic relaxation without any indication for a barrier on the $\pi\pi^*$ state [147]. Comparing their results with simulations of Auger spectra, they also suggest involvement of an $n\pi^*$ state.

There has been a lot of effort from theory to explain the results obtained from these

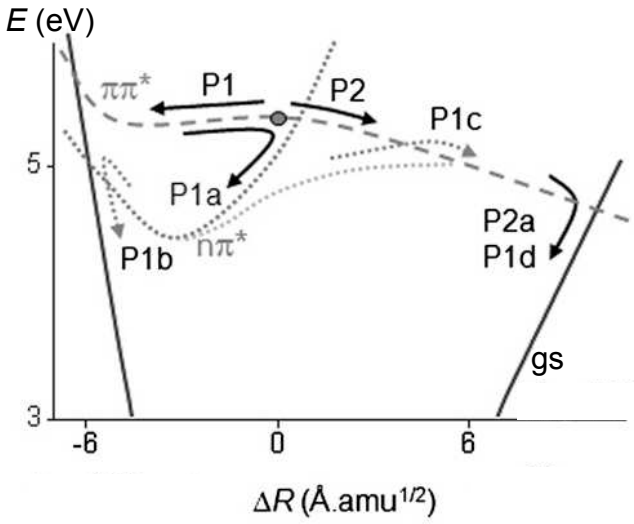

Figure 5.34. Different pathways predicted for the excited state relaxation of isolated thymine. Figure taken from Ref. [148].

gas phase experiments and to assign distinct pathways [148–155] as summarised in Figure 5.34. Merchán *et al.* proposed a relaxation pathway that occurs only on the ππ* hypersurface [149]. They assigned the sub-ps lifetime to a direct transition from the excited ππ* state to the ground state and the longer-lived contribution to a planar minimum on the ππ* state where the population is trapped. Hudock *et al.* and Szymczak *et al.* found a fs-transfer from the FC region to a minimum of the ππ* potential surface [154, 155]. According to them, a small barrier to the ππ*/nπ* conical intersection would then result in the ps decay observed in the experiments. Asturiol *et al.* found two relaxation pathways [150]: a direct pathway and an indirect pathway *via* the nπ* state. Both paths start with a small barrier on the ππ* state which has to be overcome initially. A part of the population then passes a conical intersection directly into the ground state. The remaining population decays *via* the nπ* state which has a pronounced minimum giving rise to the ps lifetime. The sub-ps lifetime refers to the de-population of the ππ* state including both, the direct transition to the ground state and the population transfer to the nπ* state. Lan *et al.* found a barrierless transition on the ππ* surface to the ππ*/nπ* conical intersection giving rise to the fs-lifetime and a subsequent trapping of the population in the nπ* state leading to a ps decay [151]. In more recent works, a population transfer from the ππ* state to the nπ* state on the femtosecond timescale was predicted for isolated thymine [148, 152]. While Picconi *et al.* found a significant population of the nπ* state upon excitation of the ππ* state [152], Barbatti *et al.* even proposed a complete population transfer to the nπ* state [148]. In contrast, recent QM-MD simulations of excited state dynamics of isolated thymine find no indication for involvement of the nπ* state but assign the whole relaxation pathway to dynamics on

the ππ* potential surface [153].

Also solvated thymine has been studied experimentally applying different femtosecond time-resolved spectroscopy techniques [2, 122, 139, 156–159]. First femtosecond studies on transient absorption of DNA bases including thymine have been published by the Kohler group [2, 122, 139, 156]. They found a sub-ps decay of the excited state signal (720 fs) and a bi-exponential re-population of the ground state minimum. This delayed re-population was assigned to a relaxation *via* the dark nπ* state. For thymine an nπ* state lifetime of 30 ps was deduced [156]. Gustavsson and co-workers have studied thymine extensively applying fs fluorescence up-conversion in different protic and aprotic environments [157–159]. They observed two lifetimes: an ultra-short contribution below 200 fs and a longer-lived contribution which was strongly solvent dependent (630 fs in water) [157, 159]. They did not observe the 30 ps contribution of the nπ* state, but this was not expected in fluorescent up-conversion experiments because transitions from the nπ* state to the ground state are optically dark.

Theoretical calculations on solvated thymine are rare. The first theoretical study on a similar molecule in solution was performed by Improta *et al.* [160]. They studied the excited state dynamics of uracil in solution explicitly including the exciting laser pulse which turned out to be an important feature. Uracil only differs from thymine by lacking the methyl group at the $C5$ atom. Their calculations show that the potential energy surfaces of the nπ* state and the ππ* state cross along the de-excitation path on the ππ* surface. They therefore can explain an ultrafast population transfer from the ππ* state to the nπ* state in less than 100 fs in aqueous solution and suggest a similar behaviour for solvated thymine.

Recently, QM/MM molecular dynamics simulations about excited state relaxation of thymine in aqueous solution were published by Nakayama *et al.* [153]. In contrast to the pronounced involvement of the nπ* state in the calculations of Improta *et al.* (see above), these new simulations find no indication for any role of the nπ* state in the deactivation process. As shown in Figure 5.4, the lowest excited state of thymine in water is the ππ* state. Upon excitation of this ππ* state of the solvated thymine, Nakayama *et al.* found two distinct relaxation pathways *via* two conical intersections with the ground state. The two corresponding structures at the CIs are shown in Figure 5.35. The first CI involves a twisting of the $C5$–$C6$ bond with a strong puckering of the $C6$ atom and is labelled as $(^1\pi\pi^*(C5\text{–}C6)/S_0)_{CI}$. The second CI is associated to an out-of-plane displacement of the carbonyl group and is labelled as $(^1\pi\pi^*(C4\text{–}O8)/S_0)_{CI}$. According to Nakayama *et al.*, this second pathway only appears for excited thymine in solution and was absent in their calculations on the isolated thymine.

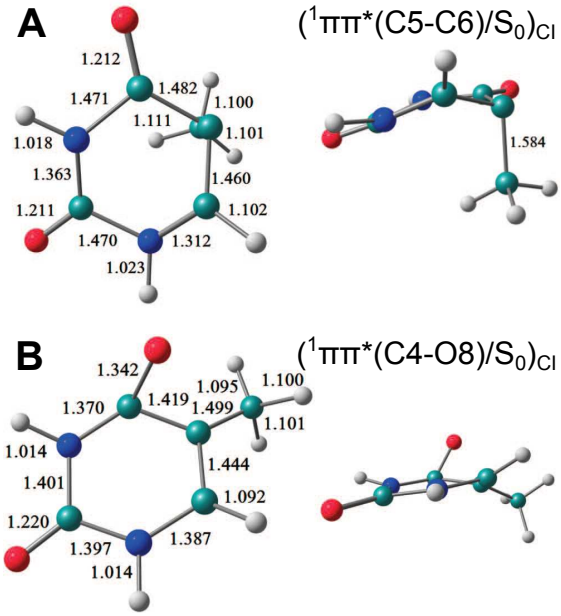

Figure 5.35. Snapshots of thymine at the conical intersections that are involved in the electronic de-excitation of thymine in solution. [153]

5.5.2. TRPES results

Figures 5.36 and 5.37 show the time-resolved photoelectron spectra of thymine and thymidine, respectively. For both molecules, photoelectron kinetic energies ranging up to about 2.5 eV are observed in a pump-probe delay range from -0.5 ps to 1 ps. These data were analysed in terms of a global fit including the convolution of a Gaussian cross-correlation and an exponential decay, both for positive and negative delays (accounting for excitation with 266 nm or 238 nm). The explicit fit function is given in equation A.7 (see appendix A.1). All fit results are summarised in Table 5.5. Following the observation of Ullrich *et al.*, a time-dependent spectral shift of the individual contributions was not included [146].

In a first version, only a single contribution for each temporal direction was assumed. The results of this fit are shown in Figures 5.36(a,d,g,j) and 5.37(a,d,g,j) for thymine and thymidine, respectively. These fits give reasonable agreement with the data but there are still systematic deviations as revealed by the residuals in 5.36d and 5.37d. These show rather positive values at early negative delays and negative values at positive delays. Therefore, the model was extended to a second contribution and parallel pathways have been assumed:

$$S_0 \xrightarrow{\hbar\omega} \begin{cases} S_m & \xrightarrow{k_1} S_0, \\ S_n & \xrightarrow{k_2} S_0. \end{cases} \tag{5.9}$$

Table 5.5. Fitparameters of the global analysis of thymine and thymidine assuming n contributions to the signal. The lifetimes τ_1 and τ_2 refer to decays at positive delays (pump 266 nm, probe 238 nm) and the lifetimes τ_3^- and τ_4^- to decays at negative delays (pump 238 nm, probe 266 nm). The parameter $\beta = \frac{A_3^- + A_4^-}{A_1^+ + A_2^+}$ gives the ratio between signal in negative delay direction and signal in positive direction, with $A_i = \int_0^\infty a_i(E_{\mathrm{kin}})\mathrm{d}E_{\mathrm{kin}}$ (for $a_i(E_{\mathrm{kin}})$ see Equation A.7 in Appendix A.1). The uncertainties of the lifetimes correspond to one standard deviation as obtained from the fit.

	n	τ_1 / fs	τ_2 / fs	τ_3^- / fs	τ_4^- / fs	β
thymine	2 (1+1)	240±10	–	140±40	–	0.29
	3 (2+1)	70±10	410±40	320±40	–	0.08
	2 (FU [157])	195±17	633±18	–	–	–
	2 (TA [156])†	–	720±70	–	–	–
	4 (2+2)	80±10	420±10	70±10	430±10	0.14
thymidine	2 (1+1)	260±10	–	230±30	–	0.13
	1 (FU [140])	–	700±120	–	–	–
	1 (TA [122, 139])	–	540±40	–	–	–
	3 (2+1)	120±10	390±10	290±20	–	0.09
	2 (FU [121])	150±20	720±30	–	–	–
	4 (2+2)	140±10	430±10	3±10	310±10	0.73
TMP	1 (FU [140])	–	980±120	–	–	–
	2 (TA [156])‡	–	410±90	–	–	–

† additional lifetime of $\tau_{\mathrm{long}} = (30\pm13)$ ps for re-population of the ground state

‡ additional lifetime of $\tau_{\mathrm{long}} = (127\pm15)$ ps for re-population of the ground state

In this model, S_m and S_n may either be two different excited states or refer to different trajectories within the same excited state. But in any case, k_1 and k_2 reveal the temporal evolution of two different points in phase space that are directly populated by the pump pulse. Hence, the data cannot be fitted well with a single exponential characterised by $k = k_1 + k_2$. For negative delays, a single contribution was used in this second fit shown in Figures 5.36(b,e,h,k) and 5.37(b,e,h,k). Figure 5.36b shows the experimental data of thymine (colour) and the fit (lines). In Figure 5.36e, the residuals from the fit are shown. At positive delays, the residuals vary statistically around zero and the model fits well to the data. At early negative delays, however, the residuals are systematically more positive (red) revealing an underestimation of the data by the model. These deviations seem to arise from a very tiny temporal shift of the excited state population decay (cf. Figure 5.36k) which may simply reflect the limitations of using an exponential decay model to fit the population. In fact, the prepared wave packet needs some time to spread and reach the conical intersection. It is therefore reasonable to expect a small delay in the excited state de-population.

The decay associated spectra and population dynamics of individual contributions are shown in Figures 5.36h and k, respectively. In positive delay direction, contributions with lifetimes of 70 fs and 410 fs are observed for thymine. The average kinetic

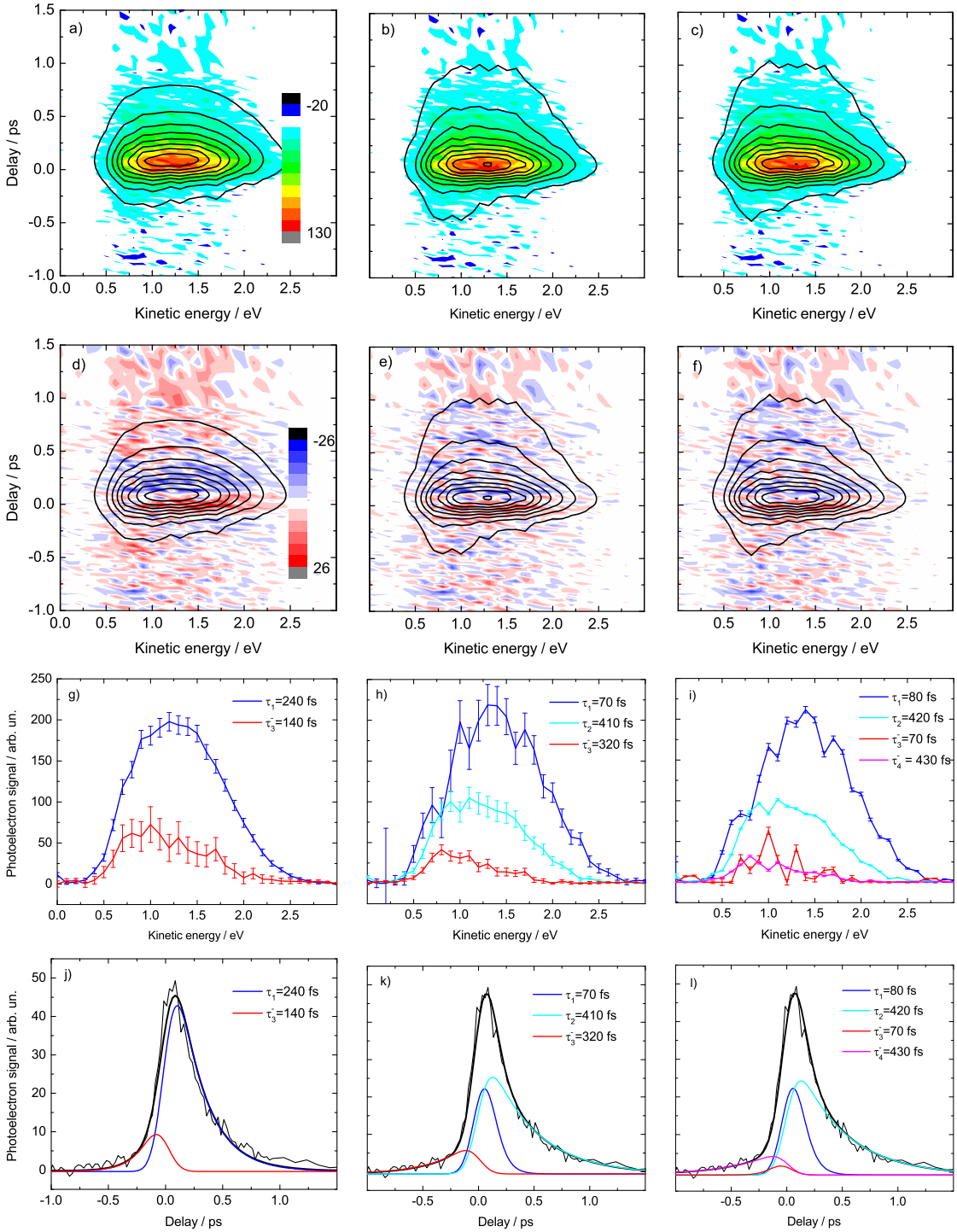

Figure 5.36. Time-resolved photoelectron spectrum of thymine in solution obtained with 266 nm and 238 nm pulses. A global analysis including two (left column), three (center column), and four contributions (right column) was performed. a-c) Comparison of the global fit (lines) with the measured data (colour), d-f) Residuals (colour) and the global fit (lines), where the colour scale covers a range of ±15 % of the maximum photoelectron signal, g-i) Decay associated spectra of the two, three, or four contributions with error bars, j-l) Population dynamics of the individual contributions with the same colour code as in the decay associated spectra.

energies (AKE, see equation 5.3.2) for thymine are 1.42 eV and 1.26 eV for the fast and the slowly decaying component in positive delay direction, respectively. The contribution towards negative delays shows a lifetime of 320 fs and has an AKE of 1.08 eV. The probe-photon energy difference between positive and negative delay direction is (5.2 eV–4.65 eV=0.55 eV). Hence, the AKE of the contribution in positive direction should be shifted by 0.55 eV with respect to the same contribution in negative direction. However, this is not the case. In all our liquid jet experiments, we have observed that the photoelectron signal is in general strongly reduced at very low kinetic energies [79]. However, this is not the case for experiments with nitric oxide in the gas phase, i.e. it is not given by properties of the spectrometer itself. The reason for this reduction of signal is possibly a cloud of charged water clusters surrounding the liquid jet [37]. Due to this reduced signal at low kinetic energies, an overestimation of the average kinetic energy can be assumed, especially for the case of the lower probe photon energy in negative delay direction. For adenine / adenosine a very good agreement of the maximum kinetic energy with the probe photon energy difference has been demonstrated (see Section 5.3.2 or [79]). In the case of thymine, the maximum kinetic energies of the individual contributions are 2.8 eV and 2.6 eV at positive delays and 2.0 eV at negative delays (cf. Figure 5.36b). The difference between the maximum kinetic energy of the slower contribution in positive delay direction and the contribution in negative delay direction matches the probe photon energy difference. This indicates that both contributions originate from the same relaxation path. This would indicate the absence of the faster decaying contribution at negative delays. However, due to the low signal at negative delays, a deconvolution is very difficult (see the subsequent paragraph), and a combination of fast and slowly decaying contribution at negative delays cannot be excluded.

The corresponding data and fits for thymidine are shown in Figure 5.37. For completeness, the fits again include two, three, or four contributions. The fit with three contributions is preferred for the same reasons as in the thymine case and discussed in detail. For the contributions in positive delay direction (266 nm pump, 238 nm probe), we found lifetimes of 120 fs and 390 fs, and for the contribution in negative delay direction (238 nm pump, 266 nm probe) 290 fs. These lifetimes are almost identical to the excited state lifetimes of thymine – only the short lifetime at positive delays is slightly longer for thymidine.

The AKE for the two contributions in positive delay direction are 1.43 eV for the faster decaying contribution and 1.19 eV for the slower one. For the contribution in negative delay direction, we observe an AKE of 1.00 eV. Again, these values do not reveal the probe photon energy difference of 0.55 eV for positive and negative delays. But the maximum kinetic energies are 2.9 eV and 2.6 eV for the fast and slow contribution in positive delay direction and 2.0 eV in negative delay direction. Again, the difference between the

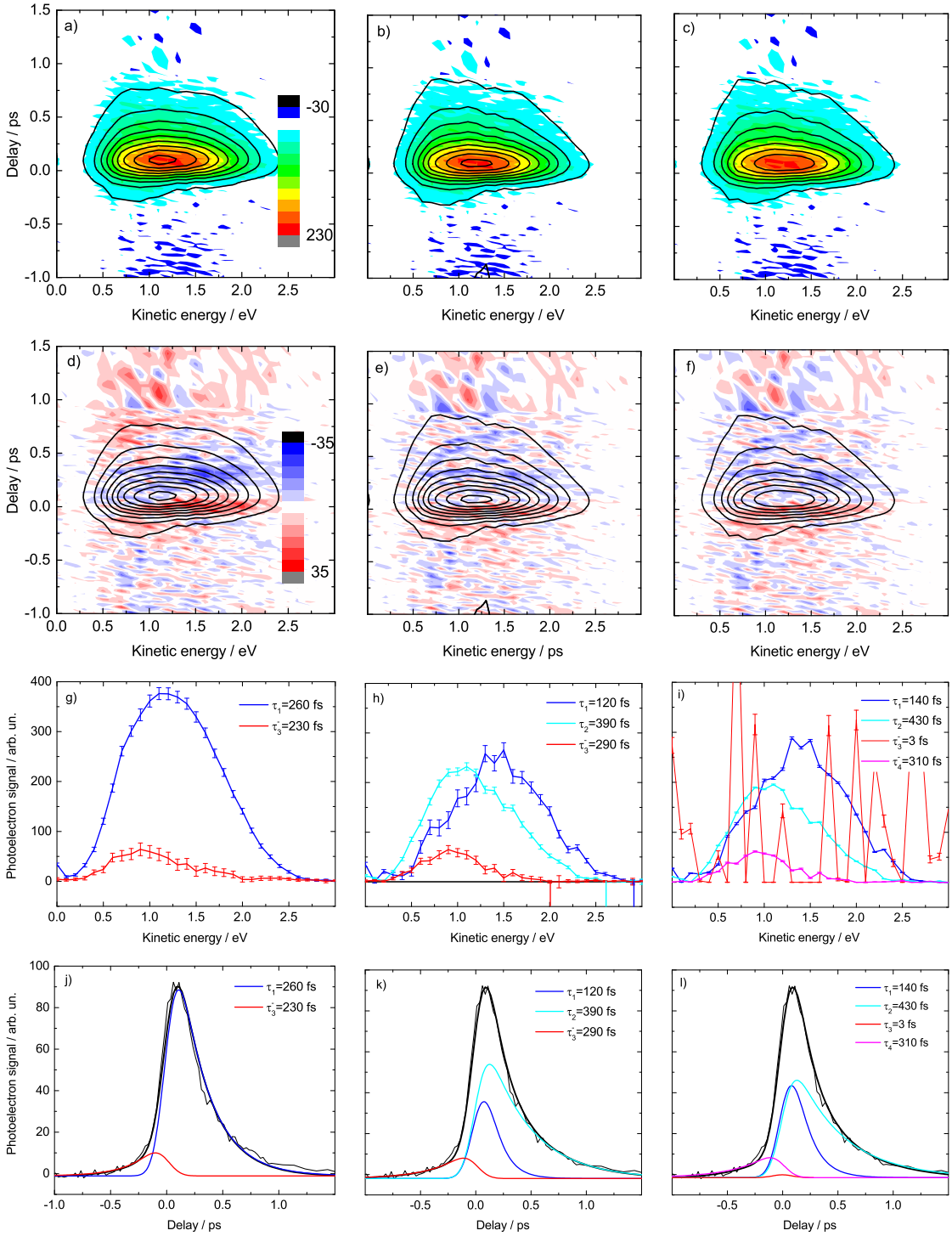

Figure 5.37. Time-resolved photoelectron spectrum of thymidine in solution obtained with 266 nm and 238 nm pulses. A global analysis including two (left column), three (center column), and four contributions (right column) was performed. a-c) Comparison of the global fit (lines) with the measured data (colour), d-f) Residuals (colour) and the global fit (lines), where the colour scale covers a range of ±15 % of the maximum photoelectron signal, g-i) Decay associated spectra of the two, three, or four contributions with error bars, j-l) Population dynamics of the individual contributions with the same colour code as in the decay associated spectra.

maximum kinetic energy of the slower contribution in positive delay direction and the contribution in negative delay direction matches the probe photon energy difference.

For comparison, also a global analysis with four contributions (two for each temporal direction) was performed, as shown in Figure 5.36(c,f,i,l) and Figure 5.37(c,f,i,l) for thymine and thymidine, respectively. This fit gives similarly good agreement with the data as the one with three contributions. Also the lifetimes are very similar. For thymine, the very quickly decaying contribution at negative delays has only a very small amplitude compared to the total signal (see Figure 5.36l). For thymidine, this contribution is even smaller and reveals an unrealistically short lifetime of only 3 fs. Therefore, we can conclude, that a fit with three contributions is sufficient – especially, since the main focus of this work lies on the dynamics upon excitation with 266 nm (positive delays). Due to the large similarities of the data and fits of thymine and thymidine, we can conclude that the excited states of both molecules relax along the same coordinates and that the sugar moiety only plays a minor role (e.g. by slightly extending the lifetimes).

5.5.3. Discussion

In their fluorescence up-conversion experiments, Gustavsson *et al.* found a bi-exponential decay of the signal of thymine and thymidine upon excitation with 267 nm pulses. The deduced lifetimes of 195 fs and 630 fs for Thy and <150 fs and 690 fs for Thd were all assigned to the decay of the ππ* state [157, 161]. In experiments on transient absorption, Kohler and co-workers found a mono-exponential decay (540 fs) of the ππ* excited state of thymidine in early experiments [122, 139]. A more detailed study on thymine (and its nucleotide, TMP) revealed a 720 fs (410 fs) lifetime of the excited state and a bi-exponential re-population of the vibronic ground state suggesting that a significant part of the excited state population is trapped in a dark state [156]. They found a lifetime of 30 ps (127 ps) for the decay of the dark state in thymine (TMP). This dark state was suggested to be the lowest nπ* state [156, 160, 162]. In contrast, recent QM/MM molecular dynamics simulations suggest that the relaxation only occurs along two different coordinates on the same ππ* potential [153]. The observed ground state re-population times in this study suggest a sub-ps decay of the excited states. The excited-state lifetimes presented here are in agreement with both, fluorescence up-conversion lifetimes and QM/MM molecular dynamics simulations.

Motivated by the good agreement of our experimental data with the QM/MM molecular dynamics simulations [153], a collaboration was established with A. Nakayama. Based on his theoretical work, Nakayama calculated the time-dependent energy of the ionic ground state (D_0) of solvated thymine. In Figure 5.38A and B, potential energies along representative trajectories are shown for the ground state and the excited states

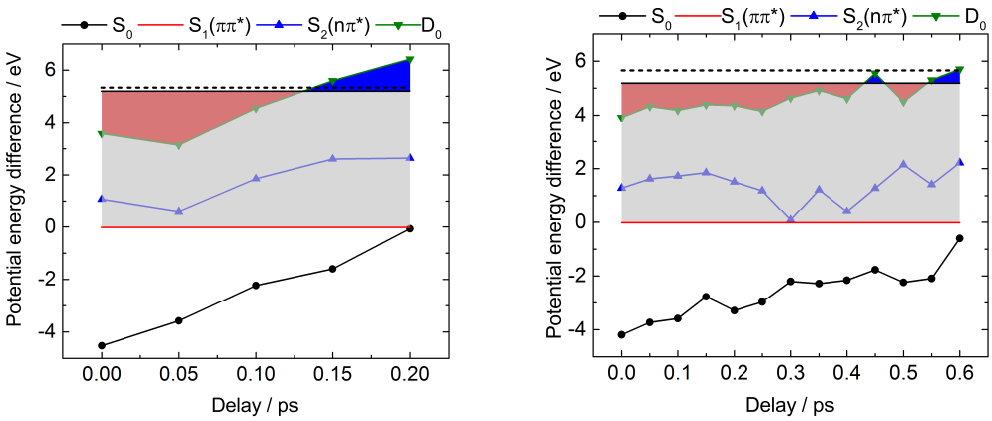

Figure 5.38. Time-dependent potential energies of all relevant states along two representative trajectories that reach the regions of (a) $^1\pi\pi^*(C5\text{–}C6/S_0)_{CI}$ and (b) $^1\pi\pi^*(C4\text{–}O8/S_0)_{CI}$. All potential energies are given relative to the $S_1(\pi\pi^*)$ potential energy. The potential energies of the excited states ($S_1(\pi\pi^*)$, red squares and $S_2(n\pi^*)$, blue triangles) and neutral ground state (S_0, black circles) are taken from Ref. [153]. The potential energy of the ionic ground state ($D_0(\pi^{-1})$, green triangles) was calculated by Akira Nakayama [163]. For the case of instantaneous and complete redistribution of the excess energy, the ionisation window is given by $E(\pi\pi^*)+\hbar\omega_{probe}$ (black solid line) for a 5.2 eV photon. The black diamond shows the total photon energy ($\hbar\omega_{pump}+\hbar\omega_{probe}$) which only seems to be higher in b) due to the slightly lower absolute energy of the $\pi\pi^*$ state. Red shaded areas are regions where the probe photon energy is large enough to ionise the $\pi\pi^*$ state. The blue shaded areas denote regions where the energy of ionic ground state is too high and hence the molecule cannot be ionised by the probe photon. Along the pathway towards the $^1\pi\pi^*(C5\text{–}C6/S_0)_{CI}$ (a), the ionic ground state energy increases by about 3 eV within the first 200 fs making ionisation impossible already at ∼130 fs after excitation. However, along the second pathway, relaxation is much slower, and the ionic ground state energy rises less steeply. Therefore, the molecule can be ionised for a much longer period up to about 500 fs along this pathway.

of thymine – relative to the excited $\pi\pi^*$ state. Besides the temporal evolution of the relative energies of the ground state (S_0, black circles), the $\pi\pi^*$ state (S_1, red line), and the $n\pi^*$ state (S_2, blue triangles), also the relative potential energy of the ionic ground state (D_0, green triangles) is depicted. For both representative trajectories, the potential energy of the $n\pi^*$ state is above the $\pi\pi^*$ potential energy suggesting that the $n\pi^*$ state is not involved in the relaxation. The black horizontal line at 5.2 eV relative energy denotes the photon energy of the probe pulse. As long as the probe photon energy is higher than the ionic ground state energy (red area), the excited state can be ionised. If the relative ionic ground state energy gets higher than the probe photon energy (blue area), then the $\pi\pi^*$ state cannot be ionised any more. For the representative trajectory towards the $^1\pi\pi^*(C5\text{–}C6/S_0)_{CI}$) (see Figure 5.38A), the observation time is limited to about 130 fs. In contrast, for the second representative trajectory *via* the $^1\pi\pi^*(C4\text{–}O8/S_0)_{CI}$ shown in Figure 5.38B the $\pi\pi^*$ state can be ionised all along the relaxation path. This indicates an assignment of the measured lifetimes: the short lifetime corresponds to the

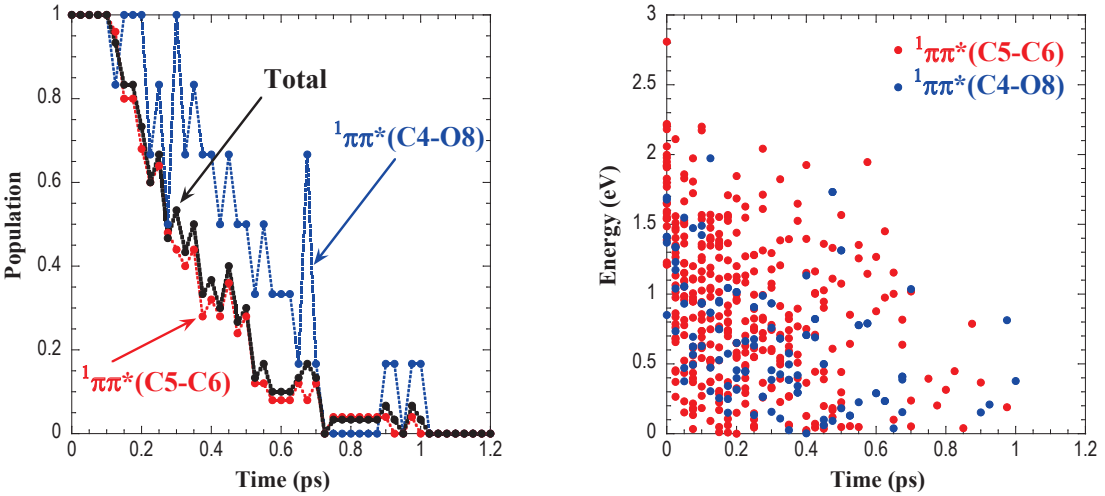

Figure 5.39. Results of simulation with 30 trajectories reaching either the $(^1\pi\pi^*(C5–C6/S_0)_{CI}$ (red) or the $(^1\pi\pi^*(C4–O8/S_0)_{CI}$ region (blue). **Left:** Time-dependent population in the $^1\pi\pi^*$ excited state. The black line shows the average of all trajectories. **Right:** Kinetic energies of photoelectrons along the trajectories for ionisation with 5.2 eV photon energy. At t=0 ps, the average of all kinetic energies is 1.72 eV. The average over kinetic energies of trajectories that reach the $(^1\pi\pi^*(C5–C6/S_0)_{CI}$ and $(^1\pi\pi^*(C4–O8/S_0)_{CI}$ regions are 1.80 and 1.40 eV, respectively.

relaxation *via* the $^1\pi\pi^*(C5–C6/S_0)_{CI}$ and the long lifetime to the relaxation *via* the $^1\pi\pi^*(C4–O8/S_0)_{CI}$. Further trajectories towards both conical intersections were simulated by Akira Nakayama and the results will soon be published in a common paper [163].

This assignment is supported by comparing the decay associated spectra with the results from QM/MM molecular dynamics simulations [163]. Figure 5.39 shows the time-dependent population in the excited state which can be ionised by a probe photon with 5.2 eV photon energy (a) and the expected kinetic energy of the photoelectron at different delays (b). The trajectories were assigned to two groups: one evolving towards the $^1\pi\pi^*(C5–C6/S_0)_{CI}$ and the second towards $^1\pi\pi^*(C4–O8/S_0)_{CI}$. The trajectories from the latter group stay in the excited state for a longer time before they hop to the ground state or leave the FC window for ionisation. The kinetic energies calculated from these trajectories are on average higher for the relaxation towards $^1\pi\pi^*(C5–C6/S_0)_{CI}$ than towards $^1\pi\pi^*(C4–O8/S_0)_{CI}$. In the first case, we find an average kinetic energy of 1.8 eV at the temporal overlap and in the second case, the kinetic energy amounts to 1.4 eV. With increasing delay, the ionisation energy quickly increases due to the evolving dynamics and the corresponding photoelectron kinetic energy decreases. For comparison with the measured spectra, we have to consider the limited time-resolution of the experiment. Averaging over all kinetic energies up to 100 fs, we find an average kinetic energy of 1.14 eV for relaxation towards $^1\pi\pi^*(C5–C6/S_0)_{CI}$ and 1.05 eV for relaxation towards

$^1\pi\pi^*(C4\text{–}O8/S_0)_{CI}$. This is only slightly lower than the average kinetic energy retrieved for the fast and slowly decaying contribution, i.e. 1.42 and 1.26 eV, respectively. For both, the excited state lifetime and the photoelectron spectrum, we find a qualitative agreement between the QM/MM molecular dynamics simulations and the experiment. We assign the short-lived contribution to a wave packet evolving along the relaxation path associated to the $^1\pi\pi^*(C5\text{–}C6/S_0)_{CI}$, whereas the longer-lived contribution reveals a wave packet relaxing through the $^1\pi\pi^*(C4\text{–}O8/S_0)_{CI}$.

Why do we not observe signal from the nπ state?* It has been discussed, that in aqueous solution, a part of the excited state population of thymine is trapped in the nπ* state with a lifetime of 30 ps [156]. Hence, we should observe some signal at long delays if this state was occupied and if the photon energy was high enough to ionise this state. We do not observe any pump-probe signal lasting longer than about 2 ps. Therefore, I have to discuss if the nπ* state can be ionised by a 5.2 eV photon. Within an in-house collaboration, Hans-Herrmann Ritze performed *ab-initio* calculations on isolated thymine employing the MOLPRO2010.1 package [164]. Assuming C_s symmetry and using the aug-cc-pVTZ basis set, the equilibrium structure of the nπ* electronic state was obtained at the CASPT2 level of theory. Applying the MR-CISD(+Q) method, the vertical ionisation energy from the nπ* to the $D_1(n^{-1})$ cationic state was computed for this geometry and a value of 5.48 eV was found for isolated thymine. For the hydrated molecule, we expect a lowering of this value by about 0.9 eV due to solvatochromic shifts [80, 165, 166]. Therefore, the vertical ionisation energy of hydrated thymine would be expected at about 4.6 eV for the nπ* minimum geometry. This is easily accessible with 5.2 eV probe photons. Hence, if the nπ* state was populated to significant amounts, we would expect a signal around 0.6 eV with a lifetime of about 30 ps. Especially at longer delays when the signal from the ππ* state has decayed, the nπ* signal would be easily detectable. The fact that we do not observe any long-lived signal strongly suggests that the nπ* state is not significantly populated and not involved in the excited-state relaxation of thymine. The bi-exponential re-population of the vibronic ground state observed in transient absorption [156] might instead reflect ground state dynamics (e.g. hot-ground-state cooling) along the different relaxation paths.

5.6. Cytosine and cytidine

5.6.1. Current state of knowledge

Cytosine is in structure quite similar to thymine (discussed in the previous section). But in contrast to thymine, cytosine appears in several tautomers in the gas phase. Therefore, excited state dynamics of cytosine in the gas phase is quite complex and

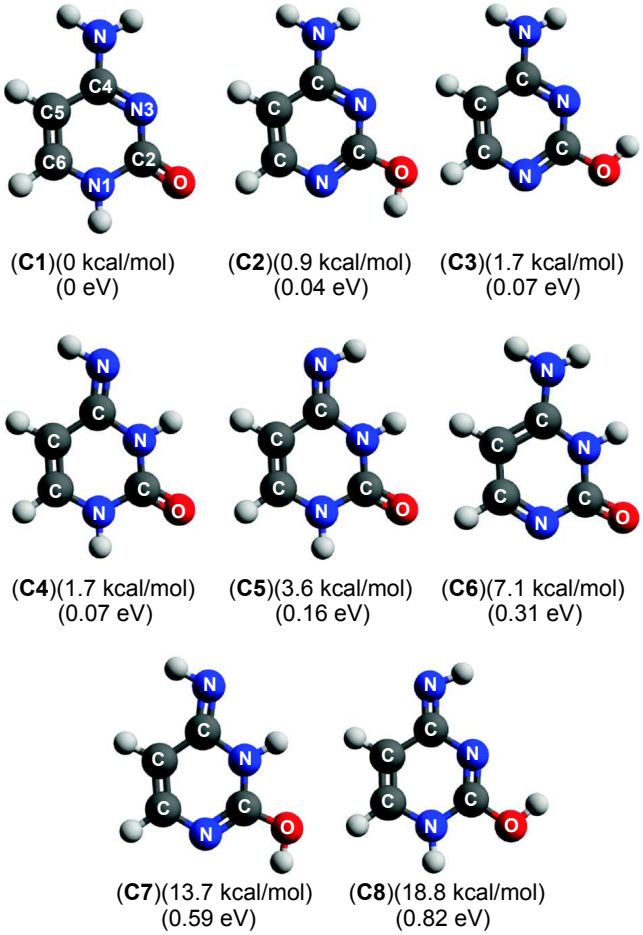

Figure 5.40. Tautomeric structures of isolated cytosine [85]. The tautomers are ordered according to the ground-state energy. In aqueous solution, the canonical tautomer (C1) is much better hydrated than the enol- and imino-forms [169] and is the only tautomer of cytosine in aqueous solution.

difficult to interpret. Figure 5.40 shows the lowest eight tautomers with their relative ground state energies found in a recent coupled-cluster calculation [85]. Experimentally, three tautomers have been distinguished: the keto- (C1), the enol- (C2, C3) and the keto-imino-tautomer (C4, C5) [167]. The exact relative abundance of the keto-, enol- and keto-imino-tautomer in the gas phase is still under discussion [168, references therein].

Kosma *et al.* and Ho *et al.* performed experiments on isolated cytosine accounting for the tautomers present in the gas phase [78, 168]. Kosma *et al.* observed the time-dependent ion signal after excitation with a tunable pump pulse and delayed ionisation with several photons of a 800 nm probe pulse. Depending on the excitation wavelength, they found different excited state lifetimes and assigned these to different tautomers. Ho *et al.* compared the excited state lifetimes of cytosine with the excited state lifetimes of 1-methyl cytosine and 5-fluoro cytosine where different tautomers are favoured. Both

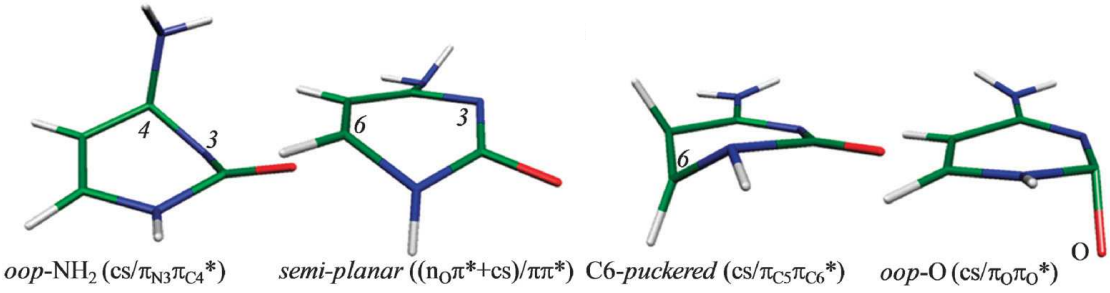

Figure 5.41. Structures at conical intersections of isolated keto cytosine [170].

groups came to the conclusion that upon ππ* excitation, the enol-tautomer decays on a timescale of several picoseconds whereas the keto- and imino-tautomers decay much faster.

In numerous theoretical studies on excited state relaxation of cytosine, several conical intersections with the ground state have been identified. However, the labelling of the CIs is quite different for individual studies. Therefore, a labelling according to Barbatti *et al.* is chosen here [170, cross-references therein]. The conical intersections are shown in Figure 5.41: the *oop-NH_2* CI is connected to a strong out-of-plane (oop) motion of the amino group and puckering of the atoms $N3$ and $C4$ [151, 171–176]; the *semi-planar* CI is characterised by a $C5$–$C6$ bond length increase and a $C2$–$N3$ bond length decrease [171–173, 175, 176]; the *C6-puckered* CI involves a twist around the $C5$–$C6$ bond leading to a puckering of the $C6$ atom [151, 171, 174–179]; and the *oop-O* CI is connected to a strong out-of-plane motion of the O atom while the ring stays almost planar [170]. This latter CI lies at a quite high energy for isolated cytosine. Therefore, it is not involved in the relaxation of isolated cytosine.

The relative importance of those CIs is not as clear (see Table 5.6). Hudock and Martínez find most excited molecules to relax towards the *oop-NH_2* CI [175]. Lan *et al.* see all the excited molecules relax along the *C6-puckered* geometry. Barbatti *et al.* observed the main fraction of the excited molecules relaxing towards the *semi-planar* CI. Also the most recent studies by Nakayama *et al.* and Mai *et al.* do not provide a consistent picture: Nakayama *et al.* see most molecules relax via the *C6-puckered* CI while Mai *et al.* observe a broad distribution in the pathways including the triplet manifold where 25% of the trajectories get trapped.

Calculations of Nakayama *et al.* [180] show, that the excited state dynamics of the isolated cytosine is different for the imino-, keto-, and enol-tautomer. The lifetimes, they found were remarkably similar to the lifetimes measured in pump-probe experiments [78, 168]. Nakayama *et al.* concluded that the imino- and keto-tautomer decay with a sub-ps lifetime, whereas the enol-tautomer stays in the excited state for a much longer time. In a recent study, Mai et al. [181] compared the calculated excited state dynamics of

Table 5.6. Importance of individual relaxation pathways of excited keto-cytosine according to different theoretical studies.

	oop-NH_2	*semi-planar*	*C6-puckered*	others
Hudock and Martínez [175]	65%	15%	5%	15% [a]
Lan *et al.* [151]	0%	0%	100%	–
Barbatti *et al.* [170]	7%	68%	8%	17%[b]
Nakayama *et al.* [180]	4%	0%	84%	12%[a]
Mai *et al.* [181]	20%	42%	1%	37%[c]

[a] no relaxation within 1 ps simulation time
[b] no relaxation within 1.2 ps simulation time
[c] 25% populate triplet states, the remaining 12% persisted in the S_1 excited state beyond the simulation time of 1 ps

the keto- and enol-tautomer of cytosine. They found triplets states playing a significant role in the excited-state relaxation of the keto-tautomer, whereas the triplet states are less important for the enol-tautomer relaxation. There is no simulation on the excited state dynamics of hydrated cytosine, yet. QM/MM molecular dynamics simulation are difficult for cytosine because the molecule is not planar in solution and frequent switching of states occurs.

For solvated cytosine, the situation is a bit easier because the canonical keto-tautomer (C1) gains a substantial amount of energy due to solvation – more than the enol- and imino-tautomers [169]. Therefore, dynamics occurring from this tautomer is expected to dominate the signal of excited cytosine in water. Hare *et al.* have observed a bi-exponential re-population of the vibronic ground state for all pyrimidines (cytosine, thymine and uracil) [156] and explained this behaviour by a population trapping in an optically dark nπ* state. In cytosine, about 10 % of the excited molecules experience this trapping and re-populate the vibronic ground state with a rate of $(12\,\mathrm{ps})^{-1}$. In cytidine 5'-monophosphate (CMP), even 41 % of the excited molecules only re-populate the vibronic ground state with a rate of $(34\,\mathrm{ps})^{-1}$. These experimental results have triggered several theoretical investigations which have developed models for an ultra-fast population transfer from the excited ππ* state to the nπ* state [160, 162]. However, the nπ* state which is discussed to play a critical role in the excited state relaxation of pyrimidines has not yet been observed directly in experiments.

5.6.2. TRPES results

Figures 5.42 and 5.43 show the time-resolved photoelectron signal of cytosine and cytidine, respectively, solvated in water. The photoelectron spectrum extends over kinetic energies between 0 and 2.5 eV and is observed in a pump probe delay range between −0.5 and 2 ps. The signal at positive delays results from 266 nm excitation and 238 nm ionisation (at negative delays: 238 nm pump and 266 nm probe).

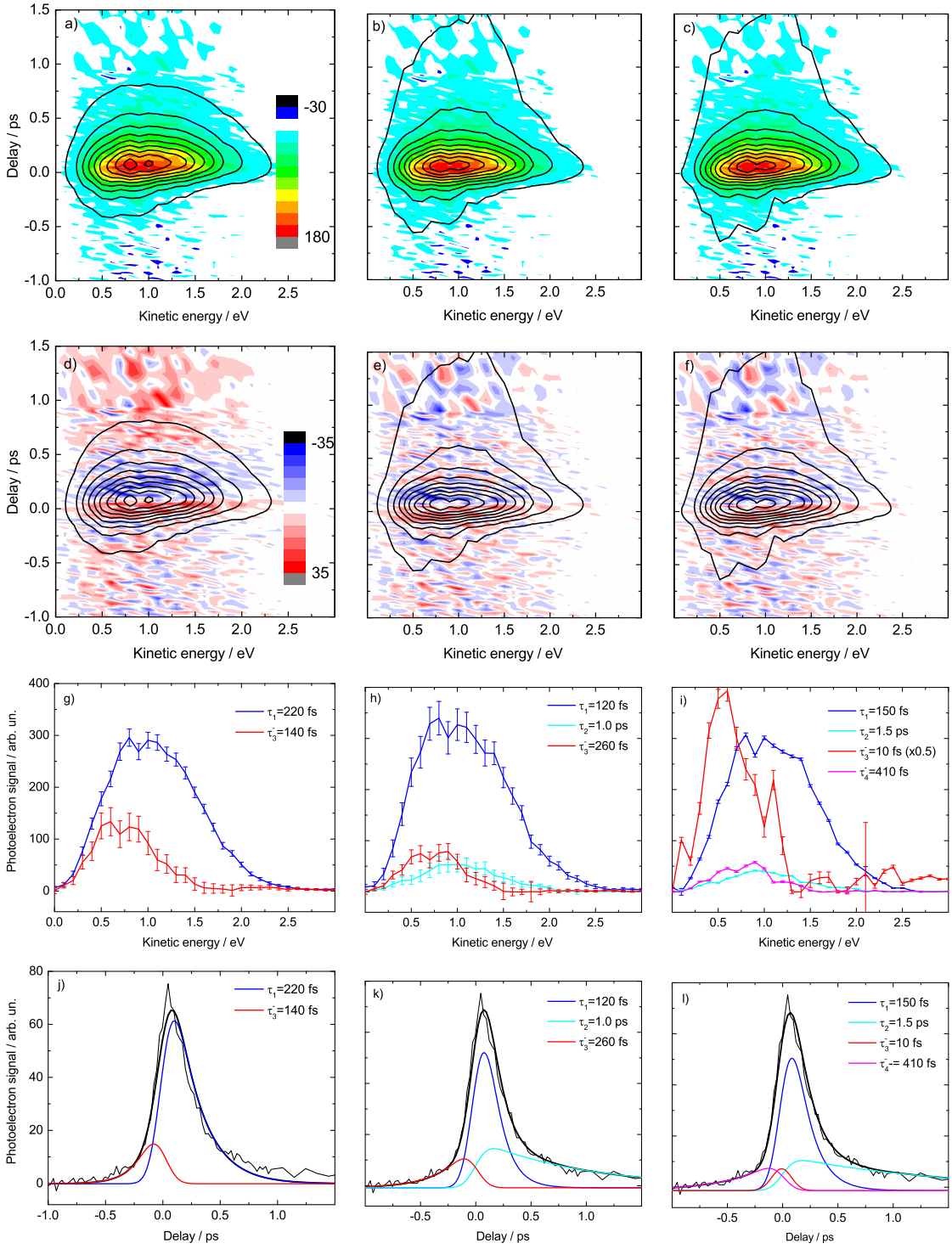

Figure 5.42. Time-resolved photoelectron spectrum of cytosine in solution obtained with 266 nm and 238 nm pulses. A global analysis including two (left column), three (center column), and four contributions (right column) was performed. a-c) Comparison of the global fit (lines) with the measured data (colour), d-f) Residuals (colour) and the global fit (lines), where the colour scale covers a range of ±15 % of the maximum photoelectron signal, g-i) Decay associated spectra of the two, three, or four contributions with error bars, j-l) Population dynamics of the individual contributions with the same colour code as in the decay associated spectra.

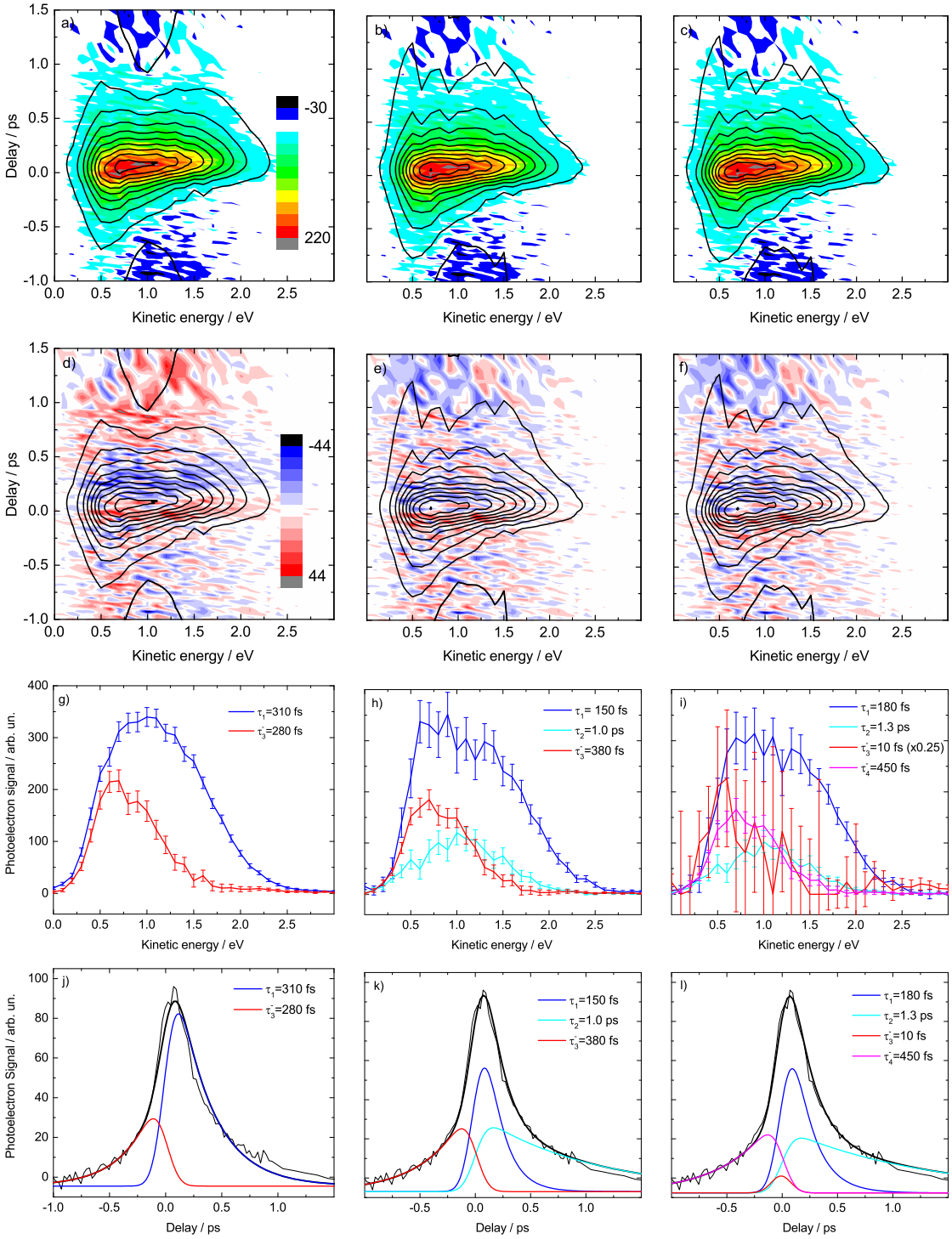

Figure 5.43. Time-resolved photoelectron spectrum of cytidine in solution obtained with 266 nm and 238 nm pulses. A global analysis including two (left column), three (center column), and four contributions (right column) was performed. a-c) Comparison of the global fit (lines) with the measured data (colour), d-f) Residuals (colour) and the global fit (lines), where the colour scale covers a range of ±15 % of the maximum photoelectron signal, g-i) Decay associated spectra of the two, three, or four contributions with error bars, j-l) Population dynamics of the individual contributions with the same colour code as in the decay associated spectra.

These data were analysed in terms of a global fit as described in the previous section on thymine (Section 5.5). The fit function includes an exponential decay convolved with a Gaussian cross-correlation for each contribution (see equation A.7 in Appendix A.1). All fit results are summarised in Table 5.7. Similar to the previous analysis of thymine (Section 5.5), the decay-associated spectra are not expected to change in time. The most simple model involves only a single contribution in each temporal direction. The result of this fit is shown in Figures 5.42(a,d,g,j) and 5.43(a,d,g,j) for cytosine and cytidine, respectively. In both cases, this fit gives reasonably good agreement but some systematic deviations are obvious. The residuals in Figures 5.42d and 5.43d are mainly positive just before time zero, negative at delays up to 0.5 ps and at later times positive, again. Therefore, an additional contribution towards positive delays was added symbolizing an alternative relaxation path (see scheme 5.9). The result of this fit with three contributions is shown in the center column (Fig. 5.42(b,e,h,k) and 5.43(b,e,h,k)). The residuals (Fig. 5.42e and 5.43e) reveal a much better agreement of the data with the fit. However, at small negative delays, the fit still underestimates the data. This has also been observed for thymine and we again explain this deviation by the failure of the exponential fit model: the wave packet needs some finite time to evolve and explore the phase space to reach the CI. Therefore, a small delay in the population decay is expected.

Figure 5.42k shows the population dynamics of the individual contributions for the three-contributions fit for cytosine. At positive delays, the main part of the excited population (90%) decays with a rate of about $(170\,\mathrm{fs})^{-1}$. The remaining 10% population decays with a rate of about $(1.4\ \mathrm{ps})^{-1}$. At negative delays, the excited state lifetime is about 230 fs. For cytidine (see Fig. 5.43k), excited state lifetimes are 160 fs and 1.1 ps for the positive delays with about 78% of the population decaying via the faster path and 370 fs for negative delays. All the fit parameters are summed up in Table 5.7. As observed for thymine/thymidine, there is no indication for a longer-lived excited state in cytosine/cytidine.

The corresponding decay associated spectra are shown in Figure 5.42h for cytosine and in Figure 5.43h for cytidine. Although the relative intensity of the spectra differs, their shape for individual contributions of the excited state dynamics of cytosine and cytidine is very similar: in positive temporal direction, the short-lived contribution has a very broad and asymmetric spectrum (possibly cut towards 0 eV) ranging up to about 2.5 eV while the more slowly decaying contribution is more symmetric and ranges only up to about 2 eV. The contribution in negative delays is again asymmetric (probably cut towards 0 eV) and ranges only up to about 1.8 eV. The similarity of the spectra and the lifetimes of excited cytosine and cytidine in solution suggests that both molecules relax on very similar pathways.

Table 5.7. Fitparameters of the global analysis of cytosine and cytidine in solution assuming n contributions to the signal and comparison with results from transient absorption (TA) and fluorescence up-conversion (FU). The lifetimes τ_1 and τ_2 refer to decays at positive delays (pump 266 nm, probe 238 nm) and the lifetimes τ_3^- and τ_4^- to decays at negative delays (pump 238 nm, probe 266 nm). The uncertainties of the lifetimes correspond to one standard deviation as obtained from the fit.

	n	τ_1 / fs	τ_2 / ps	τ_3^- / fs	τ_4^- / ps
cytosine	2 (1+1)	270	–	180	–
	2 (TA [156])[†]	0.7±0.1		–	–
	3 (2+1)	170±20	1.4±0.4	230±40	–
	2 (FU [182])	200±20	1.30±0.07	–	–
	4 (2+2)	190	1.9	10	0.29
cytidine	2 (1+1)	350	–	320	–
	1 (FU [140])	0.76±0.12		–	–
	1 (TA [122, 139])	0.72±0.40		–	–
	3 (2+1)	160±30	1.1±0.3	370±30	–
	2 (FU [182])	180±20	0.92±0.06	–	–
	4 (2+2)	210	1.4	80	430
CMP	1 (FU [140])	0.95±0.12		–	–
	1 (FU [182])	0.53±0.20		–	–
	2 (TA [156])[‡]	0.7±0.3		–	–
	2 (FU [182])	270±20	1.4±0.2	–	–

[†] additional lifetime of $\tau_{\text{long}} = (12\pm3)$ ps for re-population of the ground state

[‡] additional lifetime of $\tau_{\text{long}} = (34\pm3)$ ps for re-population of the ground state

5.6.3. Discussion

For both, cytosine and cytidine, the lifetimes obtained from the fit with three contributions are comparable to the lifetimes obtained from a bi-exponential fit to the data obtained from fluorescence up-conversion (see Table 5.7). For cytosine, we found (170±20) fs and (1.4±0.4) ps and for cytidine (160±30) fs and (1.1±0.3) ps. Hence, the short and long lifetime are identical for the two molecules. However, the results from mono-exponential fits to the TA and FU data for cytidine yield a significantly larger lifetime (∼740 fs) than a mono-exponential fit to our data (350 fs). This is probably due to the different relative amplitudes of the different contributions.

Why do we not observe any long-lived signal due to a trapping of the population in the nπ state?* There are two possible reasons for the absence of such a signal. Firstly, the nπ* state is not involved in the deactivation of the ππ* excited state and, hence, no population can be probed. Secondly, the ionisation energy of the nπ* minimum might be larger than the photon energy of the probe pulse and an existing population in the nπ* state could not be ionised.

Time-dependent photoelectron spectra of isolated cytosine have been simulated by Hudock and Martinez [175]. They observed that a significant part of the population

did not decay within 1 ps but instead was trapped in the $n_O\pi^*$ minimum (associated to the O atom). They applied 6.2 eV probe photons and observed kinetic energies of about 0.5 eV. From this, we estimate the ionisation energy of the $n\pi^*$ state at the corresponding minimum geometry of the isolated cytosine to be about 5.7 eV for the isolated molecule. In hydrated cytosine, the $n\pi^*$ state is destabilised and binding energies in water are in general lower. Therefore, the ionisation energy is expected to lower by about 1.5 eV in total (cf. Fig. 5.4). Hence, our probe photon energy of 5.2 eV should be sufficient to ionise the $n\pi^*$ state of solvated cytosine at the $n\pi^*$ potential minimum and give rise to a long-lived signal if this state is occupied. The absence of such a signal indicates that the $n\pi^*$ state of cytosine in solution is not populated during the relaxation.

Assignment of relaxation pathways. There have been numerous theoretical studies on excited state dynamics of isolated cytosine in the past [151, 170–176, 179]. These studies agree on the fact that cytosine relaxes along multiple pathways. However, differences appear in the relative importance of individual pathways. The influence of hydration on the relaxation has been studied regarding only two specific pathways that appear in isolated cytosine [183, 184]. These pathways towards the *oop-*NH_2 CI and the *C6-puckered* CI remained equally accessible. There was no clear preference of one over the other pathways. Since, even for isolated cytosine, the assignment of relaxation pathways to measured excited state lifetimes remains controversially, we cannot provide a clear assignment of decay channels in solution, yet.

However, an intriguing similarity to the thymine case might be pointed out. Nakayama *et al.* have recently found two different relaxation pathways on the $\pi\pi^*$ potential energy surface for hydrated thymine [153]: the first involving a CI with a pronounced out-of-plane motion of the NH_2 group, the second involving a CI with an out-of-plane motion of the *O*8 atom (cf. Fig. 5.35). These geometries show very similar features as the geometries at the *oop-*NH_2 CI and the *oop-O* CI of cytosine. The latter is very high in potential energy for isolated thymine and therefore is not involved in excited state relaxation in the gas phase. However, this pathway is strongly stabilised upon hydration and hence becomes relevant. We may speculate that hydration influences the relaxation pathways in cytosine similarly. But here, further sophisticated theoretical work on cytosine in solution is required. We expect that this work presents benchmark data and will trigger new theory work to better understand the relaxation dynamics in hydrated DNA bases.

6. Conclusions and Outlook

In this work, I have investigated the solvated electron and the excited state dynamics of DNA bases and nucleosides in solution by means of time-resolved photoelectron spectroscopy.

The solvated electron is the – seemingly – most simple species in solution. We have generated solvated electron by a charge-transfer-to-solvent excitation of iodide anions in aqueous solution and have observed a temporal evolution as expected from transient absorption experiments: Initially, the newly formed excess electrons are located in a non-relaxed solvent environment, i. e. water molecules need to re-orient around the new charge distribution in order to stabilise it. This leads to a time-dependent shift of the photoelectron band. The solvated electron is initially located in close proximity to the geminate iodine radial, and recombination competes with the formation of free solvated electrons. Again in agreement with existing literature, we have observed a geminate recombination rate of $(22\,\mathrm{ps})^{-1}$ and a rate for formation of free solvated electrons of about $(60\,\mathrm{ps})^{-1}$.

However, in addition to existing literature, we have also obtained surprising new results: Some of the excess charges are apparently generated already in relaxed solvent environment – their binding energy is already initially large. We also observed an additional sub-ps decay of solvated electron signal. Based on the surface sensitivity of liquid jet photoelectron spectroscopy and supported by our data obtained from surface active tetrabutyl ammonium iodide measurements, we proposed a new interpretation of the data: There are two sub-populations of solvated electrons contributing to the signal: surface and bulk solvated electrons. Bulk solvated electrons thermalise in about 1 ps and then either recombine with the geminate iodide radical with a rate of $(22\,\mathrm{ps})^{-1}$ or diffuse away from the iodine radical surviving for up to µs. Solvated electrons close to the surface are generated already with a binding energy characteristic for thermalised solvated electrons and recombine on a sub-ps timescale. Both species have the same binding energy of 3.4 eV. No indication for a long-lived contribution with a binding energy of 1.6 eV has been observed.

I presented the first photoelectron spectra of neutral DNA bases and nucleosides in aqueous solution (guanine excluded due to its poor solubility in water). I found a common feature in the two-photon ionisation signals (one-colour signals): the spectra

are in general down-shifted in electron kinetic energy. This observation was interpreted in terms of excited-state dynamics occurring within the pulse duration.

For adenine, the most theoretical and experimental work was available, and we chose this molecule for a proof of principle experiment. We distinguished the two tautomers that are present in solution and assigned the excited state lifetimes according to the literature. The time-dependent photoelectron spectra of these two tautomers are almost identical and reveal an excited state binding energy of about 4 eV. But the relative signal intensity of the two tautomers depends on the probe wavelength, i.e. their excited-state ionisation cross-sections have a different wavelength dependence.

In the case of guanosine, previous experiments with transient absorption and fluorescence up-conversion have given similar excited state lifetimes of 200 fs, 1 ps and 2.5 ps. But these lifetimes were assigned differently. While in transient absorption experiments, the first two lifetimes were assigned to dynamics on the excited ππ* state and the largest lifetime was assigned to hot-ground-state relaxation, fluorescence up-conversion experiments indicated that all lifetimes had to be assigned to excited state dynamics and the excited state potential was suggested to be very flat. In our experiment using time-resolved photoelectron spectroscopy, we found comparable lifetimes of about 300 fs and 2 ps. Since we cannot ionise the ground state (even if hot), we follow the latter assignment: a sequential transition out of the Franck-Condon region and a subsequent population transfer through the conical intersection into the ground state. With the higher excitation energy at negative delays, the relaxation lifetimes are decreased in agreement with the higher excess energy accelerating the excited state dynamics and also opening further relaxation pathways. The fact that the spectra are almost identical at positive and negative delays suggests that vibrational energy in the excited state is preserved.

Regarding the solvated pyrimidine bases (thymine and cytosine) and nucleosides (thymidine and cytidine), our data challenged the previously accepted relaxation pathway *via* the nπ* state. In transient absorption experiments, an excited state de-population of <1 ps was found and assigned to the relaxation of the ππ* state. Additionally, the re-population of the vibronic ground state occurred within several ten ps. This was explained by an involvement of a dark nπ* state. In photoelectron spectroscopy, also nπ* states are directly observable if the photon energy is sufficiently high for ionisation. Our time-resolved photoelectron spectra show no signal from an nπ* state although it is energetically accessible with the probe photon energy and should be easily observable at delay times >1 ps. In case of thymine/thymidine, our data instead is in agreement with the previously proposed relaxation along two different reaction coordinates on the same ππ* potential energy surface. For cytosine/cytidine, we observed a very similar behaviour as for thymine/thymidine, however the corresponding QM/MM molecular

dynamics simulations are not available, yet. We suppose that also cytosine and cytidine relax along two coordinates on the $\pi\pi^*$ potential surface.

In this work, I have shown that time-resolved photoelectron spectroscopy is a powerful tool to investigate solvated molecules in a liquid jet. This technique provides a different view on the excited state dynamics of solvated molecules complementing established techniques as transient absorption or fluorescence up-conversion.

Only short time after the very first works on time-resolved photoelectron spectroscopy in solution were published in 2010, this technique has raised a lot of interest and several groups are now implementing set-ups to join this research area. Most of these groups aim at using high harmonics for the benefit of a larger Franck-Condon window for ionisation. But they sacrifice the advantage of almost background-free measurements because every molecule will be ionised by a single photon – whether solute or solvent, whether in the ground or excited state. A very simple estimation demonstrates the obstacles: To minimise solute-solute interactions, diluted solutions of up to 1 mM concentration are preferred. Aqueous solutions always contain 55 M water molecules. Moreover, typically excitation densities of about 10% are used to avoid non-linear effects. Hence, only from considering the concentrations and excitation density, a signal-to-noise ratio of about $2 \cdot 10^{-6}$ at maximum is expected. At the same time, the pulse energies have to be decreased drastically in order to create only a few (meaning 1–10) photoelectrons per pulse, otherwise space charge effects disturb the spectrum. Hence, there are some technical challenges to be overcome prior to performing successful experiments on diluted solutions using high harmonic radiation. One possibility is obviously to significantly increase the repetition rate of the laser.

The time-resolved photoelectron spectroscopy of liquid samples as it is presented in this work is a great tool which has provided new insights in the dynamics and energetics of the solvated electron and the excited-state dynamics of DNA bases and nucleosides – although these species were already extensively studied with other techniques and reasonably well understood.

The photostability of DNA bases is not yet understood completely but it is surely based on the ultrafast dynamics that bring the molecule back into the ground state. We have shown, that the dynamics starts already within the pulse duration and that the process initiating these dynamics could not be resolved, yet. It would be very interesting to do the same experiment with even shorter pulses in order to resolve the initial steps.

A. Appendix

A.1. Fitfunction for the time-dependent signal

The cross-correlation of the laser pulses is assumed to be of Gaussian shape. Therefore, a normalized Gaussian $G(t)$ is used where w is its width (twice the standard deviation):

$$G(t) = \frac{1}{w\sqrt{\pi/2}} \cdot \exp\left(-\frac{2t^2}{w^2}\right). \tag{A.1}$$

The full width at half maximum of the cross-correlation is then given by FWHM= $w \cdot \sqrt{\ln(4)}$. (For the convolution with the exponential, this Gaussian runs over the whole time axis. Therefore, it is not shifted to t_0 which is the temporal overlap of pump and probe pulses.)

The lifetime of the excited state i is given by an exponential decay function $E_i(t)$, where k_i is the decay rate of the excited state with corresponding lifetime of $\tau_i = k_i^{-1}$ and A_i is the amplitude of this contribution at t_0:

$$E_i(t) = A_i \cdot \exp(-k_i \cdot (t - t_0)). \tag{A.2}$$

The time-dependent signal is then the convolution of the Gaussian cross-correlation and the exponential decrease $E(t)$ (the exponential has to be 0 for delay times $< t_0$ and is therefore multiplied with a step-function centred at t_0):

$$\text{Popdyn}(t) = G(t) \otimes E(t) = \frac{1}{2} A_i \cdot \exp\left(\frac{k_i^2 w^2}{8} - k_i(t - t_0)\right) \cdot \text{Erfc}\left(\frac{k_i w^2 - 4(t - t_0)}{2w\sqrt{2}}\right). \tag{A.3}$$

Parallel decays: If several transients (all initiated instantaneously by the pump pulse) contribute to the signal, then individual population dynamics are summed up:

$$\text{Signal}(t) = \sum_i A_i \cdot \frac{1}{2} \exp\left(\frac{k_i^2 w^2}{8} - k_i(t - t_0)\right) \cdot \text{Erfc}\left(\frac{k_i w^2 - 4(t - t_0)}{2w\sqrt{2}}\right), \tag{A.4}$$

where A_i is the amplitude of the individual component at the time $t = t_0$.

Sequential decays: In case of sequential decays, only the transient A is populated by the pump pulse and decays with the rate k_A by forming transient B which rises with the

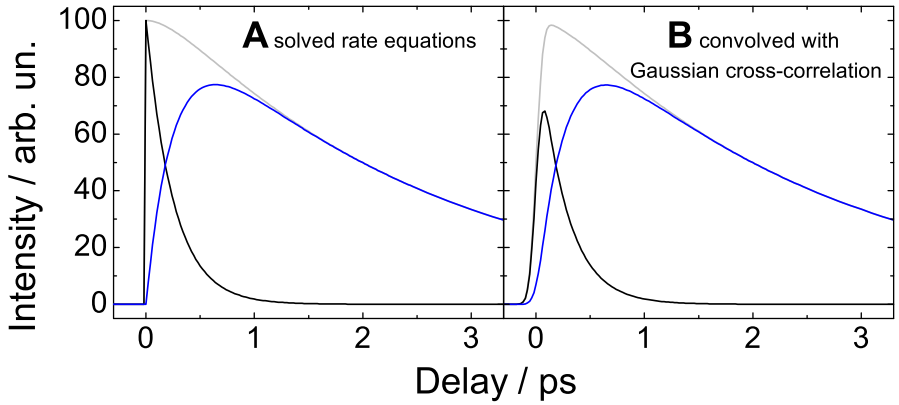

Figure A.1. The solutions of the rate equations for two transients with lifetimes of 250 fs and 2.5 ps in a sequential model with complete population transfer ($\alpha = 1$) are shown in A. B shows the same equations convolved with the Gaussian cross-correlation (FWHM = 117 fs).

same time constant. In this case, the rate equations have to be solved, where N_A and N_B reflect the number of molecules in the corresponding excited states:

$$\begin{array}{ll} \frac{\mathrm{d}N_\mathrm{A}(t)}{\mathrm{d}t} & = -k_\mathrm{A} \cdot N_\mathrm{A}(t) \\ \frac{\mathrm{d}N_\mathrm{B}(t)}{\mathrm{d}t} & = -k_\mathrm{B} \cdot N_\mathrm{B}(t) + k_\mathrm{A} \cdot N_\mathrm{A}(t) \end{array} \quad \Rightarrow \quad \begin{array}{ll} N_\mathrm{A}(t) & = A_0 \cdot \mathrm{e}^{-k_\mathrm{A} t} \\ N_\mathrm{B}(t) & = \frac{A_0 \cdot k_\mathrm{A}}{k_\mathrm{A} - k_\mathrm{B}} (\mathrm{e}^{-k_\mathrm{A} t} - \mathrm{e}^{-k_\mathrm{B} t}) \end{array} \quad , \tag{A.5}$$

where A_0 is the initial population of transient A at t_0. If now also these functions are convolved with the same Gaussian cross-correlation function $G(t)$, the Population dynamics for transient B changes to (the population dynamics for transient A is of course the same as for the parallel pathways):

$$\begin{aligned} \mathrm{Popdyn_B}(t) = \alpha \cdot \frac{A_0 \cdot k_A}{k_A - k_B} \cdot \frac{1}{2} \Bigg(& \exp\left(\frac{k_B^2 w^2}{8} - k_B (t - t_0) \right) \cdot \mathrm{Erfc}\left(\frac{k_B w^2 - 4(t - t_0)}{2w\sqrt{2}} \right) \\ & - \exp\left(\frac{k_A^2 w^2}{8} - k_A (t - t_0) \right) \cdot \mathrm{Erfc}\left(\frac{k_A w^2 - 4(t - t_0)}{2w\sqrt{2}} \right) \Bigg), \end{aligned} \tag{A.6}$$

where α corresponds to the relative cross-section of transient B as compared to transient A. If all population is transferred from A to B and they have equal ionization cross-sections then $\alpha = 1$. This is illustrated in Figure A.1 showing the solutions of the rate equations (A) and the convolutions with the cross-correlation function (B).

For the experiments with DNA bases and nucleotides, the photon energies were chosen such that both pump and probe pulse can initiate dynamics. Therefore, also signal into negative temporal direction (where the probe pulse pumps) is expected. In the corresponding equation for population dynamics, only the sign in front of the term $(t - t_0)$ in the argument of the exponential and in the argument of the error function

changes.

Two-dimensional fit of signal from DNA bases: For the two-dimensional fit of the photoelectron signal, the amplitudes A_i are replaced by energy-dependent amplitudes $a_i(E)$ for each energy point which are introduced as fit-parameters. Hence, the $a_i(E)$ is the decay-associated spectrum of the contribution i. An additional time-independent contribution $a_{\text{offset}}(E)$ is added due to the dead time effects of the detector.

$$\text{Signal}(E,t) = a_{\text{offset}}(E) + \sum_i a_i(E) \cdot \frac{1}{2}\exp\left(\frac{k_i^2 w^2}{8} - k_i(t-t_0)\right) \cdot \text{Erfc}\left(\frac{k_i w^2 - 4(t-t_0)}{2w\sqrt{2}}\right), \tag{A.7}$$

This is the case of parallel pathways but it is also easily adaptable to the sequential pathways.

A.2. Excitation and ionization energies of the DNA bases

Table A.1 lists values and references for the vertical excitation and ionization energies of the DNA bases in gas phase (absolute calculated values) and aqueous solution (solvatochromic shifts compared to the isolated molecule).

Table A.1. Vertical excitation energies (Franck-Condon region) of the DNA bases in the gas phase and in aqueous solution. For adenine in solution, Lan *et al.* found strongly mixed characters in the first three excited states [83].

molecule	state	vertical excitation energy / eV	Ref.
adenine (gas)	$n\pi^*$	4.58	[185]
	$\pi\pi^*$ (L_a)	5.16(exp), 4.66(theo)	[186], [185]
	$\pi\pi^*$ (L_b)	within 0.2 around L_a, 4.97	[116], [185]
	IP	8.5	[187]
adenine (aq)	L_a	-0.1–0.3	[188]
	L_b	-0.1–0.2	[188]
	$n\pi^*$	+0.2–0.5	[188]
	IP	7.5 eV	[80]
guanine (gas)	L_a ($\pi\pi^*$)	4.26	[135]
	L_b ($\pi\pi^*$)	4.99	[135]
	$n\pi^*$	5.33	[135]
	IP	8.24	[189]
guanine (aq)	L_a ($\pi\pi^*$)	-(0.1–0.3)	[188]
	L_b ($\pi\pi^*$)	$\sim$	[188]
	$n\pi^*$ (dark)	+0.5	[188]
	IP	7.2 eV	[80]
thymine (gas)	$n\pi^*$	4.54	[151]
	$\pi\pi^*$	4.90	[151]
	IP	9.15	[190]
thymine (aq)	$\pi\pi^*$	-0.1–0.2	[188]
	$n\pi^*$	+0.5	[188]
	IP	8.1 eV	[80]
cytosine (gas)	$\pi\pi^*$	4.30	[151]
	$n\pi^*$	4.68	[151]
	IP	8.8 eV	[78, Ref. 12]
cytosine (aq)	$\pi\pi^*$	+0.2	[188]
	$n\pi^*$	+0.6	[188]
	IP	7.8 eV	[80]

Bibliography

[1] A. H. Zewail. Femtochemistry: Atomic-Scale Dynamics of the Chemical Bond. *J. Phys. Chem. A*, 104:5660, 2000.

[2] C. E. Crespo-Hernández, B. Cohen, P. M. Hare, and B. Kohler. Ultrafast Excited-State Dynamics in Nucleic Acids. *Chem. Rev.*, 104(4):1977–2020, 2004.

[3] H. Haken and H. C. Wolf. *Atom- und Quantenphysik: Einführung in die experimentellen und theoretischen Grundlagen ; mit 32 Tabellen, 177 Aufgaben und vollständigen Lösungen.* Springer-Lehrbuch. Springer, Berlin [u.a.], 8 edition, 2004 [erschienen] 2003.

[4] S. Lochbrunner, J. J. Larsen, J. P. Shaffer, M. Schmitt, T. Schultz, J. G. Underwood, and A. Stolow. Methods and applications of femtosecond time-resolved photoelectron spectroscopy. *J. Electron Spectrosc. Relat. Phenom.*, 112(1-3):183–198, 2000.

[5] A. Stolow, A. E. Bragg, and D. M. Neumark. Femtosecond Time-Resolved Photoelectron Spectroscopy. *Chem. Rev.*, 104(4):1719–1758, 2004.

[6] I. V. Hertel and W. Radloff. Ultrafast dynamics in isolated molecules and molecular clusters. *Rep. Prog. Phys.*, 69:1897, 2006.

[7] M. Weinelt. Time-resolved two-photon photoemission from metal surfaces. *J. Phys.: Condens. Matter*, 14(43):R1099–R1141, 2002.

[8] V. P. Zhukov and E. V. Chulkov. The femtosecond dynamics of electrons in metals. *Physics-Uspekhi*, 52(2):105–136, 2009.

[9] H. Siegbahn and K. Siegbahn. ESCA applied to liquids. *J. Electron Spectrosc. Relat. Phenom.*, 2(3):319–325, 1973.

[10] M. Faubel and B. Steiner. Strong Bipolar Electrokinetic Charging of Thin Liquid Jets Emerging from 10 µm PtIr Nozzles. *Ber. Bunsenges. Phys. Chem.*, 96:1167, 1992.

[11] M. Faubel, B. Steiner, and J. P. Toennies. Photoelectron spectroscopy of liquid water, some alcohols, and pure nonane in free micro jets. *J. Chem. Phys.*, 106:9013, 1997.

[12] B. Winter and M. Faubel. Photoemission from Liquid Aqueous Solutions. *Chem. Rev.*, 106(4):1176–1211, 2006.

[13] Y. Itikawa and N. Mason. Cross Sections for Electron Collisions with Water Molecules. *J. Phys. Chem. Ref. Data*, 34(1):1, 2005.

[14] M. Faubel, B. Steiner, and J. P. Toennies. Measurement of HeI photoelectron spectra of liquid water, formamide and ethylene glycol in fast-flowing microjets. *J. Electron Spectrosc. Relat. Phenom.*, 95(2-3):159–169, 1998.

[15] F. Buchner, A. Lübcke, N. Heine, and T. Schultz. Time-resolved photoelectron spectroscopy of liquids. *Rev. Sci. Instrum.*, 81(11):113107, 2010.

[16] B. Winter, R. Weber, W. Widdra, M. Dittmar, M. Faubel, and I. V. Hertel. Full Valence

Band Photoemission from Liquid Water Using EUV Synchrotron Radiation. *J. Phys. Chem. A*, 108(14):2625–2632, 2004.

[17] K. R. Siefermann, Y. Liu, E. Lugovoy, O. Link, M. Faubel, U. Buck, B. Winter, and B. Abel. Binding energies, lifetimes and implications of bulk and interface solvated electrons in water. *Nat. Chem.*, 2(4):274–279, 2010.

[18] B. Winter. Liquid microjet for photoelectron spectroscopy. *Nucl. Instr. Meth. Phys. Res. A*, 601(1-2):139–150, 2009.

[19] I. Plante and F. A. Cucinotta. Cross sections for the interactions of 1 eV–100 MeV electrons in liquid water and application to Monte-Carlo simulation of HZE radiation tracks. *New J. Phys.*, 11(6):063047, 2009.

[20] M. Michaud, A. Wen, and L. Sanche. Cross Sections for Low-Energy (1–100 eV) Electron Elastic and Inelastic Scattering in Amorphous Ice. *Radiat. Res.*, 159(1):3–22, 2003.

[21] F. Buchner, T. Schultz, and A. Lübcke. Solvated electrons at the water–air interface: surface versus bulk signal in low kinetic energy photoelectron spectroscopy. *Phys. Chem. Chem. Phys.*, 14(16):5837, 2012.

[22] B. Winter, R. Weber, P. M. Schmidt, I. V. Hertel, M. Faubel, L. Vrbka, and P. Jungwirth. Molecular Structure of Surface-Active Salt Solutions: Photoelectron Spectroscopy and Molecular Dynamics Simulations of Aqueous Tetrabutylammonium Iodide. *J. Phys. Chem. B*, 108(38):14558–14564, 2004.

[23] P. Jungwirth and D. J. Tobias. Ions at the Air/Water Interface. *J. Phys. Chem. B*, 106(25):6361–6373, 2002.

[24] N. Ottosson, M. Faubel, S. E. Bradforth, P. Jungwirth, and B. Winter. Photoelectron spectroscopy of liquid water and aqueous solution: Electron effective attenuation length and emission-angle anisotropy. *J. Electron Spectrosc. Relat. Phenom.*, 177:60, 2010.

[25] S. Thürmer, R. Seidel, M. Faubel, W. Eberhardt, J. C. Hemminger, S. E. Bradforth, and B. Winter. Photoelectron Angular Distributions from Liquid Water: Effects of Electron Scattering. *Phys. Rev. Lett.*, 111(17):173005, 2013.

[26] Y.-I Suzuki, K. Nishizawa, N. Kurahashi, and T. Suzuki. Effective attenuation length of an electron in liquid water between 10 and 600 eV. *Phys. Rev. E*, 90:010302, 2014.

[27] W. L. Holstein, L. J. Hayes, E. M. C. Robinson, G. S. Laurence, and M. A. Buntine. Aspects of Electrokinetic Charging in Liquid Microjets. *J. Phys. Chem. B*, 103:3035, 1999.

[28] S. Ong, X. Zhao, and K. B. Eisenthal. Polarization of water molecules at a charged interface: second harmonic studies of the silica/water interface. *Chem. Phys. Lett.*, 191(3-4):327–335, 1992.

[29] J. P. O'Reilly, C. P. Butts, I. A. I'Anso, and A. M. Shaw. Interfacial pH at an Isolated Silica−Water Surface. *J. Am. Chem. Soc.*, 127(6):1632–1633, 2005.

[30] P. M. Dove and C. M. Craven. Surface charge density on silica in alkali and alkaline earth chloride electrolyte solutions. *Geochim. Cosmochim. Acta*, 69(21):4963–4970, 2005.

[31] C. H. Hamann and W. Vielstich. *Electrochemistry*. Wiley-VCH, 1998.

[32] R. Weber, B. Winter, P. M. Schmidt, W. Widdra, I. V. Hertel, M. Dittmar, and M. Faubel.

Photoemission from aqueous alkali-metal - iodide salt solutions using EUV synchrotron radiation. *J. Phys. Chem.*, 108:4729, 2004.

[33] N. Ottosson, J. Heyda, E. Wernersson, W. Pokapanich, S. Svensson, B. Winter, G. Öhrwall, P. Jungwirth, and O. Björneholm. The influence of concentration on the molecular surface structure of simple and mixed aqueous electrolytes. *Phys. Chem. Chem. Phys.*, 12:10693, 2010.

[34] M. A. Brown, B. Winter, M. Faubel, and J. C. Hemminger. Spatial Distribution of Nitrate and Nitrite Anions at the Liquid/Vapor Interface of Aqueous Solutions. *J. Am. Chem. Soc.*, 131(24):8354–8355, 2009.

[35] Y. Tang, Suzuki Y.-I., H. Shen, K. Sekiguchi, N. Kurahashi, K. Nishizawa, P. Zuo, and T. Suzuki. Time-resolved photoelectron spectroscopy of bulk liquids at ultra-low kinetic energy. *Chem. Phys. Lett.*, 494(1-3):111–116, 2010.

[36] A. T. Shreve, T. A. Yen, and D. M. Neumark. Photoelectron spectroscopy of hydrated electrons. *Chem. Phys. Lett.*, 493(4-6):216–219, 2010.

[37] N. Preissler, F. Buchner, T. Schultz, and A. Lübcke. Electrokinetic charging and evidence for charge evaporation in liquid microjets of aqueous salt solution. *J. Phys. Chem. B*, 117:2422, 2013.

[38] P. Kruit and F. H. Read. Magnetic field paralleliser for 2π electron-spectrometer and electron-image magnifier. *J. Phys. E: Sci. Instrum.*, 16(4):313–324, 1983.

[39] J. L. Wiza. Microchannel plate detectors. *Nuclear Instruments and Methods*, 162(1-3):587–601, 1979.

[40] G. K. Jarvis, M. Evans, C. Y. Ng, and K. Mitsuke. Rotational-resolved pulsed field ionization photoelectron study of $NO^+(X^1\Sigma^+, v^+=0–32)$ in the energy range of 9.24–16.80 eV. *J. Chem. Phys.*, 111(7):3058, 1999.

[41] E. J. Hart and J. W. Boag. Absorption Spectrum of the Hydrated Electron in Water and in Aqueous Solutions. *J. Am. Chem. Soc.*, 84(21):4090–4095, 1962.

[42] W. Weyl. Ueber Metallammonium-Verbindungen. *Annalen der Physik und Chemie*, 197(4):601–612, 1864.

[43] J. A. Kloepfer, V. H. Vilchiz, V. A. Lenchenkov, A. C. Germaine, and S. E. Bradforth. The ejection distribution of solvated electrons generated by the one-photon photodetachment of aqueous I^- and two-photon ionization of the solvent. *J. Chem. Phys.*, 113:6288, 2000.

[44] R. Laenen, T. Roth, and A. Laubereau. Novel Precursors of Solvated Electrons in Water: Evidence for a Charge Transfer Process. *Phys. Rev. Lett.*, 85(1):50–53, 2000.

[45] J. A. Kloepfer, V. H. Vilchiz, V. A. Lenchenkov, A. C. Germaine, and S. E. Bradforth. Femtosecond dynamics of photodetachment of the iodide anion in solution: resonant excitation into the charge-transfer-to-solvent state. *Chem. Phys. Lett.*, 298(1-3):120–128, 1998.

[46] H. Iglev, A. Trifonov, A. Thaller, I. Buchvarov, T. Fiebig, and A. Laubereau. Photoionization dynamics of an aqueous iodide solution: the temperature dependence. *Chem. Phys. Lett.*, 403:198, 2005.

[47] M. Assel, R. Laenen, and A. Laubereau. Ultrafast electron trapping in an aqueous NaCl-

solution. *Chem. Phys. Lett.*, 289(3-4):267–274, 1998.

[48] R. A. Crowell, R. Lian, I. A. Shkrob, D. M. Bartels, X. Chen, and S. E. Bradforth. Ultrafast dynamics for electron photodetachment from aqueous hydroxide. *J. Chem. Phys.*, 120(24):11712, 2004.

[49] J. A. Kloepfer, V. H. Vilchiz, V. A. Lenchenkov, X. Chen, and S. E. Bradforth. Time-resolved scavenging and recombination dynamics from I:e^- caged pairs. *J. Chem. Phys.*, 117:766, 2002.

[50] W. S Sheu and P. J. Rossky. Dynamics of electron detachment from an aqueous halide ion. *Chem. Phys. Lett.*, 213:233, 1993.

[51] Y. Tang, H. Shen, K. Sekiguchi, N. Kurahashi, T. Mizuno, Suzuki Y.-I., and T. Suzuki. Direct measurement of vertical binding energy of a hydrated electron. *Phys. Chem. Chem. Phys.*, 12(15):3653, 2010.

[52] A. Lübcke, F. Buchner, N. Heine, I. V. Hertel, and T. Schultz. Time-resolved photoelectron spectroscopy of solvated electrons in aqueous NaI solution. *Phys. Chem. Chem. Phys.*, 12(43):14629, 2010.

[53] I. V. Hertel, C. Hüglin, C. Nitsch, and C. P. Schulz. Photoionization of $Na(NH_3)_n$ and $Na(H_2O)_n$ clusters: a step towards the liquid phase? *Phys. Rev. Lett.*, 67:1767, 1991.

[54] L. Lehr, M. T. Zanni, C. Frischkorn, R. Weinkauf, and D. M. Neumark. Electron Solvation in Finite Systems: Femtosecond Dynamics of Iodide(Water)$_n$ anion clusters. *Science*, 284:635, 1999.

[55] A. E. Bragg, J. R. R. Verlet, A. Kammrath, O. Cheshnovsky, and D. M. Neumark. Hydrated electron dynamics: From clusters to bulk. *Science*, 306:669, 2004.

[56] J. R. R. Verlet, A. E. Bragg, A. Kammrath, O. Cheshnovsky, and D. M. Neumark. Observation of Large Water-Cluster Anions with Surface-Bound Excess Electrons. *Science*, 307:93, 2005.

[57] J. V. Coe, G. H. Lee, J. G. Eaton, S. T. Arnold, H. W. Sarkas, K. H. Bowen, C. Ludewigt, H. Haberland, and D. R. Worsnop. Photoelectron spectroscopy of hydrated electron cluster anions, $(H_2O)^-_{n=2-69}$. *J. Chem. Phys.*, 92(6):3980, 1990.

[58] L. Ma, K. Majer, F. Chirot, and B. von Issendorff. Low temperature photoelectron spectra of water cluster anions. *J. Chem. Phys.*, 131(14):144303, 2009.

[59] J. Kim, I. Becker, O. Cheshnovsky, and M. A. Johnson. Photoelectron spectroscopy of the 'missing' hydrated electron clusters (H2O)−n, n=3, 5, 8 and 9: Isomers and continuity with the dominant clusters n=6, 7 and âl"11. *Chem. Phys. Lett.*, 297(1-2):90–96, 1998.

[60] D. M. Neumark. Spectroscopy and dynamics of excess electrons in clusters. *Mol. Phys.*, 106(16-18):2183–2197, 2008.

[61] R. E. Larsen, W. J. Glover, and B. J. Schwartz. Does the Hydrated Electron Occupy a Cavity? *Science*, 329(5987):65–69, 2010.

[62] L. Turi and A. Madarasz. Comment on "Does the Hydrated Electron Occupy a Cavity?". *Science*, 331(6023):1387, 2011.

[63] L. D. Jacobson and J. M. Herbert. Comment on "Does the Hydrated Electron Occupy a

Cavity?". *Science*, 331(6023):1387, 2011.

[64] R. E. Larsen, W. J. Glover, and B. J. Schwartz. Response to Comments on "Does the Hydrated Electron Occupy a Cavity?". *Science*, 331(6023):1387, 2011.

[65] F. Uhlig, O. Marsalek, and P. Jungwirth. Unraveling the Complex Nature of the Hydrated Electron. *J. Phys. Chem. Lett.*, 3(20):3071–3075, 2012.

[66] J. R. Casey, A. Kahros, and B. J. Schwartz. To Be or Not to Be in a Cavity: The Hydrated Electron Dilemma. *J. Phys. Chem. B*, 117(46):14173–14182, 2013.

[67] M. F. Fox and E. Hayon. Far ultraviolet solution spectroscopy of the iodide ion. *J. Chem. Soc., Faraday Trans.*, 73(0):1003, 1977.

[68] X. Chen and S. E. Bradforth. The Ultrafast Dynamics of Photodetachment. *Annu. Rev. Phys. Chem.*, 59(1):203–231, 2008.

[69] R. S. Berry, C. W. Reimann, and G. N. Spokes. Absorption Spectra of Gaseous Halide Ions and Halogen Electron Affinities: Chlorine, Bromine, and Iodine. *J. Chem. Phys.*, 37(10):2278, 1962.

[70] B. J. Schwartz and P. J. Rossky. Pump-probe spectroscopy of the hydrated electron: A quantum molecular dynamics simulation. *J. Chem. Phys.*, 101:6917, 1994.

[71] Y.-I Yamamoto, Y.-I Suzuki, G. Tomasello, T. Horio, S. Karashima, R. Mitrić, and T. Suzuki. Time- and Angle-Resolved Photoemission Spectroscopy of Hydrated Electrons Near a Liquid Water Surface. *Phys. Rev. Lett.*, 112(18), 2014.

[72] F. Uhlig, O. Marsalek, and P. Jungwirth. Electron at the Surface of Water: Dehydrated or Not? *J. Phys. Chem. Lett.*, 4(2):338–343, 2013.

[73] Suzuki Y.-I., H. Shen, Y. Tang, N. Kurahashi, K. Sekiguchi, T. Mizuno, and T. Suzuki. Isotope effect on ultrafast charge-transfer-to-solvent reaction from I− to water in aqueous NaI solution. *Chemical Science*, 2(6):1094, 2011.

[74] F. Messina, O. Bräm, A. Cannizzo, and M. Chergui. Real-time observation of the charge transfer to solvent dynamics. *Nat. Commun.*, 4:2119(1–6), 2013.

[75] E. R. Bittner. Exciton dynamics: Simplifying organic complexity. *Nat. Phys.*, 2(9):591–592, 2006.

[76] E. R. Bittner. Lattice theory of ultrafast excitonic and charge-transfer dynamics in DNA. *J. Chem. Phys.*, 125(9):094909, 2006.

[77] T. M. Nordlund. Sequence, Structure and Energy Transfer in DNA. *Photochem. Photobiol.*, 83(3):625–636, 2007.

[78] K. Kosma, C. Schröter, E. Samoylova, I. V. Hertel, and T. Schultz. Excited-State Dynamics of Cytosine Tautomers. *J. Am. Chem. Soc.*, 131(46):16939–16943, 2009.

[79] F. Buchner, H.-H. Ritze, J. Lahl, and A. Lübcke. Time-resolved photoelectron spectroscopy of adenine and adenosine in aqueous solution. *Phys. Chem. Chem. Phys.*, 15(27):11402, 2013.

[80] R. Seidel. *Electronic-structure interactions in aqueous solutions: a liquid-jet photoelectron-spectroscopy study.* PhD thesis, Technische Universitaet Berlin, Berlin, 2011.

[81] E. Pluhařová, P. Jungwirth, S. E. Bradforth, and P. Slavíček. Ionization of Purine Tau-

tomers in Nucleobases, Nucleosides, and Nucleotides: From the Gas Phase to the Aqueous Environment. *J. Phys. Chem. B*, 115(5):1294–1305, 2011.

[82] P. Slavíček, B. Winter, M. Faubel, S. E. Bradforth, and P. Jungwirth. Ionization Energies of Aqueous Nucleic Acids: Photoelectron Spectroscopy of Pyrimidine Nucleosides and ab Initio Calculations. *J. Am. Chem. Soc.*, 131(18):6460–6467, 2009.

[83] Z. Lan, Y. Lu, E. Fabiano, and W. Thiel. QM/MM Nonadiabatic Decay Dynamics of 9H-Adenine in Aqueous Solution. *ChemPhysChem*, 12(10):1989–1998, 2011.

[84] F.-A. Miannay, T. Gustavsson, A. Banyasz, and D. Markovitsi. Excited-State Dynamics of dGMP Measured by Steady-State and Femtosecond Fluorescence Spectroscopy. *J. Phys. Chem. A*, 114(9):3256–3263, 2010.

[85] V. A. Ovchinnikov and D. Sundholm. Coupled-cluster and density functional theory studies of the electronic 0–0 transitions of the DNA bases. *Phys. Chem. Chem. Phys.*, 16(15):6931, 2014.

[86] M. Hanus, M. KabeláčŇ, J. Rejnek, F. RyjáčŇek, and P. Hobza. Correlated ab Initio Study of Nucleic Acid Bases and Their Tautomers in the Gas Phase, in a Microhydrated Environment, and in Aqueous Solution. Part 3. Adenine. *J. Phys. Chem. B*, 108(6):2087–2097, 2004.

[87] B. Cohen, P. M. Hare, and B. Kohler. Ultrafast Excited-State Dynamics of Adenine and Monomethylated Adenines in Solution: Implications for the Nonradiative Decay Mechanism. *J. Am. Chem. Soc.*, 125(44):13594–13601, 2003.

[88] A. Holmén and A. Broo. A Theoretical Investigation of the Solution N(7)H $\longleftrightarrow$ N(9)H Tautomerism of Adenine. *Int. J. Quantum Chem.*, 22:113, 1995.

[89] J. Gu and J. Leszczynski. A DFT Study of the Water-Assisted Intramolecular Proton Transfer in the Tautomers of Adenine. *J. Phys. Chem. A*, 103:2744, 1999.

[90] A. Laxer, D. T. Major, H. E. Gottlieb, and B. Fischer. ($^{15}N_5$)-Labeled Adenine Derivatives: Synthesis and Studies of Tautomerism by ^{15}N NMR Spectroscopy and Theoretical Calculations. *J. Org. Chem.*, 66:5463, 2001.

[91] M. Dreyfus, G. Dodin, O. Bensaude, and J. E. Dubois. Tautomerism of purines. I. N(7)H $\rightleftharpoons$ N(9)H equilibrium in adenine. *J. Am. Chem. Soc.*, 97(9):2369–2376, 1975.

[92] M. T. Chenon, R. J. Pugmire, D. M. Grant, R. P. Panzica, and L. B. Townsend. Carbon-13 magnetic resonance. XXVI. Quantitative determination of the tautomeric populations of certain purines. *J. Am. Chem. Soc.*, 97(16):4636–4642, 1975.

[93] N. C. Gonnella, H. Nakanishi, J. B. Holtwick, D. S. Horowitz, K. Kanamori, N. J. Leonard, and J. D. Roberts. Studies of tautomers and protonation of adenine and its derivatives by nitrogen-15 nuclear magnetic resonance spectroscopy. *J. Am. Chem. Soc.*, 105(7):2050–2055, 1983.

[94] A. Holmén. Vibrational Transition Moments of Aminopurines: Stretched Film IR Linear Dichroism Measurements and DFT Calculations. *J. Phys. Chem. A*, 101(24):4361–4374, 1997.

[95] T. Gustavsson, A. Sharonov, D. Onidas, and D. Markovitsi. Adenine, deoxyadenosine and deoxyadenosine 5′-monophosphate studied by femtosecond fluorescence upconversion

spectroscopy. *Chem. Phys. Lett.*, 356(1-2):49–54, 2002.

[96] T. Pancur, N. K. Schwalb, F. Renth, and F. Temps. Femtosecond fluorescence upconversion spectroscopy of adenine and adenosine: experimental evidence for the $\pi\sigma^*$ state? *Chem. Phys.*, 313(1-3):199–212, 2005.

[97] S. Ullrich, T. Schultz, M. Z. Zgierski, and A. Stolow. Direct Observation of Electronic Relaxation Dynamics in Adenine via Time-Resolved Photoelectron Spectroscopy. *J. Am. Chem. Soc.*, 126(8):2262–2263, 2004.

[98] H. Kang, B. Jung, and S. K. Kim. Mechanism for ultrafast internal conversion of adenine. *J. Chem. Phys.*, 118(15):6717, 2003.

[99] A. L. Sobolewski, W. Domcke, C. Dedonder-Lardeux, and C. Jouvet. Excited-state hydrogen detachment and hydrogen transfer driven by repulsive $^1\pi\sigma^*$ states: A new paradigm for nonradiative decay in aromatic biomolecules. *Phys. Chem. Chem. Phys.*, 4(7):1093–1100, 2002.

[100] L. Blancafort. Excited-State Potential Energy Surface for the Photophysics of Adenine. *J. Am. Chem. Soc.*, 128(1):210–219, 2006.

[101] C. M. Marian. A new pathway for the rapid decay of electronically excited adenine. *J. Chem. Phys.*, 122(10):104314, 2005.

[102] S. Perun, A. L. Sobolewski, and W. Domcke. Ab Initio Studies on the Radiationless Decay Mechanisms of the Lowest Excited Singlet States of 9H-Adenine. *J. Am. Chem. Soc.*, 127(17):6257–6265, 2005.

[103] L. Serrano-Andrés, M. Merchán, and A. C. Borin. Adenine and 2-aminopurine: Paradigms of modern theoretical photochemistry. *Proc. Natl. Acad. Sci.*, 103(23):8691–8696, 2006.

[104] L. Serrano-Andrés, M. Merchán, and A. C. Borin. A Three-State Model for the Photophysics of Adenine. *Chem.–Eur. J.*, 12(25):6559–6571, 2006.

[105] M. Barbatti, Z. Lan, R. Crespo-Otero, J. J. Szymczak, H. Lischka, and W. Thiel. Critical appraisal of excited state nonadiabatic dynamics simulations of 9H-adenine. *J. Chem. Phys.*, 137(22):22A503, 2012.

[106] M. Barbatti and H. Lischka. Nonadiabatic Deactivation of 9 H -Adenine: A Comprehensive Picture Based on Mixed Quantum−Classical Dynamics. *J. Am. Chem. Soc.*, 130(21):6831–6839, 2008.

[107] M. Zierhut, W. Roth, and I. Fischer. Dynamics of H-atom loss in adenine. *Phys. Chem. Chem. Phys.*, 6(22):5178–5183, 2004.

[108] M. G. D. Nix, A. L. Devine, B. Cronin, and M. N. R. Ashfold. Ultraviolet photolysis of adenine: Dissociation via the $^1\pi\sigma^*$ state. *J. Chem. Phys.*, 126(12):124312, 2007.

[109] H.-H Ritze, H. Lippert, E. Samoylova, V. R. Smith, I. V. Hertel, W. Radloff, and T. Schultz. Relevance of $\pi\sigma^*$ states in the photoinduced processes of adenine, adenine dimer, and adenine–water complexes. *J. Chem. Phys.*, 122(22):224320, 2005.

[110] W. M. I. Hassan, W. C. Chung, N. Shimakura, S. Koseki, H. Kono, and Y. Fujimura. Ultrafast radiationless transition pathways through conical intersections in photo-excited 9H-adenine. *Phys. Chem. Chem. Phys.*, 12(20):5317, 2010.

[111] B. Mennucci, A. Toniolo, and J. Tomasi. Theoretical Study of the Photophysics of Adenine in Solution: Tautomerism, Deactivation Mechanisms, and Comparison with the 2-Aminopurine Fluorescent Isomer. *J. Phys. Chem. A*, 105(19):4749–4757, 2001.

[112] S. Yamazaki and S. Kato. Solvent Effect on Conical Intersections in Excited-State 9H-Adenine: Radiationless Decay Mechanism in Polar Solvent. *J. Am. Chem. Soc.*, 129(10):2901–2909, 2007.

[113] V. Ludwig, Z. M. da Costa, M. S. do Amaral, A. C. Borin, S. Canuto, and L. Serrano-Andrés. Photophysics and photostability of adenine in aqueous solution: A theoretical study. *Chem. Phys. Lett.*, 492(1-3):164–169, 2010.

[114] R. Mitrić, U. Werner, M. Wohlgemuth, G. Seifert, and V. Bonačić-Koutecký. Nonadiabatic Dynamics within Time-Dependent Density Functional Tight Binding Method. *J. Phys. Chem. A*, 113(45):12700–12705, 2009.

[115] C. M. Marian, M. Kleinschmidt, and J. Tatchen. The photophysics of 7H-adenine: A quantum chemical investigation including spin–orbit effects. *Chem. Phys.*, 347(1-3):346–359, 2008.

[116] D. Tuna, A. L. Sobolewski, and W. Domcke. Mechanisms of Ultrafast Excited-State Deactivation in Adenosine. *J. Phys. Chem. A*, 118(1):122–127, 2014.

[117] E. Nir and M. S. de Vries. Fragmentation of laser-desorbed 9-substituted adenines. *Int. J. Mass Spectrom.*, 219(1):133–138, 2002.

[118] H. Kang, J. Chang, S. H. Lee, T. K. Ahn, N. J. Kim, and S. K. Kim. Excited-state lifetime of adenine near the first electronic band origin. *J. Chem. Phys.*, 133(15):154311, 2010.

[119] H. Asami, K. Yagi, M. Ohba, S. Urashima, and H. Saigusa. Stacked base-pair structures of adenine nucleosides stabilized by the formation of hydrogen-bonding network involving the two sugar groups. *Chem. Phys.*, 419:84–89, 2013.

[120] D. Voet, W. B. Gratzer, R. A. Cox, and P. Doty. Absorption Spectra of Nucleotides, Polynucleotides, and Nucleic Acids in the Far Ultraviolet. *Biopolymers*, 1:193–208, 1963.

[121] D. Onidas, D. Markovitsi, S. Marguet, A. Sharonov, and T. Gustavsson. Fluorescence Properties of DNA Nucleosides and Nucleotides: A Refined Steady-State and Femtosecond Investigation. *J. Phys. Chem. B*, 106(43):11367–11374, 2002.

[122] J.-M. L. Pecourt, J. Peon, and B. Kohler. Ultrafast Internal Conversion of Electronically Excited RNA and DNA Nucleosides in Water. *J. Am. Chem. Soc.*, 122(38):9348–9349, 2000.

[123] A. L. Sobolewski and W. Domcke. On the mechanism of nonradiative decay of DNA bases: ab initio and TDDFT results for the excited states of 9H-adenine. *Eur. Phys. J. D*, 20(3):369–374, 2002.

[124] I. Hünig, C. Plützer, K. A. Seefeld, D. Löwenich, M. Nispel, and K. Kleinermanns. Photostability of Isolated and Paired Nucleobases: N–H Dissociation of Adenine and Hydrogen Transfer in its Base Pairs Examined by Laser Spectroscopy. *ChemPhysChem*, 5(9):1427–1431, 2004.

[125] A. L. Sobolewski and W. Domcke. Photoinduced charge separation in indole–water clusters. *Chem. Phys. Lett.*, 329(1-2):130–137, 2000.

[126] A. L. Sobolewski and W. Domcke. Photoinduced Electron and Proton Transfer in Phenol and Its Clusters with Water and Ammonia. *J. Phys. Chem. A*, 105(40):9275–9283, 2001.

[127] R. Mitrić, J. Petersen, and V. Bonačić-Koutecký. Laser-field-induced surface-hopping method for the simulation and control of ultrafast photodynamics. *Phys. Rev. A*, 79(5):053416, 2009.

[128] M. Wohlgemuth, V. Bonačić-KouteckýĄ, and R. MitrićĄ. Time-dependent density functional theory excited state nonadiabatic dynamics combined with quantum mechanical/molecular mechanical approach: Photodynamics of indole in water. *J. Chem. Phys.*, 135(5):054105, 2011.

[129] R. Arce, L. Marínez, and E. Danielsen. The Photochemistry of Adenosine: Intermediates contributing to its Photodegradation Mechanism in Aqueous Solution at 298 K and Characterization of the Major Product. *Photochem. Photobiol.*, 58(3):318–328, 1993.

[130] M. Hanus, F. RyjáčŇek, M. KabeláčŇ, T. Kubař, T. V. Bogdan, S. A. Trygubenko, and P. Hobza. Correlated ab Initio Study of Nucleic Acid Bases and Their Tautomers in the Gas Phase, in a Microhydrated Environment and in Aqueous Solution. Guanine: Surprising Stabilization of Rare Tautomers in Aqueous Solution. *J. Am. Chem. Soc.*, 125(25):7678–7688, 2003.

[131] H. T. Miles, F. B. Howard, and J. Frazier. Tautomerism and Protonation of Guanosine. *Science*, 142(3598):1458–1463, 1963.

[132] C. M. Marian. The Guanine Tautomer Puzzle: Quantum Chemical Investigation of Ground and Excited States. *J. Phys. Chem. A*, 111(8):1545–1553, 2007.

[133] H. Chen and S. Li. Ab initio study on deactivation pathways of excited 9H-guanine. *J. Chem. Phys.*, 124(15):154315, 2006.

[134] L. Serrano-Andrés, M. Merchán, and A. C. Borin. A Three-State Model for the Photophysics of Guanine. *J. Am. Chem. Soc.*, 130(8):2473–2484, 2008.

[135] Z. Lan, E. Fabiano, and W. Thiel. Photoinduced Nonadiabatic Dynamics of 9 H -Guanine. *ChemPhysChem*, 10(8):1225–1229, 2009.

[136] S. Yamazaki, W. Domcke, and A. L. Sobolewski. Nonradiative Decay Mechanisms of the Biologically Relevant Tautomer of Guanine. *J. Phys. Chem. A*, 112(47):11965–11968, 2008.

[137] M. Barbatti, J. J. Szymczak, A. J. A. Aquino, D. Nachtigallová, and H. Lischka. The decay mechanism of photoexcited guanine − A nonadiabatic dynamics study. *J. Chem. Phys.*, 134(1):014304, 2011.

[138] B. Heggen, Z. Lan, and W. Thiel. Nonadiabatic decay dynamics of 9H-guanine in aqueous solution. *Phys. Chem. Chem. Phys.*, 14(22):8137, 2012.

[139] J.-M. L. Pecourt, J. Peon, and B. Kohler. DNA Excited-State Dynamics: Ultrafast Internal Conversion and Vibrational Cooling in a Series of Nucleosides. *J. Am. Chem. Soc.*, 123(42):10370–10378, 2001.

[140] J. Peon and A. H. Zewail. DNA/RNA nucleotides and nucleosides: direct measurement of excited-state lifetimes by femtosecond fluorescence up-conversion. *Chem. Phys. Lett.*, 348(3-4):255–262, 2001.

[141] V. Karunakaran, K. Kleinermanns, R. Improta, and S. A. Kovalenko. Photoinduced Dy-

namics of Guanosine Monophosphate in Water from Broad-Band Transient Absorption Spectroscopy and Quantum-Chemical Calculations. *J. Am. Chem. Soc.*, 131(16):5839–5850, 2009.

[142] B. Heggen, F. Buchner, A. Lübcke, and W. Thiel. 2015. in preparation.

[143] J. Rejnek, M. Hanus, M. KabeláčŇ, F. RyjáčŇek, and P. Hobza. Correlated ab initio study of nucleic acid bases and their tautomers in the gas phase, in a microhydrated environment and in aqueous solution. Part 4. Uracil and thymine. *Phys. Chem. Chem. Phys.*, 7(9):2006, 2005.

[144] R. Abouaf, J. Pommier, and H. Dunet. Electronic and vibrational excitation in gas phase thymine and 5-bromouracil by electron impact. *Chem. Phys. Lett.*, 381(3-4):486–494, 2003.

[145] H. Kang, K. T. Lee, B. Jung, Y. J. Ko, and S. K. Kim. Intrinsic Lifetimes of the Excited State of DNA and RNA Bases. *J. Am. Chem. Soc.*, 124(44):12958–12959, 2002.

[146] S. Ullrich, T. Schultz, M. Z. Zgierski, and A. Stolow. Electronic relaxation dynamics in DNA and RNA bases studied by time-resolved photoelectron spectroscopy. *Phys. Chem. Chem. Phys.*, 6(10):2796, 2004.

[147] B. K. McFarland, J. P. Farrell, S. Miyabe, F. Tarantelli, A. Aguilar, N. Berrah, C. Bostedt, J. D. Bozek, P. H. Bucksbaum, J. C. Castagna, R. N. Coffee, J. P. Cryan, L. Fang, R. Feifel, K. J. Gaffney, J. M. Glownia, T. J. Martinez, M. Mucke, B. Murphy, A. Natan, T. Osipov, V. S. Petrović, S. Schorb, Th. Schultz, L. S. Spector, M. Swiggers, I. Tenney, S. Wang, J. L. White, W. White, and M. Gühr. Ultrafast X-ray Auger probing of photoexcited molecular dynamics. *Nat. Commun.*, 5, 2014.

[148] M. Barbatti, A. J. A. Aquino, J. J. Szymczak, D. Nachtigallová, P. Hobza, and H. Lischka. Relaxation mechanisms of UV-photoexcited DNA and RNA nucleobases. *Proc. Natl. Acad. Sci.*, 107(50):21453–21458, 2010.

[149] M. Merchán, R. González-Luque, T. Climent, L. Serrano-Andrés, E. Rodríguez, M. Reguero, and D. Peláez. Unified Model for the Ultrafast Decay of Pyrimidine Nucleobases. *J. Phys. Chem. B*, 110(51):26471–26476, 2006.

[150] D. Asturiol, B. Lasorne, M. A. Robb, and L. Blancafort. Photophysics of the π,π* and n,π* States of Thymine: MS-CASPT2 Minimum-Energy Paths and CASSCF on-the-Fly Dynamics. *J. Phys. Chem. A*, 113(38):10211–10218, 2009.

[151] Z. Lan, E. Fabiano, and W. Thiel. Photoinduced Nonadiabatic Dynamics of Pyrimidine Nucleobases: On-the-Fly Surface-Hopping Study with Semiempirical Methods. *J. Phys. Chem. B*, 113(11):3548–3555, 2009.

[152] D. Picconi, V. Barone, A. Lami, F. Santoro, and R. Improta. The Interplay between ππ*/nπ* Excited States in Gas-Phase Thymine: A Quantum Dynamical Study. *ChemPhysChem*, 12(10):1957–1968, 2011.

[153] A. Nakayama, G. Arai, S. Yamazaki, and T. Taketsugu. Solvent effects on the ultrafast nonradiative deactivation mechanisms of thymine in aqueous solution: Excited-state QM/MM molecular dynamics simulations. *J. Chem. Phys.*, 139(21):214304, 2013.

[154] H. R. Hudock, B. G. Levine, A. L. Thompson, H. Satzger, D. Townsend, N. Gador, S. Ullrich, A. Stolow, and T. J. Martínez. Ab Initio Molecular Dynamics and Time-Resolved

Photoelectron Spectroscopy of Electronically Excited Uracil and Thymine. *J. Phys. Chem. A*, 111(34):8500–8508, 2007.

[155] J. J. Szymczak, M. Barbatti, J. T. S. Hoo, J. A. Adkins, T. L. Windus, D. NachtigallováĄ, and H. Lischka. Photodynamics Simulations of Thymine: Relaxation into the First Excited Singlet State. *J. Phys. Chem. A*, 113(45):12686–12693, 2009.

[156] P. M. Hare, C. E. Crespo-Hernández, and B. Kohler. Internal conversion to the electronic ground state occurs via two distinct pathways for pyrimidine bases in aqueous solution. *Proc. Natl. Acad. Sci.*, 104(2):435–440, 2007.

[157] T. Gustavsson, Á. Bányász, E. Lazzarotto, D. Markovitsi, G. Scalmani, M. J. Frisch, V. Barone, and R. Improta. Singlet Excited-State Behavior of Uracil and Thymine in Aqueous Solution: A Combined Experimental and Computational Study of 11 Uracil Derivatives. *J. Am. Chem. Soc.*, 128(2):607–619, 2006.

[158] T. Gustavsson, N. Sarkar, Á. Bányász, D. Markovitsi, and R. Improta. Solvent Effects on the Steady-state Absorption and Fluorescence Spectra of Uracil, Thymine and 5-Fluorouracil. *Photochem. Photobiol.*, 83(3):595–599, 2007.

[159] T. Gustavsson, Á. Bányász, N. Sarkar, D. Markovitsi, and R. Improta. Assessing solvent effects on the singlet excited state lifetime of uracil derivatives: A femtosecond fluorescence upconversion study in alcohols and D_2O. *Chem. Phys.*, 350(1-3):186–192, 2008.

[160] R. Improta, V. Barone, A. Lami, and F. Santoro. Quantum Dynamics of the Ultrafast $\pi\pi^*/n\pi^*$ Population Transfer in Uracil and 5-Fluoro-Uracil in Water and Acetonitrile. *J. Phys. Chem. B*, 113(43):14491–14503, 2009.

[161] T. Gustavsson, A. Sharonov, and D. Markovitsi. Thymine, thymidine and thymidine 5′-monophosphate studied by femtosecond fluorescence upconversion spectroscopy. *Chem. Phys. Lett.*, 351(3-4):195–200, 2002.

[162] Yannick Mercier, Fabrizio Santoro, Mar Reguero, and Roberto Improta. The Decay from the Dark $n\pi^*$ Excited State in Uracil: An Integrated CASPT2/CASSCF and PCM/TD-DFT Study in the Gas Phase and in Water. *J. Phys. Chem. B*, 112(35):10769–10772, 2008.

[163] F. Buchner, A. Nakayama, S. Yamazaki, H.-H. Ritze, and Lübcke A. The role of the $n\pi^*$ state for the excited state relaxation of hydrated thymine and thymidine. *J. Am. Chem. Soc.*, 2014. submitted.

[164] H.-J. Werner, P. J. Knowles, G. Knizia, F. R. Manby, M. Schütz, P. Celani, T. Korona, R. Lindh, A. Mitrushenkov, G. Rauhut, K. R. Shamasundar, T. B. Adler, R. D. Amos, A. Bernhardsson, A. Berning, D. L. Cooper, M. J. O. Deegan, A. J. Dobbyn, F. Eckert, E. Goll, C. Hampel, A. Hesselmann, G. Hetzer, T. Hrenar, G. Jansen, C. Köppl, Y. Liu, A. W. Lloyd, R. A. Mata, A. J. May, S. J. McNicholas, W. Meyer, M. E. Mura, A. Nicklass, D. P. O'Neill, P. Palmieri, K. Pflüger, R. Pitzer, M. Reiher, T. Shiozaki, H. Stoll, A. J. Stone, R. Tarroni, T. Thorsteinsson, M. Wang, and A. Wolf. MOLPRO, version 2010.1, a package of *ab initio* programs.

[165] S. Urano, X. Yang, and P. R. LeBreton. UV photoelectron and quantum mechanical characterization of DNA and RNA bases: valence electronic structures of adenine, 1,9-dimethyl-guanine, 1-methylcytosine, thymine and uracil. *J. Mol. Struct.*, 214:315–328,

1989.

[166] D. Ghosh, O. Isayev, L. V. Slipchenko, and A. I. Krylov. Effect of Solvation on the Vertical Ionization Energy of Thymine: From Microhydration to Bulk. *J. Phys. Chem. A*, 115(23):6028–6038, 2011.

[167] R. D. Brown, P. D. Godfrey, D. McNaughton, and A. P. Pierlot. Tautomers of cytosine by microwave spectroscopy. *J. Am. Chem. Soc.*, 111(6):2308–2310, 1989.

[168] J.-W. Ho, H.-C. Yen, W.-K. Chou, C.-N. Weng, L.-H. Cheng, H.-Q. Shi, S.-H. Lai, and P.-Y. Cheng. Disentangling Intrinsic Ultrafast Excited-State Dynamics of Cytosine Tautomers. *J. Phys. Chem. A*, 115(30):8406–8418, 2011.

[169] S. A. Trygubenko, T. V. Bogdan, M. Rueda, M. Orozco, F. J. Luque, J. Šponer, P. Slavíček, and P. Hobza. Correlated ab initio study of nucleic acid bases and their tautomers in the gas phase, in a microhydrated environment and in aqueous solution: Part 1. Cytosine. *Phys. Chem. Chem. Phys.*, 4(17):4192–4203, 2002.

[170] M. Barbatti, A. J. A. Aquino, J. J. Szymczak, D. Nachtigallová, and H. Lischka. Photodynamical simulations of cytosine: characterization of the ultrafast bi-exponential UV deactivation. *Phys. Chem. Chem. Phys.*, 13(13):6145, 2011.

[171] K. A. Kistler and S. Matsika. Radiationless Decay Mechanism of Cytosine: An Ab Initio Study with Comparisons to the Fluorescent Analogue 5-Methyl-2-pyrimidinone. *J. Phys. Chem. A*, 111(14):2650–2661, 2007.

[172] N. Ismail, L. Blancafort, M. Olivucci, B. Kohler, and M. A. Robb. Ultrafast Decay of Electronically Excited Singlet Cytosine via a π,π^* to n_o,π^* State Switch. *J. Am. Chem. Soc.*, 124(24):6818–6819, 2002.

[173] L. Blancafort, B. Cohen, P. M. Hare, B. Kohler, and M. A. Robb. Singlet Excited-State Dynamics of 5-Fluorocytosine and Cytosine: An Experimental and Computational Study. *J. Phys. Chem. A*, 109(20):4431–4436, 2005.

[174] L. Blancafort. Energetics of Cytosine Singlet Excited-State Decay Paths – A Difficult Case for CASSCF and CASPT2. *Photochem. Photobiol.*, 83(3):603–610, 2007.

[175] H. R. Hudock and T. J. Martínez. Excited-State Dynamics of Cytosine Reveal Multiple Intrinsic Subpicosecond Pathways. *ChemPhysChem*, 9(17):2486–2490, 2008.

[176] M. Merchán and L. Serrano-Andrés. Ultrafast Internal Conversion of Excited Cytosine via the Lowest $\pi\pi^*$ Electronic Singlet State. *J. Am. Chem. Soc.*, 125(27):8108–8109, 2003.

[177] K. Tomić, J. Tatchen, and C. M. Marian. Quantum Chemical Investigation of the Electronic Spectra of the Keto, Enol, and Keto−Imine Tautomers of Cytosine. *J. Phys. Chem. A*, 109(37):8410–8418, 2005.

[178] M. Z. Zgierski, S. Patchkovskii, T. Fujiwara, and E. C. Lim. On the Origin of the Ultrafast Internal Conversion of Electronically Excited Pyrimidine Bases. *J. Phys. Chem. A*, 109(42):9384–9387, 2005.

[179] A. L. Sobolewski and W. Domcke. Ab initio studies on the photophysics of the guanine–cytosine base pair. *Phys. Chem. Chem. Phys.*, 6(10):2763, 2004.

[180] A. Nakayama, Y. Harabuchi, S. Yamazaki, and T. Taketsugu. Photophysics of cytosine tautomers: new insights into the nonradiative decay mechanisms from MS-CASPT2 po-

tential energy calculations and excited-state molecular dynamics simulations. *Phys. Chem. Chem. Phys.*, 15(29):12322, 2013.

[181] S. Mai, P. Marquetand, M. Richter, J. González-Vázquez, and L. González. Singlet and Triplet Excited-State Dynamics Study of the Keto and Enol Tautomers of Cytosine. *ChemPhysChem*, 14(13):2920–2931, 2013.

[182] A. Sharonov, T. Gustavsson, V. Carré, E. Renault, and D. Markovitsi. Cytosine excited state dynamics studied by femtosecond fluorescence upconversion and transient absorption spectroscopy. *Chem. Phys. Lett.*, 380(1-2):173–180, 2003.

[183] L. Blancafort and A. Migani. Water effect on the excited-state decay paths of singlet excited cytosine. *J. Photochem. Photobiol., A*, 190(2-3):283–289, 2007.

[184] K. A. Kistler and S. Matsika. Photophysical pathways of cytosine in aqueous solution. *Phys. Chem. Chem. Phys.*, 12(19):5024, 2010.

[185] E. Fabiano and W. Thiel. Nonradiative Deexcitation Dynamics of 9H-Adenine: An OM2 Surface Hopping Study. *J. Phys. Chem. A*, 112(30):6859–6863, 2008.

[186] M. Barbatti and S. Ullrich. Ionization potentials of adenine along the internal conversion pathways. *Phys. Chem. Chem. Phys.*, 13(34):15492, 2011.

[187] H. Satzger, D. Townsend, and A. Stolow. Reassignment of the low lying cationic states in gas phase adenine and 9-methyl adenine. *Chem. Phys. Lett.*, 430(1-3):144–148, 2006.

[188] R. Improta and V. Barone. Excited States Behavior of Nucleobases in Solution: Insights from Computational Studies. In *Topics in Current Chemistry*, Topics in Current Chemistry, pages 1–29. Springer Berlin Heidelberg, 2014.

[189] E. Nir, L. Grace, B. Brauer, and M. S. de Vries. REMPI Spectroscopy of Jet-Cooled Guanine. *J. Am. Chem. Soc.*, 121(20):4896–4897, 1999.

[190] Y. He, C. Wu, and W. Kong. Photophysics of Methyl-Substituted Uracils and Thymines and Their Water Complexes in the Gas Phase. *J. Phys. Chem. A*, 108(6):943–949, 2004.

Abbreviations

AIP	adiabatic ionisation potential
AKE	average kinetic energy
AMP	adenosine monophosphate
BBO	barium borate
CI	conical intersection
CMP	cytosine monophosphate
CTTS	charge transfer to solvent
DNA	deoxyribonucleic acid
EUV	extreme ultraviolet spectral range: ∼10–120 nm
FC	Franck-Condon
FU	fluorescence up-conversion
FWHM	full width at half maximum
GMP	guanosine monophosphate
HCl	hydrochloric acid
HPLC	high pressure liquid chromatography
MBI	Max-Born-Institute
MCP	multi channel plate
NaCl	sodium chloride
NaI	sodium iodide
NO	nitric oxide
QM/MM	quantum mechanics/molecular mechanics

SFG	sum frequency generation
SHG	second harmonic generation
TA	transient absorption
TMP	thymidine monophosphate
TOF	time of flight
TRIS	tris(hydroxymethyl)aminomethane
TRPES	time-resolved photoelectron spectroscopy
UV	ultraviolet spectral range: 200–380 nm
VIE	vertical ionisation energy
VUV	vacuum ultraviolet spectral range: ∼100–200 nm

Acknowledgements / Danksagung

The completion of this thesis would not have been possible without many people. I want to thank all these people:

First of all, I thank my supervisor and first referee Marc Vrakking for giving me the opportunity to write this thesis in department A of the Max-Born-Institute in Berlin. I also acknowledge fruitful discussions as this thesis was evolving.

I also thank Philippe Wernet, the second referee of this thesis, for his interest in this work and his willingness to review it.

I gratefully acknowledge Andrea Lübcke's enduring guidance throughout my work. We spent instructive weeks in the lab where she patiently explained what and why until I was prepared to work on my own. She supported me whenever I got stuck but still gave me enough freedom to work on my own. And finally, she thoroughly read (and extensively commented on) this whole manuscript.

I thank Thomas Schultz whose interesting lecture on modern methods in spectroscopy motivated me to join this research field. He brought me in contact with the Max-Born-Institute and introduced me to my later project leader Andrea Lübcke.

Special thanks goes to Hans-Hermann Ritze who shared his profound knowledge and experience on molecular dynamics of isolated molecules and therefore contributed a lot to this work.

I thank the collaborators Roland Mitrić, Akira Nakayama and Walter Thiel for fruitful discussions and sophisticated theoretical simulations that I was allowed to present in this thesis.

Für die Unterstützung von technischer Seite danke ich dem gesamten Service- und Techniker-Team des Max-Born-Institut. Besonderer Dank gilt hier vor allem F. Noack und G. Mügge für die Bereitstellung des Lasersystems „Multicolor I“ im Femtosekunden-Applikationslabor. Außerdem danke ich K. Bäurich für die umfangreiche Betreuung im Chemie-Labor und R. Peslin für die engagierte Unterstützung bei mechanischen Problemen jeder Art.

Letztlich gilt ein ganz besonderer Dank meiner Familie und meinen Freunden, die mich während der letzten vier Jahre unterstützt und alle meine Launen in den verschiedenen Phasen der Arbeit ertragen haben.

List of own publications

- F. Buchner, A. Nakayama, S. Yamazaki, H.-H. Ritze, A. Lübcke (2014). **The role of the nπ* state for the excited-state relaxation of hydrated thymine and thymidine.** *J. Am. Chem. Soc.*, submitted.
- P. Trabs, F. Buchner, M. Ghotbi, A. Lübcke, H.-H. Ritze, M. J. J. Vrakking, A. Rouzée (2014). **Time-, angle- and kinetic-energy-resolved photoelectron spectroscopy of highly excited states of NO.** *J. Phys. B.*, *47*, 124016 .
- F. Buchner, H. H. Ritze, J. Lahl, A. Lübcke (2013). **Time-resolved photoelectron spectroscopy of adenine and adenosine in aqueous solution.** *Phys. Chem. Chem. Phys.*, *15*, 11402.
- T. Leitner, F. Buchner, A. Lübcke, A. Rouzée, L. Rading, P. Johnsson, M. Odelius, H. O. Karlsson, M. Vrakking, P. Wernet (2013). **Coherent wave packet dynamics in photo-excited NaI.** In *EPJ Web of Conferences* (Vol. 41, p. 02027). EDP Sciences.
- N. Preissler, F. Buchner, T. Schultz, A. Lübcke (2013). **Electrokinetic Charging and Evidence for Charge Evaporation in Liquid Microjets of Aqueous Salt Solution.** *J. Phys. Chem. B*, *117*(8), 2422.
- F. Buchner, H. H. Ritze, M. Beutler, T. Schultz, I. V. Hertel, A. Lübcke (2012). **Role of alkali cations for the excited state dynamics of liquid water near the surface.** *J. Chem. Phys.*, *137*, 024503.
- F. Buchner, T. Schultz, A. Lübcke (2012). **Solvated electrons at the water–air interface: surface versus bulk signal in low kinetic energy photoelectron spectroscopy.** *Phys. Chem. Chem. Phys.*, *14*(16), 5837.
- F. Buchner, A. Lübcke, N. Heine, T. Schultz (2010). **Time-resolved photoelectron spectroscopy of liquids.** *Rev. Sci. Instrum.*, *81*(11), 113107.
- A. Lübcke, F. Buchner, N. Heine, I. V. Hertel, T. Schultz (2010). **Time-resolved photoelectron spectroscopy of solvated electrons in aqueous NaI solution.** *Phys. Chem. Chem. Phys.*, *12*(43), 14629.

Eidesstattliche Versicherung

Hiermit versichere ich, dass ich die vorliegende Dissertation selbstständig und nur unter Verwendung der angegebenen Literatur und Hilfsmittel verfasst habe. Die Arbeit ist weder in einem früheren Promotionsverfahren angenommen noch als ungenügend beurteilt worden.

Berlin, den 06. Januar 2015